Title:

Tau modulates nuclear integrity, chromatin, and cholesterol synthesis genes via the nuclear envelope

Authors:

Lisa Diez[1*], Renata Ponce-Lina[1*], Cagla Kilic[1,3], Rithika Sankar[1], Frieda Balduin[1], Cong Wang[4], Pia Grundschoettel[5,6], Koki Sakurai[7,8], Bilge Askin[1,2,3], Chiara Bordier[1], Tejaswini Karra[1], Katharina Tipp[1], Boglarka Krisztina Nagy-Herczeg[1], Maryam Mohamaddokht[1], Leandre Ravatt[1,2,3], Satabdee Mohapatra[1,3], Alvaro Dominguez-Baquero[1,3], Ramesh Adakkattil[9], Maximilian Franck[1], Sabrina Hübschmann[1], Elena De Domenico[10], Marc Beyer[10], Tomohisa Toda[7,8,11], Helena Radbruch[12], Tara L. Spires-Jones[13,14], Alexander von Appen[9], Thomas Ulas[5,6], Andrew Newman[15], Fan Liu[4], Susanne Wegmann[1,2,3,15,#]

[1] German Center for Neurodegenerative Diseases (DZNE), Berlin, Germany
[2] Einstein Center for Neuroscience (ECN), 10117 Berlin, Germany
[3] Charité University Medicine, 10117 Berlin, Germany
[4] Department of Structural Biology, Leibniz-Forschungsinstitut für Molekulare Pharmakologie (FMP), 13125 Berlin, Germany
[5] Genomics and Immunoregulation, Life & Medical Sciences (LIMES) Institute, University of Bonn, Bonn, Germany
[6] Systems Medicine, German Center for Neurodegenerative Diseases (DZNE), Bonn, Germany
[7] Laboratory of Neural Epigenomics, Institute of Medical Physics and Micro-tissue Engineering, Friedrich-Alexander-Universität Erlangen-Nürnberg, 91054 Erlangen, Germany
[8] Max-Planck-Zentrum für Physik und Medizin, 91054 Erlangen, Germany
[9] Max Planck Institute of Molecular Cell Biology and Genetics, 01307 Dresden, Germany
[10] Platform for Single Cell Genomics and Epigenomics (PRECISE), DZNE Bonn, 53127 Bonn, Germany
[11] German Center for Neurodegenerative Diseases (DZNE), 01307 Dresden, Germany
[12] Department of Neuropathology, Charité Universitätsmedizin Berlin, 10117 Berlin, Germany
[13] UK Dementia Research Institute, the University of Edinburgh, Edinburgh EH8 9JZ, UK
[14] Centre for Discovery Brain Sciences, the University of Edinburgh, Edinburgh EH8 9JZ, UK
[15] Institute of Cell and Neurobiology, Charité Universitätsmedizin Berlin, 10117 Berlin, Germany

corresponding author: susanne.wegmann@dzne.de
* contributed equally

Keywords:

Tau missorting, nucleus, nuclear envelope, proximity biotinylation, Lamin B receptor, SUN1, chromatin, gene expression, Alzheimer's disease

Abstract/Summary

The intracellular re-distribution of the neuronal microtubule-associated protein Tau, from the axon into the somatodendritic compartment, is a physiological stress-related event and occurs early in Alzheimer's disease (AD). Nuclear envelope distortions have been linked to the presence and aggregation of pathological Tau near the nucleus in these diseases. How physiologically increased soma Tau levels, enabling Tau interactions with the nucleus, impact nuclear integrity and neuronal physiology is unclear. Combining proximity biotinylation interactomics with chromatin imaging and molecular assays, we show that soluble Tau interacts with proteins coordinating chromatin at the inner nuclear membrane, including lamin B receptor and SUN1. This interaction promotes nuclear envelope invaginations and damage and changes the coordination of DNA at the nuclear lamina. Increasing somatodendritic Tau is sufficient to upregulate the expression of multiple transcription factors implicated in AD pathogenesis and to reduce expression of genes involved in cholesterol biosynthesis, which seem coordinated at lamin associated domains. These nuclear envelope-related mechanisms suggest that physiological, neuronal stress-related somatodendritic Tau missorting can initiate chromatin-related cascades important for early changes in AD and tauopathies.

Introduction

Tau, encoded by the *MAPT* gene, is an intrinsically disordered protein that has a high affinity to microtubules (MTs) (Mandelkow *et al*, 1995; Jeganathan *et al*, 2008). The majority of Tau is expressed in neurons of the central nervous system. In mature neurons, Tau is enriched in the axon where its microtubule association is regulated by phosphorylation and other post-translational modifications (PTMs) (Parra Bravo *et al*, 2024). In conditions where Tau gets "activated", the subcellular distribution of phosphorylated Tau – detached from MTs – changes, and similar levels of soluble cytosolic Tau can be found throughout axon, soma, and dendrites. This subcellular phospho-Tau redistribution (= missorting) can be triggered by various physiological neuronal stress conditions, including temperature changes, mechanical stimulation, and neuronal hyperactivity (Sultan *et al*, 2011; Schneeweis *et al*, 2024; Braun *et al*, 2020), and is considered an early pathological change in Tau-related brain disorders like frontotemporal dementia (FTD) and Alzheimer's disease (AD).

Pathological accumulation of phosphorylated Tau in neuronal cell bodies can be observed in a number (>20) of neurological conditions, e.g., in traumatic brain injury, epilepsy, autoimmune brain diseases, and – most prominently – AD and primary tauopathies (Spillantini & Goedert, 2013; Chang *et al*, 2021). It is widely believed that the accumulation of soluble phospho-Tau precedes Tau aggregation in neuronal cell bodies, which is a pathological hallmark and correlate of neuronal loss in these diseases. The actual, neurophysiological reason and function of somatodendritic Tau "missorting" remains unclear. It is likely that the interaction of Tau with molecules and organelles in the somatodendritic compartment, like the nucleus, builds the foundation for stress-related Tau functions. Notably, these interactions of Tau would be enabled in both physiological stress and disease conditions.

In human AD and FTD brains, as well as in cell models of tauopathy, Tau was shown to cluster at the outer nuclear envelope (NE) and to impair nuclear transport through nuclear pores (Jiang & Wolozin, 2021; Kang *et al*, 2021; Eftekharzadeh *et al*, 2018; Diez *et al*, 2022). This could affect chromatin organization and gene expression. Accordingly, changes in chromatin and gene expression occur in AD and FTD brains and in brains of tauopathy animal models (Rico *et al*, 2018; Frost *et al*, 2014; Klein *et al*, 2019). Global chromatin relaxation (Frost *et al*, 2014), neurotoxic re-activation of retroviral transposable elements (Ramirez *et al*, 2022; Guo *et al*, 2018), and activation of senescence-like expression profiles (Musi *et al*, 2018) have been reported to correlate with Tau pathology.

In the physiological context, Tau inside the nucleus was shown to interact with DNA, histone proteins, and the nucleolus (Maina *et al*, 2018; Sultan *et al*, 2011; Liu & Götz, 2013; Benhelli-Mokrani *et al*, 2018), with suggested functions in gene expression, DNA protection and compaction, and nucleolar stress response. However, there is currently no consensus about the impact of Tau on chromatin, and reported effects range from Tau-induced global chromatin relaxation and transcriptional activation (Klein *et al*, 2019; Frost *et al*, 2014) to stabilization of chromatin compaction and transcriptional repression (Benhelli-Mokrani *et al*, 2018; Rico *et al*, 2018). These inconclusive reports may – at least in part – result from difficulties to distinguish between physiological nuclear actions of soluble somatodendritic Tau *versus* pathological actions or loss of nuclear functions of oligomeric and aggregated Tau.

In this study, we aimed at understanding whether Tau missorting – i.e., the increase of Tau in the somatodendritic compartment – is sufficient to induce nuclear distortions and changes in neuronal chromatin and gene expression, and which Tau interactions underlie these effects. The herein newly identified interactions of Tau with nuclear envelope proteins, like the lamin B receptor (LBR) and SUN1, provide a molecular mechanism for neuronal chromatin and gene expression alterations in response to physiological and disease-associated soluble Tau missorting.

Results

Pathological Tau is associated the neuronal nuclear envelope distortions in the brain

In human Alzheimer's disease (AD) brains, diffuse misfolded (Alz50+) and aggregated Tau accumulate in the soma of neurons (Figure 1A). In neurons having soluble phosphorylated Tau (pS202/pS205/pT231), presumably prior to developing Tau aggregation pathology, p-Tau can be found at the nuclear envelope (NE; labeled with anti-SUN1 antibody; Figure 1B). Neurons with larger p-Tau aggregates in the cell body did not show this Tau pattern (Figure 1B), indicating that cytosolic phosphorylated Tau may have a special affinity to the NE. This is in line with previous observations of our own and others, for example, that Tau clusters forming during the aggregation process associated with the NE (Kang *et al*, 2021; Hochmair *et al*, 2022; Eftekharzadeh *et al*, 2018) and that Tau interactions with nuclear pore proteins (Nups) affect neuronal nuclear transport (Eftekharzadeh *et al*, 2018).

In addition, AD (Braak 5/6) compared to control (Braak 0/1) brains had more nuclei with NE deformations – folds and invaginations –, whereby the occurrence of invagination was higher in neurons with misfolded Tau in the soma (Figure 1C,D; Supplemental Video V1-4). In both AD and control brains, the number of nuclei surrounded by aggregated Tau correlated with the number of neuronal nuclei having invaginations (Figure 1E). These data suggest that the accumulation of non-aggregated phosphorylated Tau in the neuronal soma may be associated with nuclear envelope distortions (Figure 1F). The details of Tau interactions with the NE, and their consequences, remain unclear though.

Increased somatodendritic soluble Tau is sufficient to induce nuclear shape changes

Tau protein levels - in healthy neurons high in axons and low in soma and dendrites - increase in the soma in physiological and pathological neuronal stress conditions. To investigate whether the somatodendritic missorting of soluble Tau is sufficient, or whether pathological misfolding would be necessary, to induce NE alterations, we modulated soma Tau levels in cultured hippocampal neurons using adeno-associated virus (AAV) constructs. A reduction in Tau levels were achieved by inhibiting endogenous Tau transcription (Tau KD) through expression of a *MAPT*-targeted zinc-finger protein array coupled to a gene-silencing KREB transcription factor, ZFP90 (Wegmann *et al*, 2021), which reduced Tau levels by >50% compared to untreated neurons (Tau base; Figure 2A, Figure EV1A). The Tau knockdown AAV construct expressed equal amounts of ZFP90 and GFP as a transduction marker, separated by a self-cleaving 2a peptide. A control AAV expressing target-less zinc finger array (ZFP72) did not change Tau levels compared to GFP expressing or non-treated neurons (Figure EV1B). To produce elevated somatodendritic Tau levels, we expressed GFP-labeled full-length wildtype Tau (2N4R isoform; Tau OE) or FTD-mutants Tau^{P301L} (TauPL OE) and $Tau^{P301L/S320F}$ (TauPL/SF OE; Figure 2A). GFP-Tau^{P301L} does not aggregate in neurons, yet has a higher oligomerization propensity than wildtype Tau due to increased accessibility of an aggregation-prone motif (PHF6*; amino acids ^{306}*VQIVYK*^{311}) in the beginning of R3 in the Tau repeat domain (Von Bergen *et al*, 2000). GFP-$Tau^{P301L/S320F}$, having an additional pro-aggregation mutation in R3, spontaneously forms NFT-like aggregates in the soma of a subset (5-20%) of neurons (Jorge-Oliva *et al*, 2023; Hochmair *et al*, 2025). Here we used these FTD-Tau variants to test the effect of Tau oligomerization and aggregation on the NE. After 7 days of AAV expression, Tau KD neurons had <50% of total endogenous Tau left (by Western blot; Figure 2B). Tau OE and TauPL OE neurons had a 5-7-fold increase in total soluble Tau. TauPL/SF OE neurons showed only a 2-fold increase in soluble Tau (RIPA buffer extracts), which may be linked to the sequestering of soluble Tau into detergent-insoluble NFTs.

It was previously suggested that endogenous Tau can be found inside the nucleus, particularly in conditions of stress-induced somatodendritic missorting (Violet *et al*, 2014; Benhelli-Mokrani *et al*, 2018). To test how AAV-modulated Tau levels correlated with nuclear Tau levels, we determined total Tau immunofluorescence (endogenous + GFP-Tau) in the soma and nucleus of AAV-treated neuronal cultures (Figure 2C). We found that both somatic and nuclear Tau levels were reduced to ~30% in Tau KD neurons (Figure 2C). In Tau OE and TauPL OE neurons, somatic and nuclear Tau levels were ~1.5-fold increased compared to untreated

159 controls (Tau base). Notably, in hippocampal neurons of AD brains, we measured an up to
160 ~2.5-fold increased levels of diffuse, non-aggregated Tau in the soma (Figure EV1C).
161 Interestingly, TauPL/SF OE neurons had ~2-fold increased Tau in the soma but nuclear Tau
162 levels were comparable to untreated neurons. Together, these data suggest that the levels of
163 somatic and nuclear Tau are correlated in the case of soluble Tau variants, while pro-
164 aggregant TauPL/SF cannot enter the nucleus and resides in the cytoplasm.

165 Finally, to test the effect of Tau levels on nuclear shape, we measured the circularity of
166 neuronal nuclei after immunostaining for Lamin A/C. Expression of all Tau variants led to a
167 decrease in nuclear circularity compared to control neurons, indicating an effect of elevated
168 Tau levels on NE integrity (Figure 2D), whereby overexpression of wildtype Tau had a stronger
169 effect than FTD-mutant TauPL and TauPL/SF expression. Neurons with TauPL/SF aggregates
170 in the soma showed little effects on nuclear circularity (non-significant), as did Tau KD neurons.
171 These data support the idea that elevated levels of soluble, non-aggregated Tau in the soma
172 – and nucleus - are sufficient to induce nuclear shape changes and envelope distortions in
173 neurons.

174 ***Increased levels of Tau in the nucleoplasm induce nuclear envelope damage***

175 Next, we tested whether increased soluble Tau levels were sufficient to induce NE rupture,
176 and whether this was related to the presence of Tau outside (in cytoplasm) or inside (in
177 nucleoplasm) the nucleus. NE rupture can be detected by local accumulation of BAF (barrier-
178 to-autointegration factor) at NE damage sites, and the subsequent recruitment of Emerin to
179 these sites during repair (Halfmann *et al*, 2019) (Figure 2E). We expressed SNAP-BAF
180 together with different GFP-labeled Tau and Tau-NLS (nuclear localization signal) variants in
181 human cells for 24 h (Figure 2F) and determined the amount of SNAP-BAF accumulation at
182 the NE, as well as its colocalization with Emerin (by immunostaining). In all cells expressing
183 GFP (control), Tau, or Tau-NLS, Emerin was recruited from the NE into BAF accumulations
184 (Figure 2G), indicating the successful initiation of NE repair processes. Quantification of BAF
185 accumulation at the NE showed that all Tau variants carrying a recombinant NLS had
186 significantly more NE ruptures than GFP-expressing control cells (Figure 2H). Tau variants
187 without NLS, primarily expressed in the cytoplasm, showed only a small, non-significant
188 increase in NE BAF accumulation, i.e., NE ruptures. These data indicate that soluble Tau
189 inside the nucleus promotes NE damage but does not impact initial steps (Emerin recruitment)
190 of the repair process.

191 ***Proximity biotinylation suggests Tau interactions with inner nuclear envelope***

192 To understand how soluble Tau can induce NE distortion and damage, we decided to identify
193 nuclear interaction partners of Tau by proximity biotinylation. We fused full-length human
194 wildtype (TurboID-Tau) or FTD-mutant Tau^{P301L} (TurboID-Tau^{P301L}; Figure 3A,B) to the biotin
195 ligase TurboID (Branon *et al*, 2018), which facilitated rapid (within minutes upon addition of
196 biotin) biotinylation of proteins in proximity (~35 nm distance) to Tau or Tau^{P301L} in their native
197 cellular environment. We transiently expressed TurboID-Tau and TurboID-Tau^{P301L} in human
198 neuroblastoma cells (SH-SY5Y line), lysed the cells in hypotonic buffer, and concentrated their
199 nuclei by centrifugation in order to enrich nuclear Tau interaction partners. Biotinylated nuclear
200 proteins that have been in proximity to Tau or Tau^{P301L} were pulled-down from the nuclear
201 pellet using magnetic streptavidin-coated beads and analyzed by mass spectrometry (Figure
202 3B,C,D; Figure EV2A,B). Expression of TurboID alone was used to obtain a control
203 interactome for unspecific TurboID activity. Notably, while the TurboID-Tau fusion constructs
204 (MW ~85 kDa) were mostly located in the cytoplasm, the TurboID only control (MW ~39 kDa)
205 was abundant in the nucleus (Figure 3C), rendering it a stringent control for identified potential
206 nuclear Tau interactors. In addition, as positive control and reference interactome for protein-
207 specific nuclear interactions, we also determined the nuclear proximity biotinylation proteome
208 for TurboID fused to the C-terminal fragment of TDP-43 (TurboID-TDP-43ctf; Figure EV2C-F),
209 a component of insoluble cytoplasmic TDP-43 aggregates in ALS/FTD brains (Igaz *et al*, 2008).
210 A proximity biotinylation interactome of TDP-43ctf has previously been determined in mouse
211 neuroblastoma cells (Chou *et al*, 2018).

Proteome analysis of biotinylated proteins from five independent cultures revealed multiple significantly enriched proteins in the TurboID-Tau (87 proteins) and TurboID-Tau^{P301L} (44 proteins) proximity proteome compared to TurboID alone (log2[fold change Tau/Ctrl] >1.5, p-value <10^{-1}) (Figure 3E; Supplemental Tables T1, T2). As expected for bait proteins in our approach, Tau (MAPT) itself was maximally enriched in the Tau and Tau^{P301L} biotinylation proteomes (Figure 3E). Among the significantly enriched proteins, we found 27 proteins that were enriched in the biotinylation proteomes of both Tau variants (~30% of potential TurboID-Tau interactors (27/87), ~60% of TurboID-Tau^{P301L} interactors (27/44); Figure 3F). Interestingly, the TurboID-Tau proteome showed more overlap with the proteome of TurboID-TDP-43ctf ((37/87) = 43% potential Tau interactors), a protein that shuttles between nucleo- and cytoplasm (Figure EV2G; Supplemental Table T3).

Gene ontology (GO) analysis for biotinylated proteins enriched in TurboID-Tau and TurboID-Tau^{P301L} over TurboID control proteomes clustered potential Tau interactors into the cellular components *nuclear inner membrane*, *ER membrane*, and *nuclear outer membrane* (Figure 3G). Tau^{P301L} had overall fewer potential interactors, which clustered in the cellular components *nuclear outer membrane* and *organelle envelope*. Cluster analysis of significantly enriched proteins (log2[fold change] > 1.5 and -log10[p-value] > 1) using STRING (Szklarczyk *et al*, 2023) grouped potential Tau interactors in the inner nuclear and in the synaptic vesicle membrane, and suggested their involvement in ER organization, TORC1 complex, and cholesterol and phospholipid biosynthesis (Figure 3H). Cholesterol synthesis and lipid metabolism were also the strongest enriched categories in GO Biological processes for Tau interactors. hits for potential Tau interactors (FigureEV2H, Supplemental Table T4). For TauPL, potential interactors, clustered, for example, as component of the plasma membrane, were involved in microtubule transport and lipid synthesis, i.e., phosphate acyltransferases, or were calcium channel subunits (Figure 3I). Potential interactors of our positive control, TDP-43ctf, clustered in categories associated with the *nuclear outer membrane* and *nuclear envelope* (Figure EV2H), confirming previous results (Chou *et al*, 2018). In summary, GO and cluster analyses suggested that many of the nuclear Tau interactors are involved in NE and ER associated processes, i.e., chromatin organization at the inner nuclear membrane and metabolic regulation including cholesterol and lipid synthesis. Notably, since the NE is an extension of the endoplasmic reticulum (ER), interactions of Tau with components of NE and ER could be functionally and/or structurally related, and could both contribute to nuclear shape changes and NE damage induced by soluble Tau.

Tau interactions with the NE may explain how elevated soluble Tau levels could directly induce NE dysfunction and distortion. We find that both Tau and Tau^{P301L} may interact with NE proteins involved in chromatin organization at the inner nuclear lamina as well as with several proteins involved in nuclear transport (Nups and nuclear transport receptors, NTRs; Figure 3J). Thereby, especially NE proteins seem to be more enriched among potential Tau than TauPL interactors. Identified NE-specific proteins could be grouped into four protein categories (Figure 3K): (i) INM embedded proteins (LBR (= lamin B receptor), SUN1, and LEM-domain proteins, LEM-2 and EMD (= Emerin)) that coordinate chromatin association and repression at the inner leaflet of the NE (Zuleger *et al*, 2011), as well as lamin associated inner nuclear membrane protein TMEM43, important for NE structure and anchoring Emerin in the envelope (Bengtsson & Otto, 2008). (ii) Structural nuclear pore complex (NPC) proteins (Nup210, NDC1) in the nuclear envelope-embedded ring of the NPC (Schmidt & Görlich, 2016). (iii) Components of the LINC (linker of nucleoskeleton and cytoskeleton) complex (SYNE2 (=Nesprin-2), SUN1) required to translate cytoskeletal mechanical forces into changes in chromatin structure and gene expression (Sosa *et al*, 2013; Rothballer & Kutay, 2013); (iv) Nuclear transport receptors (e.g., TNPO2 and XPO6) that regulate the nuclear import and export, respectively, of biomolecular cargo through NPCs (Terry *et al*, 2007). Notably, we did not identify potential interactions of Tau with FG-rich Nups, i.e., Nup98 or Nup62, which we had previously reported to interact with Tau (Eftekharzadeh *et al*, 2018; Diez *et al*, 2022). One may account this to the rather short (10 min) biotinylation reaction time and the potential inaccessibility of Nups in the dense FG-Nup phase of the pore (Wente & Rout, 2010). Interestingly, chromatin associated proteins of the inner NE leaflet (LBR, SUN1, LEM-2, and EMD) were not identified as significant

interactors of Tau^{P301L}, indicating that oligomerization-prone FTD-mutant Tau may engage less in intranuclear interactions. This supports our observations that Tau$^{P301L/S320F}$ barely enters the nucleus at high cytosolic levels (Figure 2C) and that soluble wildtype Tau – entering the nucleus - is most effective in inducing NE distortion (Figure 2D). LBR, however, was previously found in small cytoplasmic FTD-Tau aggregates (Jiang *et al*, 2021).

Tau interacts with LBR and SUN1 at the inner nuclear envelope

The detection of multiple chromatin binding envelope proteins as potential interactors of Tau was a surprising finding. To verify these interactions, we performed co-immunoprecipitation (co-IP) of endogenous Tau (client) with different NE proteins (bait proteins) - LBR, Nesprin-2, and Lamin A/C - from nuclear enriched fractions of SH-SY5Y cells (Figure 4A, Figure EV3A). Intensity measurement indicated a mild interaction of Tau with LBR but not LaminA/C or Nesprin-2. Reciprocally, from cells overexpressing GFP-Tau, we were able to pull-down SUN1 and LBR (clients) together with GFP-Tau (bait) from nuclear lysates (Figure 4B, Figure EV3B,C,D). These data confirmed a physical interaction of Tau with LBR and SUN1. Notably, SUN1 is part of LINC complexes that are responsible for mechanical force transduction from the cytoskeleton onto chromatin (Carley *et al*, 2021). Tau effects on LINC have been recently suggested in FTD-Tau expressing cells (Sohn *et al*, 2023).

To test whether endogenous Tau would be close to other identified potential Tau interactors in the intact cellular environment, and whether these potential interactions would actually occur in or at the nucleus, we performed microscopy-based proximity ligation assays (PLAs). In these assays, two proteins – Tau and a respective partner protein – are labeled with specific primary antibodies in otherwise untreated, fixed cells or tissue, and their close proximity (<40 nm) is detected upon local fluorescent signal generation and amplification (= foci at interaction locations; Figure 4C). To outline the nuclei, DNA was labeled in parallel using DAPI. First, specificity and background signal of PLAs were detected in human neuronal cells (SH-SY5Y line) using a human Tau specific antibody (Tau13, mouse, Tau N-terminal end) alone or in combination with non-binding IgG (rabbit) as negative controls (no PLA signal detected), or Tau13 together with an antibody targeting another region of Tau (Tau DAKO, rabbit, Tau C-terminus) as positive control (strong cytoplasmic PLA signal, few PLA spots in the nucleus) (Figure 4D). A combination of antibodies against SUN1 (epitope in NE intraluminal space) and LaminA/C, interacting at the inner nuclear membrane (INM), was used as positive control to produce NE PLA signal. Additionally, for each individual antibody used in PLAs, the cellular binding pattern was first verified by immunofluorescence. To test the proximity of endogenous Tau with potential nuclear interactors, we quantified the PLA signal produced at the NE for NE proteins (Figure 4E,F) and inside the nucleus for intranuclear proteins (Figure 4G) in comparison to the IgG negative control. Among NE candidate interactors, we found the LINC complex proteins SYNE2 (Nesprin-2) and SUN1 and the INM embedded chromatin binders, EMD and LBR to produce significant PLA signal with Tau (Figure 4E,F).

In addition, we also probed the proximity of Tau with the histone associated proteins HP1α and HP1γ, which mediate the binding of inner NE proteins to chromatin and have been shown to interact with Tau *in vitro* (Abasi *et al*, 2024), as well as of the heterochromatin marks H3K9me3 and H4K20me3 because Tau has been reported to stabilize chromatin compaction (Rico *et al*, 2018). For the HP1 proteins, strong PLA signal occurred throughout the nucleus (Figure 4G). For heterochromatin histone marks, weaker but still significant signal was detected (Figure EV3E). This indicated that Tau interacted with additional chromatin-associated proteins.

Next, we tested whether the proximity of endogenous Tau with NE chromatin binders, HP1 proteins, and heterochromatin marks would occur in neurons. PLAs in primary hippocampal mouse neurons (DIV12) showed significantly enriched signal for LEM-2, LBR, HP1γ, and HP1α, but not for any of the histone marks tested (Figure 4H; Figure EV3F). Furthermore, to test whether the proximity to inner NE proteins, i.e., LBR and its binding partner HP1γ, was specific to Tau or would also occur for related proteins, we performed PLAs of LBR and HP1γ with MAP2, another neuronal microtubule-associated protein with a domain organization and

structure similar Tau and of constitutive high abundance in the somatodendritic compartment. MAP2 did not produce PLA signal with LBR and Hp1γ (Figure 4H). This indicated that the potential intranuclear interaction with chromatin binding proteins were specific to Tau. Notably, we could not test the proximity of Tau to SUN1 or SYNE2 (Nesprin-2) in primary neurons by PLA because of a lack of antibodies enabling specific immunodetection of the murine protein variants.

Tau in proximity to inner NE chromatin binders in the human brain

To test whether our observation of Tau in proximity to chromatin organizing protein in the inner NE would also occur in the human brain, we performed PLAs in FFPE-fixed human brain sections. We chose to perform the assays in AD brains, i.e., hippocampal CA1 area and dentate gyrus, because of the abundant Tau missorting and pathology in these brain regions. First, we verified the specificity of antibody binding in human brain sections for SUN1, LBR, HP1γ, and LEM-2 by immunofluorescence (Figure 4I, Figure EV4A,B). SUN1 in hippocampal neurons showed the expected NE localization as well as a single condensed circular accumulation in the center of the nucleus. Similarly, LBR localized to the nuclear envelope and formed a single condensed spot inside nuclei (Figure 4I). Additionally, LBR co-localized with cytoplasmic Tau aggregates, supporting previous observation of LBR in optogenetically induced small FTD-mutant Tau clusters (Essepian *et al*, 2025; Jiang & Wolozin, 2021). HP1γ had a peculiar distribution with strong signal in a single condensed accumulation inside the nuclei and additional weak signal at the NE and at strings connecting the NE with the inner nuclear accumulation; reminiscent of a “cart-wheel” shape. This DNA shape was found more frequently in hippocampal neurons of AD than of control brains (Figure EV4C).

Next, we performed PLAs in combination with anti-Tau antibodies (Tau13 or Tau DAKO) (Figure 4J, Figure EV4D). In parallel to PLAs and DNA labeling by DAPI, we immunolabeled neuronal MAP2 and Tau in the same brain sections, which enabled us to identify neuronal nuclei and distinguish between neurons with different levels of Tau in their cell bodies (i.e., no Tau, diffuse Tau, aggregated Tau in NFTs). For the NE proteins SUN1, LBR and LEM-2, PLA signal occurred at the NE in CA1 and DG neurons, as well as at a single condensed area in the center of a subset of CA1 neuronal nuclei, which may resemble PLA signal produced by inner nuclear condensed accumulations of the NE proteins that we observed by immunostaining (Figure 4I, Figure EV4D). For HP1γ, PLA signal was found in all areas of DAPI signal, including the NE, the inner nuclear accumulation, and DNA “strings” bridging between the NE and the accumulation (also compare HP1γ immunostaining in Figure 4I). Negative controls for PLA in human brain, i.e., anti-SUN1 antibody alone or NE-residing SUN1 in combination with postsynaptic PSD-95 that are located far from one another, did not produce PLA signal (Figure 4K). Notably, PLA signal for Tau with chromatin associated proteins occurred in neurons with and without Tau accumulation in the soma (according to immunofluorescence), suggesting that even low soluble somatodendritic - and nuclear - Tau levels are sufficient to put Tau in proximity of these proteins. This matches our observations for PLA of soluble endogenous Tau in wildtype neurons. In summary, these data suggest that Tau in the human brain associates with inner NE chromatin organizers and their HP1 adaptor proteins, even at low nuclear Tau levels. Close proximity – indicating indirect or direct interactions - of soluble Tau with chromatin binding proteins like SUN1, LBR and LEM-2 could be relevant for Tau-induced NE distortions or be part of a physiological Tau function in chromatin regulation, or both.

Tau interactions with LBR and SUN1 induce NE invaginations and nuclear inclusions

Having confirmed the interaction of Tau with LBR and SUN1, we aimed to investigate whether they would contribute to Tau-related nuclear envelope invaginations. Removal or knockdown of LBR and SUN1 likely destabilize the NE, thereby prohibiting to test whether these proteins would be necessary for Tau-related NE distortions. We therefore generated expression constructs that enabled us to artificially enhance the interaction of Tau with LBR and SUN1 using the cell permeable synthetic rapamycin analogue rCD1 (Vester *et al*, 2022) and determine the effects on the NE by microscopy: Co-expression of Tau fused to FKBP (mRFP-

373 FKBP-Tau) with LBR or SUN1 fused to SNAP (LBR-eCFP-SNAP, SUN1-eCFP-SNAP) in cells
374 allowed to determine effects on the NE upon Tau overexpression and upon additional
375 molecular coupling of Tau to LBR or SUN1. We found that overexpression of Tau was sufficient
376 to induce the frequent occurrence of nuclear envelope invaginations and circular nuclear, Tau-
377 filled "inclusions" (Figure 5A). Enhancing the interactions of Tau with LBR and SUN1 – through
378 coupling of FKBP-Tau to LBR-SNAP or SUN1-SNAP using rCD1 compound - further enhanced
379 the occurrence of NE invaginations and inclusions (Figure 5A,B). Thereby, the number of
380 inclusions was favored over the number of invaginations in the presence of rCD1. Detailed
381 microscopic evaluation of the inclusions suggested that the circular Tau inclusions originated
382 from NE protrusions (= invaginations) into the nucleoplasm, representing cytoplasm inclusions
383 enveloped by parts of the NE containing LBR and SUN1. This idea was confirmed by the
384 presence of soluble Tau and tubulin inside circular inclusions, and the presence of NE proteins
385 - LBR, SUN1, LaminB1, LaminA/C and nuclear pore complexes - in inclusion "envelopes"
386 (Figure 5C). Further, the nuclear inclusions did not co-localize with other prominent nuclear
387 organelles, i.e., nucleoli (NPM1+) and nuclear speckles (SRRM2+). Similar results were
388 obtained for co-expression of TauP301L with LBR and SUN1 (Figure EV5A,B).

389 Importantly, intensity line plots through individual Tau inclusions showed that DNA (DAPI
390 signal) and the DNA-binding protein HP1γ were enriched around Tau inclusions, immediately
391 adjacent to the LBR/SUN1 containing NE envelopes, likely through coupling of DNA to LBR,
392 SUN1, and other chromatin binding proteins in the inner NE (Figure 5C,D,E). This DNA
393 condensation at the surface of abnormal, Tau-induced nuclear inclusions and NE invaginations
394 could have a large impact on chromatin regulation and, hence, gene expression.

395 ***Tau condenses with LBR in on DNA***

396 We were especially intrigued by the identification of LBR as nuclear Tau interactor. Tau/LBR
397 interactions at the inner NE could change LBR's DNA binding, thereby impacting chromatin
398 arrangement and gene expression. LBR links chromatin to the nuclear envelope through its N-
399 terminal, nucleoplasmic projection domain (LBR-npd), directly through its DNA interaction
400 domain (Tudor domain, aa 1-89) or via binding of HP1 proteins to its globular II domain (aa 90-
401 211) (Olins *et al*, 2010) (Figure 6A). PONDR plots along the amino acid sequence of LBR
402 revealed that its N-terminal region (LBR-npd), which is protruding from the INM into the nuclear
403 lumen and encodes the DNA binding activity, was especially disordered (Figure 6A). Hp1γ,
404 which was reported to mediate LBR binding to DNA (Polioudaki *et al*, 2001) and form
405 condensates in the presence of DNA (Li *et al*, 2023), showed a disordered region in the middle
406 of its sequence. In addition, when looking at structural characteristics of LBR-npd, HP1γ, and
407 other potential nuclear Tau interactors, we found that also LEM-2, and Emerin had predicted
408 high levels of protein disorder (PONDR score > 0.5) and/or had, like Tau (MAPT), the tendency
409 to form condensates/granules (CatGRANULE score > 0.75 (Bolognesi *et al*, 2016); PhasePro
410 (http://predict.phasep.pro/ (Chen *et al*, 2022)) (Figure EV6A,B). Based on these
411 characteristics, we hypothesized that LBR-npd could form condensates with DNA and that the
412 presence of Tau may alter the interaction of LBR-npd with DNA.

413 Using recombinant Tau, LBR-npd, and HP1γ proteins (Figure 6B), we first tested whether LBR-
414 npd would show phase separation behavior – alone and in combination with DNA – by
415 microscopy. Because it is unclear which DNA base pair sequences LBR is binding to, we used
416 λ-phage DNA (λ-DNA, 47 kbp) covering a wide spectrum of base pair sequences. Without
417 DNA, LBR-npd by itself readily formed small spherical condensates (diameter 1-2 μm) that
418 assembled into larger, grape-like clusters (Figure 6C, left). Tau and HP1γ, or both together,
419 efficiently partitioned into and co-enriched in LBR-npd condensates but did not form
420 condensates in the absence of LBR-npd (Figure 6D). Fluorescence recovery after
421 photobleaching (FRAP) of condensed LBR-npd showed that Tau and HP1γ cooperatively
422 reduced the LBR-npd molecular mobility inside condensates (Figure 6E), indicating that Tau
423 and HP1γ may independently interact with LBR-npd, possibly at separate binding sites.

424 Next, we added DNA to our experimental setup. The addition of λ-DNA to LBR-npd, under the
425 same buffer conditions, changed the assembly of LBR-npd: the grape-like LBR-npd

condensate assemblies disappeared and LBR-npd attached to the added DNA strands (Figure 6C, right; Figure EV6C), resulting in thick DNA bundles coated by LBR-npd. In less coated DNA regions, LBR-npd condensates were attached to and bridging between thinly LBR-npd coated DNA threads. This arrangement of LBR-ndp on DNA was reminiscent of the wetting of protein condensates on cytoskeletal fibers (King & Petry, 2020). In the presence of HP1γ, Tau, or both, LBR-npd still associated with DNA, and HP1γ and Tau colocalized with the larger condensed LBR-npd clusters. FRAP of LBR-npd associated with DNA revealed a mobile molecular fraction of only ~3% (Figure 6E, Figure EV6D) in all conditions, indicating a tight association of LBR-npd with DNA, regardless of the presence of HP1γ or Tau.

To further assess how the presence of Tau could influence the direct interaction between LBR and DNA, we examined the binding of LBR-npd to DNA by electrophoretic mobility shift assays (EMSAs; Figure 6F). Mixing DNA (500 bp fragment; 20 ng = 1 ng/μl) with LBR-npd (400 ng = 20 ng/μl) in the presence of increasing Tau concentrations (0, 25, 50, 75 ng = 0, 1.25, 2.5, 3.75 ng/μl) showed that already small amounts of Tau (25 ng) substantially increased the binding of LBR-ndp to DNA (upshift of signal for DNA/protein complexes). This suggested a strong activity of Tau in enhancing HP1γ-independent binding of LBR-npd to DNA, notably, below LBR-npd concentrations needed for microscopic condensation. Interestingly, Tau alone also bound DNA already at low concentrations, starting at 50 ng/μl (Figure 6F), which supports previous observations of Tau binding to DNA (Sultan *et al*, 2011; Benhelli-Mokrani *et al*, 2018; Hua *et al*, 2003; Sjöberg *et al*, 2006).

Together, these data suggest that low levels of intranuclear Tau can enhance HP1-independent binding of LBR-npd to chromatin, whereas higher nuclear Tau levels may alter LBR's homotypic interactions and HP1-binding by changing its condensation behavior.

Elevated Tau levels modulate neuronal chromatin

Previous reports suggested that Tau could modulate neuronal chromatin in transgenic flies and AD brains (Frost *et al*, 2014; Klein *et al*, 2019). Our data indicated that Tau-induced NE invaginations and nuclear inclusions induce abnormal, local DNA condensation (Figure 5) and that Tau can influence the binding of LBR to HP1 and DNA (Figure 6). To better understand the connection between increased somatodendritic and nuclear Tau levels and neuronal chromatin organization, we investigated histone modifications associated with gene repression, H3K9me3 (marking constitutive heterochromatin (Padeken *et al*, 2022)), and gene activation, H3K9ac (marking enhancers or promotors (Gates *et al*, 2017)) by immunofluorescence (Figure 7A,B). Compared to GFP-expressing control neurons (Tau base), the number per nucleus but not size of H3K9me3-positive chromocenters (ChrCs) increased in Tau OE and TauPL OE neurons (Figure 7C; Figure EV7A,B). Notably, not all H3K9me3-positive chromocenters also contained highly condensed DNA (= high DAPI intensity). Tau KD did not change H3K9me3-positive ChrCs. Western blots of neuronal lysates confirmed these results (Figure EV7C,D). For H3K9ac, Tau OE (ns), TauPL OE, and Tau KD all increased general nuclear fluorescence intensity outside of ChrCs compared to control (Tau base) neurons. Western blots showed the same trend but remained none-significant.

These data indicated that increased cytosolic and nuclear Tau levels elevate H3K9me3-associated chromatin repression, while simultaneously increasing gene activation related to H3K9Ac. Tau reduction led to gene activation. Together this suggests that somatodendritic Tau mis-sorting, and the simultaneous increase in the amount of nuclear Tau, may favor chromatin repression, and that high Tau levels induce additionally gene activation.

Tau changes chromatin association with the nuclear envelope

In addition to histone modifications, the spatial organization and condensation of interphase chromatin serves as a higher-order regulatory level of gene expression. Thereby, DNA-dense ChrCs and the nuclear envelope play important roles. Both ChrCs and chromatin associated with the nuclear lamina (lamina-associated domains, LADs) contain mostly repressed genes (van Steensel & Belmont, 2017). We tested whether modulating Tau levels would change DNA distribution and condensation in neuronal nuclei. Nuclei of untreated or GFP-expressing

478 neurons (Tau base) and Tau KD neurons had homogenously distributed DNA outside of
479 chromocenters (diffuse DAPI signal) (Figure 7E). Nuclei of neurons with elevated Tau (Tau OE
480 and TauPL OE) seemed to have a higher concentration of DNA at the NE, whereas their
481 nucleoplasm seemed largely void of diffuse DNA signal, with few, small DNA-dense "spots".
482 Intensity line plots across nuclei and analysis of average radial DNA distribution (clock scan)
483 confirmed this observation.

484 Next, we tested whether the redistribution of DNA in Tau OE and TauPL OE neurons was
485 associated with changes in DNA compaction, which is thought to somewhat correlate to gene
486 repression. Fluorescence lifetime imaging (FLIM) of siR-DNA (siR-Hoechst) labeled DNA in
487 living neurons. siR-DNA is a far-red, cell permeable live cell DNA probe that can be used to
488 estimate DNA compaction based on its fluorescent lifetime being quenched with increasing
489 DNA density (Hockings *et al*, 2020). Using this approach, we found that neurons with all Tau
490 levels had similar siR-DNA lifetimes at the NE (Figure 7F), indicating that the redistribution of
491 DNA towards the NE in Tau OE and TauPL OE neurons was not associated with stronger DNA
492 compaction at the NE. Surprisingly, however, Tau OE and TauPL OE neurons showed strongly
493 increased Sir-DNA lifetimes – indicative of DNA decondensation - in the core of DNA ChrCs.
494 The Sir-DNA lifetimes of the remaining parts of the nucleoplasm (open chromatin) were again
495 similar in all conditions.

496 Finally, we tested whether Tau may induce changes in the nuclear positioning of specific
497 chromosomes. In the interphase nucleus, chromosomes occupy distinct territories in the 3D-
498 volume of the nucleus (Cremer & Cremer, 2001). The spatial arrangement of chromosome
499 territories (CTs) can influence the expression of harbored genes. Certain chromosomes
500 (Chr's), e.g., Chr1, Chr13, ChrX, and Chr18 have been shown to preferentially locate at the
501 nuclear periphery in interphase nuclei of mammalian cells (Mehta *et al*, 2010). Interestingly,
502 LBR was shown to contribute to ChrX silencing by associating it to the NE (Chen *et al*, 2016).
503 Furthermore, ChrX was shown to re-localize from the NE into the nuclear interior in epileptic
504 neurons of human brains (Borden & Manuelidis, 1988), a condition that is also linked to
505 somatodendritic Tau re-sorting upon neuronal hyperactivity.

506 We performed fluorescent in-situ hybridization (FISH) of chromosomes (Chromosome PAINT)
507 to test whether modulation of Tau levels would change the radial positioning of these
508 chromosomes in neuronal nuclei (Figure 7G,H). Analyzing the equatorial plane of nuclei
509 labeled for individual chromosomes, we found that the LBR-associated ChrX was shifted
510 towards the nuclear periphery upon Tau reduction (Tau KD) compared to untreated neurons
511 (Tau base). Chr1 was shifted towards the periphery in both Tau OE as well as TauKD neurons.
512 Chr13 shifted from the nuclear center to the periphery in Tau KD neurons and kept its radial
513 positioning but dispersed (= broader radial distribution) in Tau OE neurons. Different from the
514 other chromosomes tested, Chr18 was located in DAPI-positive ChrCs; it appeared to
515 condense half-way between the nuclear center and the periphery upon Tau KD. Together,
516 these data indicate that Tau levels can have a profound influence on CT organization in
517 neuronal nuclei, whereby the removal of Tau seems to have the strongest effect. This suggests
518 that low levels of endogenous nuclear Tau - present in naïve neurons – are sufficient to
519 influence chromosome organization, however, with so far unknown effects on the expression
520 of genes encoded by the affected chromosomes.

521 In summary, our data suggest that both elevation and reduction of Tau modulate neuronal
522 chromatin on multiple levels, including histone modification, DNA distribution, and CT
523 positioning.

524 ***Elevated Tau upregulates transcription factors regulating stress response pathways***

525 The identified Tau-related changes in chromatin regulation (Figure 7) and LBR-DNA
526 interactions (Figure 6) suggested that somatodendritic Tau missorting would influence gene
527 expression. To examine which genes are responsive to changes in somatodendritic/nuclear
528 Tau, we sequenced the RNA isolated from neurons containing different Tau levels (Tau base,
529 Tau OE, and Tau KD; Figure 8A). To minimize contribution of glial RNA, the primary cultures
530 where treated with AraC to kill dividing cells (Figure EV8A).

Increasing Tau (Tau OE) led to an upregulation (n = 87) and down regulation (n = 55) of several genes (significance cut-off: fold change > 2, adjusted p-value < 0.05; Figure 8B,C,D; Figure EV8B,C,D and S9A; Supplemental Table T5,T6). Reduction of Tau (Tau KD) had comparably small effects on gene expression (significantly up-regulated genes: n = 2; down-regulated genes: n = 1 (*MAPT*)), consistent with the idea that increased concentrations of Tau in and around the nucleus, as a consequence of Tau overexpression or somatodendritic resorting in neuronal stress conditions, could function as signal to initiate gene expression changes.

Gene set enrichment analysis (GSEA; considering all transcriptomic changes; Figure 8E; Figures EV9A,B) showed that increased Tau levels (Tau OE vs. Tau base) upregulated pathways of TNFα (proinflammatory) signaling, apoptosis, and oxidative stress (hypoxia) response. These pathways are associated with AD (Tao *et al*, 2024; Kumari *et al*, 2023; Decourt *et al*, 2017). In Tau OE neurons, upregulation of these pathways involved upregulation of a number of transcription factors (TFs), including activators and repressors (Figure 8F,G; Figure EV10A,B).

wPGSA gene-set analysis of all DEGs (except transposable elements, TEs), which predicts the activities of transcription regulators responsible for the observed gene expression changes (Kawakami *et al*, 2016) (wPSGA t-score indicates expression changes in genes regulated by a certain TF; TFs with a wPSGA t-score > +4 or < -4 and adjusted p-value < 10^{-5} are predicted to be involved in gene deregulation; a negative t-score indicates an overall decreased expression of the TF-regulated genes). wPGSA suggested that gene upregulation upon Tau overexpression (t-score > +4), including upregulation of TF expression, was controlled by three TFs, i.e., *Jun*, *Gcr*, and *Bmi1* (Figure EV10C). The immediate early gene *Jun* is a component of the AP-1 complex that, for example, suppresses metalloproteases in response to neuronal depolarization (Rylski *et al*, 2009). In AD, *Jun* was suggested to drive aberrant TE mobilization and to be associated with the innate immune response. In our data set, *Jun* is among the transcriptomically upregulated TFs (Figure EV10B). The glucocorticoid receptor, *Gcr*, has anti-inflammatory and immunosuppressive functions and is regulated by, as well as controls, AP-1 expression in a negative feed-back loop to regulate stress response (Karin & Chang, 2001). *Bmi1* is a major component of the polycomb group complex 1 that functions as an essential epigenetic repressor of multiple regulatory genes, e.g., involved in DNA damage repair, p53 repression and neuronal antioxidative processes (Chatoo *et al*, 2009). Notably, *Gcr* and *Bmi1* themselves were not among the significant DEGs in our data set.

For the downregulation of genes upon Tau overexpression (t-score < -4), wPSGA predicted numerous TFs to be involved, indicating that higher Tau concentrations might increase activity and/or amount of gene repressing factors. This was in line with the observed upregulation of repressive TFs (Figure EV10B). For example: (i) The c-AMP responsive element modulator *Crem*, which regulates metabolic pathways and reactions and is a negative regulator of synaptogenesis in response to neuronal activity (Aguado *et al*, 2009). (ii) The transcriptional repressor *Rest*, which becomes activated in differentiated neurons confronted with ischemic and seizure conditions to protect against neuronal death (Hwang & Zukin, 2018; Cheng *et al*, 2022), for example, by repressing the expression of pre- and post-synaptic proteins necessary for neurotransmission (McClelland *et al*, 2014). In AD, *Rest* and its protective role are downregulated (Lu *et al*, 2014; Aron *et al*, 2023), and *Rest* dysregulation is also implicated in the pathogenesis of epilepsy, Huntington's disease, Parkinson's disease (McClelland *et al*, 2011; Zuccato *et al*, 2003; Chuang *et al*, 2009). (iii) *Tgif1*, a TGFβ/Smad-induced repressor and regulator of the Wnt pathway that is involved regulating DNA repair and homeostasis (Canchi *et al*, 2019). In AD, *Tgif1* is downregulated and Wnt signaling suppressed (Martínez & Inestrosa, 2021). Other upregulated TFs that have previously been linked to AD and Tau pathology included the ER-stress and unfolded-protein response responsive transcription factors *Atf3* and *DDIT3/Chop*, the hypoxia-responsive factor *Hif1*α, associated with APP processing, Aβ production and Tau pathology (Alexander *et al*, 2022), the antioxidant transcription factor *NFE2L2/Nrf2*, *Rorb* that has been identified to be expressed in neuronal subtypes particularly vulnerable to Tau pathology (Leng *et al*, 2021), and *Arid5b* involved in

584 metabolic reprogramming and upregulated in Aβ-transgenic mice (Guo *et al*, 2024; Cichocki *et*
585 *al*, 2018). In addition, we detected *Foxo6*, a transcriptional activator involved in insulin signaling
586 and regulating apoptosis, inflammation, and oxidative stress responses (Li *et al*, 2025; Hyun
587 Kim *et al*, 2011), as well as *Neurod6*, important for neurodevelopment and differentiation and
588 downregulated in AD brains (Satoh *et al*, 2014), to be downregulated.

589 Upregulated non-TF genes included the lectin-cleaving metalloprotease *Adamts1*, a GWAS
590 risk gene for AD and suggested to improve repair and synaptic plasticity after seizure-induced
591 neuronal damage (Gottschall & Howell, 2015; Balusu *et al*, 2023), and gastrin-releasing
592 peptide, *Grp*, that stimulates excitatory neurons, likely by binding to *Grp* receptors on inhibitory
593 neurons and reducing their inhibitory activity (Yang *et al*, 2017). Furthermore, we found some
594 long non-coding RNAs (lncRNAs) to be deregulated in Tau OE neurons (Figure EV9A,C),
595 including upregulation of *Neat1*, an essential component of paraspeckles. *Neat1* is also
596 upregulated in AD brains (An *et al*, 2018) and has been implicated in decreasing apoptosis in
597 response to metabolic stress (Chai *et al*, 2022), cGAS-STING-IRF3 signaling (Morchikh *et al*,
598 2017), and regulation of potassium channel activity (Barry *et al*, 2017).

599 Together, these data reveal that increased soluble Tau in the somatodendritic and nuclear
600 compartments is sufficient to upregulate the expression of numerous TFs that stir inflammatory
601 and cell stress-related pathways observable in neurological conditions presenting with
602 somatodendritic Tau re-sorting, i.e., epilepsy and chronic stress (Tai *et al*, 2016; Lopes *et al*,
603 2016), as well as in AD and other neurodegenerative diseases (Orr *et al*, 2017). Some of the
604 Tau-induced TF changes identified, e.g., *Rest* and *Tgif1*, are opposite from what has been
605 observed in late-stage AD brains, indicating that they represent pro-pathological adjustments
606 in the transcriptome occurring in response to early Tau changes.

607 ***Elevated Tau reduces cholesterol synthesis genes***

608 Pathways downregulated by increased Tau levels (Tau OE vs. Tau base) appeared to be
609 TORC1 signaling, a regulator of cell metabolism and autophagy (Chantranupong *et al*, 2015;
610 Hu *et al*, 2019) and of neuronal dendritic growth and plasticity (Li *et al*, 2009; Kovács *et al*,
611 2007), and cholesterol biosynthesis (Figure 8E; Figure EV9B; Supplemental Table T7). GO
612 analysis of significant DEGs supported the reduced expression of genes involved in
613 cholesterol, lipid, and Acyl-CoA synthesis (Figure 8F, bottom).

614 Among the downregulated genes were *Acly* (ATP citrate Lyase), *Hmgsc1* (3-hydroxy-3-
615 methylglutaryl-CoA (HMG-CoA) synthase) and *Hmgcr* (HMG-CoA reductase), which catalyze
616 the essential first steps in the mevalonate pathway of cholesterol biosynthesis. Other enzymes
617 in the mevalonate pathway, i.e., *Mvk* and *Mvd*, as well as *Nsdhl* and *Ftfd1*, essential for later
618 steps during the cholesterol synthesis, were also downregulated. Notably, the upregulated
619 transcriptional repressor *Tgif1* is also involved in cholesterol biosynthesis regulation by
620 negatively regulating *ACAT2* involved in cholesterol esterification (Pramfalk *et al*, 2014) and
621 apolipoproteins (Melhuish *et al*, 2010). By real-time qPCR, we could verify a significant
622 increase in *Tgif1* transcripts in Tau OE neurons (Figure 8H), similar to what has previously
623 been observed in AD brains (Canchi *et al*, 2019). mRNA levels of *Hmgcs1* and *Nsdhl*,
624 representatively chosen as genes directly involved in cholesterol synthesis, appeared by RT-
625 qPCR to be non-significantly downregulated in Tau OE cultures. However,
626 immunofluorescence showed reduced levels of *Hmgcr* protein in hippocampal neurons of AD
627 compared to control brains (Figure 8I), which is in line with previous reports (Varma *et al*,
628 2021), but *Hmgcr* reduction did not correlate with the accumulation of soluble or aggregated
629 phospho-Tau in neuronal somata.

630

631 ***LAD and Chromosome association of genes deregulated by Tau***

632 Since we found that Tau interacts with LBR and SUN (and potentially other chromatin
633 organizing proteins at the NE), we wondered whether a signature of LAD associated genes
634 could be found in the transcriptome data of neurons with elevated Tau levels. LADs of type1
635 are consistently associated with the nuclear lamina, contain constitutively repressed genes,

636 and contribute to genome stability and cell identity, whereas LADs of type2 are flexible genome
637 regions that are facultative repressive and facilitate dynamic, context-specific gene regulation
638 (van Steensel & Belmont, 2017). LBR has been shown to bind LADs (Van Schaik *et al*, 2025)
639 and to coordinate ChrX on the nuclear lamina (Chen *et al*, 2016). Determining the LAD
640 association of significant DEGs in Tau OE neurons (assignment based on data for midbrain
641 human neurons (Shah *et al*, 2023)), we found that > 50% of DEGs (79 of 142) were associated
642 with LADs (LAD type1: 22 DEGs = 15% of all DEGs; LAD type2: 57 DEGs = 40% of all DEGs)
643 in Tau OE compared to Tau base neurons, confirming a pronounced effect of Tau on genes
644 associated with the NE (Figure 8J; Supplemental Table T9). LAD type1 assigned DEGs in Tau
645 OE neurons did not cluster in certain GO pathways but coded, for example, for proteins
646 involved in neuronal activity and metabolism. LAD type2 assigned DEGs clustered in
647 cholesterol synthesis pathways (4 DEGs) and coded for a number of TFs deregulated by Tau.
648 This indicated that elevated Tau levels influence the expression of genes located in genomic
649 regions that are context-dependent coordinated at the NE.

650 To further support these findings, we performed CUT&Tag (Cleavage Under Targets &
651 Tagmentation) for the chromatin activation mark H3K9ac, which identifies genomic positions
652 that are activated. CUT&Tag confirmed a strong activation of intronic and non-coding distal
653 intergenic regions in Tau OE compared to Tau base neurons (Figure EV11). Further, many
654 genome regions activated in Tau OE neurons associated with LADs type2 as well as TEs (i.e.,
655 LINEs, SINEs, and LTRs). TEs have previously been linked to Tau pathology(Ramirez *et al*,
656 2022; Guo *et al*, 2018) and spreading (Liu *et al*, 2023).

657 We next analyzed whether Tau-responsive genes would be chromosome specific. DEGs in
658 Tau OE neurons were distributed throughout chromosomes Chr1-19 and ChrX, with most of
659 them located on Chr1 (16 genes; 1.0% of Chr1 genes), Chr2 (13 genes, 0.6 % of Chr2 genes),
660 Chr10 (13 genes; 0.8% of Chr10 genes), Chr11 (12 genes; 0.5% of Chr11 genes), Chr13 (10
661 genes; 1.0% of Chr13 genes), and Chr17 (12 genes; 1.1% of Chr17 genes) (Figure 8K).
662 Interestingly, Chr1, which contained the most DEGs in Tau OE neurons and was modulated
663 by Tau levels in chromosome PAINT data (Figure 7G,H), was indeed reported to be associated
664 with the NE and the nucleolus (Manuelidis & Borden, 1988), the two nuclear entities LAD
665 regions attach to.

666 Further, we found that LAD type2 DEGs - including the cholesterol biosynthesis genes *Hmgcs1*
667 *Hmgcr,* and *Nsdhl* -, were enriched in Chr13 and ChrX (Figure 8L,M; Figure EV12). Previous
668 reports showed that Chr13 and ChrX are located near the NE (Tanabe *et al*, 2002; Borden &
669 Manuelidis, 1988; Zuleger *et al*, 2011), and our chromosome PAINT data (Figure 7G,H)
670 indicate that these chromosomes may be responsive to changes in Tau levels as well.

671 Together, our data indicate that high somatodendritic Tau levels can alter the expression of
672 genes located near the NE, mainly associated with facultative LADs type2, which represent
673 genomic elements responsive to conditional cellular adaptation. This includes genes involved
674 in cholesterol biosynthesis. These findings may suggest that increased somatodendritic
675 soluble Tau levels – as a result of physiological stress or disease-induced Tau re-distribution
676 – could downregulate neuronal cholesterol metabolism and upregulate neuronal stress
677 response pathways on the genomic level by interfering with the NE association of chromatin.

678

679 **Discussion**

680 The neuronal subcellular redistribution and somatodendritic "invasion" of Tau occurs in
681 response to diverse physiological and pathological neuronal stimuli, including temperature
682 changes, mechanical stimulation, and high neuronal activity. This suggests that resorting (=
683 missorting) of Tau – and its access to somatodendritic cellular organelles/compartments like
684 the nucleus – is part of the physiological neuronal stress-response. Upon prolonged and
685 excessive missorting of Tau, these interactions may exert pathological effects observed in Tau-
686 related neurodegenerative diseases, e.g., irreversible as synaptic decline, senescence, and,
687 ultimately, neuronal death. Deciphering the physiological function of Tau missorting is

688 therefore key to understand the reason for this frequent event, which is also is one of the initial
689 steps in the etiology of multiple neurodegenerative diseases and conditions. Here we show
690 that increasing soluble wildtype Tau levels in the neuronal somatodendritic compartment – to
691 levels comparable to human AD brain neurons – is sufficient to induce nuclear envelope
692 distortions, alterations in chromatin structure, and gene expression changes relevant for
693 neuronal stress response and cholesterol biosynthesis. Furthermore, our data suggest that
694 interactions of soluble Tau with chromatin organizing proteins in the inner nuclear envelope,
695 i.e., LBR and SUN1, underlie these effects, indicating a crucial role of nuclear Tau in neuronal
696 stress response.

697 ***The nuclear envelope – a central role for Tau-related chromatin effects? -*** In recent years,
698 multiple studies reported the correlation between Tau pathology in AD and FTD brains and in
699 cellular and animal models with FTD-mutant Tau expression (Cornelison *et al*, 2019; Prissette
700 *et al*, 2022; Sun *et al*, 2022; Fernández-Nogales & Lucas, 2020; Jiang & Wolozin, 2021;
701 Monroy-Ramírez *et al*, 2013; Essepian *et al*, 2025), with abnormal neuronal nuclear shapes
702 and NE invaginations and distortions, resembling phenotypic aspects of laminopathies (Frost,
703 2016; Frost et al, 2016a). It was, for example, proposed that NE deformations in primary
704 tauopathies can be induced by aberrant Tau-related microtubule polymerization through the
705 NE (Paonessa *et al*, 2019), or due to impaired cytoskeletal force transduction due to deficits in
706 LINC components (Sohn *et al*, 2023). In addition, nuclear transport deficits have been reported
707 as a consequence of phosphorylated Tau accumulating at the outer nuclear envelope
708 (Hochmair *et al*, 2022; Kang *et al*, 2021).

709 Our data now reveal that the sole increase in physiological, soluble somatodendritic Tau – as
710 it occurs in physiological stress conditions and early in AD -, which is coupled to an increase
711 in nuclear Tau (Figure 2; (Sultan *et al*, 2011; Benhelli-Mokrani *et al*, 2018)), is sufficient to
712 induce NE distortions. The observed effects of Tau on the NE may at least in part be induced
713 by interactions of Tau with chromatin organizing proteins located in the inner nuclear
714 membrane. In particular, we identify LBR and the LINC component SUN1 as interactors of
715 Tau, both of which play important roles for the conditional NE association of genomic LADs
716 and the repression of genes contained in these. Notably, interactions of Tau with LBR have
717 been noticed previously (Jiang & Wolozin, 2021) but their consequences have not been further
718 investigated. We found that Tau-induced NE invaginations and nuclear, NE-enveloped cytosol
719 inclusions worsened when we enforced the interaction of Tau with LBR and SUN1 at the inner
720 nuclear membrane, suggesting that direct interactions of Tau with LBR and SUN1 can induce
721 this phenotype. Furthermore, DNA and HP1 proteins got enriched at the nucleoplasmic surface
722 of these NE invaginations and nuclear inclusions, indicating direct, local effects of these
723 structures on chromatin organization. These results suggest that nuclear Tau, even though
724 being manifold less concentrated than cytosolic Tau, can have pronounced effects on the NE
725 and associated chromatin organization.

726 For LBR, the interaction with Tau may involve biomolecular condensation of the two proteins
727 together with DNA, whereby even small amounts of Tau can efficiently alter the direct
728 interactions of LBR with DNA in the absence of HP1 “adaptor” proteins. We therefore propose
729 that Tau/LBR interactions with DNA may be independent of HP1. Our PLA data from cells,
730 neurons and human brain, however, indicated an interaction of Tau with HP1 proteins.
731 Furthermore, a recent study showed that Tau impacts the binding of HP1α to DNA *in vitro*
732 (Abasi *et al*, 2024). We currently cannot not rule out that Tau may also affect HP1-mediated
733 DNA-binding of LBR and other NE proteins. It further remains to be clarified, whether Tau can
734 change direct LBR/DNA interactions in a basepair sequence selective manner. Previously,
735 A/T-rich sequences have been shown to mediate Tau/DNA binding (Sjöberg *et al*, 2006), and
736 LADs are rich in AT as well (Meuleman *et al*, 2013), suggesting that adenine (A)-thymine (T)
737 base pairs may be responsible for the attraction of Tau to LAD sequences. Tau ChIPseq data
738 indicated genome-wide binding of Tau in coding and non-coding regions (~30% lncRNAs) and
739 suggested a gene repressor role of Tau in neurons under physiological temperature stress
740 (Benhelli-Mokrani *et al*, 2018).

741 ***Tau-induced chromatin re-organization at the NE. -*** Our data show that a physiologically
742 relevant increase in somatodendritic soluble Tau levels influences chromatin on multiple levels
743 (heterochromatin marks, spatial DNA distribution, chromosome positioning). In our data, the
744 "direction" (activation or repression) of chromatin changes seems, other than previously
745 suggested for AD brains and animal models with Tau aggregation pathology (Frost *et al*, 2014),
746 not unilateral but rather complex. The identified NE Tau interactors, LBR and SUN1, have
747 previously been implicated in regulating interphase chromatin on the level of CTs. LBR,
748 through interactions with the non-coding RNA Xist, couples the inactive ChrX to the lamina for
749 repression (Chen *et al*, 2016). SUN1, together with Emerin that we find to also potentially
750 interacts with Tau, was shown to be essential for positioning ChrX and Chr18 at the nuclear
751 periphery (Goelzer *et al*, 2025; Bikkul *et al*, 2019).

752 According to a role of nuclear Tau in modulating the interactions of LBR and SUN1 with
753 chromosomes, we find that increasing and/or removing Tau from neurons leads to nuclear
754 repositioning of chromosomes that have been reported to bind LBR or SUN1 or otherwise
755 locate near the NE in interphase nuclei, i.e., Chr1, Chr13, Chr18, and ChrX. To date, however,
756 no comprehensive CT mapping data in neurons (*in vitro* or in the brain) are available, neither
757 at base line nor in disease conditions. Comparative mapping of neuronal CTs (e.g., in AD vs.
758 control brains) in brain regions relevant for Tau pathology in AD, e.g., the hippocampus, would
759 be necessary to understand the actual contribution of Tau-induced CT alterations to disease-
760 associated gene expression changes.

761 Our transcriptomics data further supported the activity of Tau on chromosome-NE association,
762 showing that elevated Tau levels induce gene expression changes in T2-LAD genes in
763 chromosomes Chr13, Chr18, and ChrX. These findings are in line with observations in human
764 AD brain, where Tau-related genomic changes clustered in large genomic segments reflecting
765 spatial chromatin organization and nuclear lamina association (Klein *et al*, 2019). It remains to
766 be clarified though to which extend disease-driving gene expression changes in AD brains
767 relate to herein described early Tau missorting and/or to later Tau pathology, and whether they
768 depend on chromosome rearrangement or other chromatin regulatory mechanisms.

769 ***Tau - a nuclear regulator of neuronal cholesterol synthesis and metabolism? -*** The Tau
770 proximity biotinylation interactomics and the transcriptomics data sets from our study
771 converged in an unexpected way: a subset of (potential) nuclear interactors identified for Tau
772 where associated with cholesterol biosynthesis and mTORC1 signaling (STRING analysis of
773 biotinylated proteins significantly enriched in Tau over control; Figure 3H); the same occurred
774 for multiple genes significantly downregulated at elevated Tau levels (Hallmark pathway
775 analysis; Figure 8E). In fact, LBR, which we confirmed as NE Tau interactor, plays an essential
776 role in cholesterol synthesis by catalyzing the conversion from lanosterol to cholesterol (Tsai
777 *et al*, 2016). The unexpected convergence of interactomics and transcriptomics data in
778 cholesterol synthesis pathways suggests a function of Tau in regulating neuronal cholesterol
779 metabolism, thereby provide important new evidence on the consequence and reason for Tau
780 missorting induced by (patho)physiological stimuli.

781 Among the T2-LAD genes repressed at elevated Tau levels we found three key cholesterol
782 synthesis genes: *Hmgcs1* (3-Hydroxy-3-Methylglutaryl-CoA Synthase 1), catalyzing
783 condensation of acetyl-CoA and acetoacetyl-CoA to form HMG-CoA, and *Hmgcr* (HMG-CoA
784 reductase), both encoded on Chr13 and essential for the first steps in the mevalonate pathway.
785 In addition, we observed downregulation of *Nsdhl* (NAD(P)-dependent steroid dehydrogenase-
786 like; T2-LAD gene on ChrX), and *Mvd* (mevalonate diphosphate decarboxylase) and *Mvk*
787 (mevalonate kinase) to be downregulated. *Hmgcs1, Hmgcr, Mvd* and *Mvk* are all
788 transcriptionally regulated by SREBP2, a master regulator of lipid and cholesterol synthesis
789 gene expression that itself is activated at low cholesterol levels (Lewis *et al*, 2011). SREBP2
790 activity itself is regulated by mTORC1 (Peterson *et al*, 2011; Lewis *et al*, 2011), hence,
791 depends on the metabolic state of the cell. In our transcriptomics data, we find mTORC1
792 related pathways to be downregulated upon Tau overexpression, which indirectly suggests
793 reduced SREBP-2 activity. It remains to be tested though whether and through which
794 mechanisms Tau could regulate SREBP-2 activity. In any case, SERBP-2 metabolism could

be a potential therapeutic target (Lewis *et al*, 2011) to battle cholesterol and metabolic changes in the AD brain.

Cholesterol is a central component of membrane biology and lipid-based signaling. Downregulation of cholesterol synthesis can be observed in response to changing metabolic needs or environmental cues. For example, during periods of energy scarcity, cells shift their focus to conserving energy, e.g., by breaking down stored lipids for energy production and downregulating cholesterol synthesis to prevent the expenditure of energy on the synthesis of non-essential molecules like cholesterol. A neuronal strategy of "saving" energy by reducing cholesterol production would be in line with the observation that somatodendritic Tau levels (= Tau mis-sorting) occurs in conditions of energy-demanding neuronal hyperexcitation (Askin *et al*, 2024; Zempel *et al*, 2010; Tai *et al*, 2016). In addition to saving energy needed for cholesterol production, reducing cholesterol biosynthesis would have an additional effect on the neuronal energy metabolism by reducing neuronal activity: A decrease in neuronal cholesterol reduces synaptic activity (Shin *et al*, 2024), e.g., by reducing synaptic vesicle release (Mailman *et al*, 2011; Wasser *et al*, 2007). We speculate that Tau missorting under excitatory stress, followed by Tau-induced reduction in cholesterol biosynthesis, could put a break on excitation to avoid further overexcitation. However, extended cholesterol restriction, i.e., because of pathologically prolonged Tau missorting, could lead to synaptic decline and neurotoxicity in AD and tauopathies (Koudinov & Koudinova, 2001; Shin *et al*, 2024). Notably, *Igf1* (insulin growth factor-1), another important regulator of cell metabolism, appeared to be upregulated at high Tau levels as well, suggesting that Tau missorting may be involved in a global adaptation of the neuronal metabolism. Further studies are needed to test this currently speculative feedback loop.

Neurons receive most of their cholesterol in form of cholesterol/APOE lipoparticles from astrocytes. However, cholesterol synthesis by astrocytes could also be influenced by Tau since astrocytes themselves – as well as oligodendrocytes - also express low amounts of Tau. A Tau-related reduction of cholesterol synthesis in oligodendrocytes would impact myelin sheets, and therefore disturb neuronal transmission (Li *et al*, 2022). In addition, neuronal cholesterol synthesis seems to be essential for re-myelination processes in the brain (Berghoff *et al*, 2021), which becomes important in neurodegenerative diseases like AD, where de-myelination, leading to network activity abnormalities and promoting and amyloid-beta deposition (Depp *et al*, 2023), occurs early on. A-beta induced Tau missorting, leading to a reduction of neuronal and glial cholesterol synthesis, could therefore accelerate AD-related myelin deterioration and A-beta deposition, thereby creating a fatal feed-back loop with long-reaching consequences for neuronal network function in the brain. In addition, low cholesterol levels also promote neuronal internalization of seeding-competent Tau oligomers (Tuck *et al*, 2022), which could contribute to an accelerated spread of Tau aggregation pathology in the brain. Notably, our data indicate that Hmgcr protein levels are indeed reduced in AD hippocampal neurons having missorted Tau, and brain cholesterols levels have been reported to be reduced in AD (REF). Whether reduced cholesterol levels in AD brains are – at least partially - a consequence of neuronal Tau missorting, and whether this provides the missing link between AD-related A-beta and Tau pathology, myelination defects, and network dysfunction remains to be clarified.

Tau missorting - sufficient to induce AD-related neuronal stress response pathways? - Since somatodendritic missorting of Tau is considered to be upstream of Tau aggregation in AD (Luna-Muñoz *et al*, 2007), the herein investigated effects of high neuronal Tau levels should reflect initial, pre-pathological Tau changes in AD brains; they may also be interpreted as part of the physiological neuronal response to certain stress stimuli. Accordingly, we find that genes deregulated in response to Tau cluster in pathways of neuronal stress response that are also activated in AD and other neurodegenerative diseases (e.g., TNFα/NFKB signaling, apoptosis, p53 pathway). This includes, for example, the TFs *Rest, Crem*, and *Jun*, and the lncRNA *Neat1*. Furthermore, activation of stress response and pro-inflammatory signaling, including TNF-α/NFK-b signaling observed in neurons with high Tau levels, can induce the acute downregulation of biosynthetic pathways, including cholesterol production, to redirect resources away from non-essential processes like lipid synthesis. A direct link between Tau, neuronal stressors, and cholesterol synthesis still needs to be confirmed though.

850 Pathological conditions presenting with Tau missorting and aggregation in neuronal cell bodies
851 - e.g., neuronal hyperexcitation in seizures or as a result of A-beta in AD, mechanical brain
852 damage in traumatic brain injury (TBI) and chronic traumatic encephalitis (CTE) - often involve
853 repeated or extreme versions of physiological, Tau-activating stimuli. In these scenarios,
854 prolonged Tau missorting may exacerbate Tau's function in neuronal stress response leading
855 to neuronal silencing, synapse loss, and eventually neuronal death. This could explain why TF
856 regulation and gene expression changes reported in AD are in part contrary to what we
857 observe for neurons with elevated somatodendritic soluble Tau levels. In addition, the
858 sequestration of soluble Tau into aggregates. i.e., NFTs in AD, could prevent its nuclear activity
859 in regulating TFs and other genes, resulting in a discrepancy in gene expression data between
860 neurons with soluble physiological Tau and AD brains. Accordingly, it was suggested that a
861 loss of physiological nuclear Tau would lead to chromatin relaxation and alter transcription
862 (Rico *et al*, 2018; Mansuroglu *et al*, 2016). Previously observed differences in the effect of Tau
863 on gene expression in human neurons versus AD brains could be explained by this (Klein *et*
864 *al*, 2019).

865 In conclusion, our data implicate a novel function of missorted Tau in physically modulating
866 neuronal chromatin organization, preferentially at the NE and involving LBR and SUN1, to
867 induce stress-related gene expression profiles and reduce cholesterol biosynthesis.
868 Interactions of Tau with LBR and SUN1 (and potentially other NE proteins) seem also relevant
869 for Tau-related NE distortions and nuclear abnormalities observed in AD and FTD brains.
870 These findings propel the understanding of somatodendritic Tau missorting in both the
871 physiological neuronal context and as early, pre-pathological change in AD.

Figure Legends

Figure 1. Tau accumulation and nuclear envelope distortion in Alzheimer's disease (AD) brains.

(A) Misfolded Tau (Alz50+) near the nucleus in AD (39 cases) and control (24 cases) brain sections (70 nm-thick) of temporal cortex (BA20/21). Data shown as median±quartiles. Student's t-test with Mann-Whithey post-test. Scale bars = 10 µm.

(B) Representative images of immunolabeled nuclear envelope (NE) protein SUN1 and phospho-Tau (pS202/pT205/pT231) in neurons of AD brains (hippocampal CA1). Neurons with diffuse granular phospho-Tau staining in the soma show phospho-Tau "foci" in proximity to SUN1 in the NE (white arrowheads). Tangles (NFTs) do not show this Tau arrangement. Scale bars = 5 µm.

(C) AD and control brain nuclei showing nuclear membrane folds ("invaginations"). Data shown as mean±SEM, one data point per case. Student's t-test with Tukey post-test. Scale bars = 2 µm.

(D) Percent of neuronal nuclei having invaginations (nuclear membrane folds) in relation to the presence of misfolded/aggregated Tau near the nucleus in AD and control brains (related to Figure 1C). Data shown as mean±SD, n = number of nuclei as indicated. Two-tailed, unpaired Student's t-test comparing with and without Tau at nucleus within AD and Ctrl groups.

(E) Correlation between the percent of nuclei having nuclear invaginations and phospho-Tau near the nucleus in AD and control brain sections. Data points present individual cases, linear regression indicated.

(F) Illustration of nuclear alterations observed in AD brains. Neurons with Tau in the soma tend to have more NE invaginations. Small phospho-Tau "clusters" appear around the NE and insoluble Tau aggregates next to the nucleus.

Figure 2. Soluble Tau in the soma increases nuclear Tau and induces nuclear envelope damage

(A) Modulating Tau levels in primary mouse hippocampal neurons using adeno-associated viruses (AAVs). Overexpression of GFP-tagged human wild-type Tau (2N4R isoform) (Tau OE), FTD-mutant Tau^{P301L} (TauPL OE) or FTD-mutant $Tau^{P301L/S320F}$ (TauPL/SF OE) increases Tau levels compared to endogenous mouse Tau (Tau base), whereas the Tau (*MAPT*) gene silencing zinc-finger protein transcription factor (Wegmann *et al*, 2021) (ZFP90) decreases endogenous Tau levels (Tau KD). Note that neurons with AAV ZFP90-2a-GFP express GFP and ZFP90 as separate proteins due to the 2a self-cleavage site. Images show expressed GFP, immunolabeled MAP2, and DAPI in AAV transduced neurons (DIV12). In untreated neurons (Tau base), endogenous Tau was immunostained as well. Scale bars = 50 µm.

(B) Western blot of neuronal lysates (RIPA buffer extracts) showing, compared to Tau base neurons, increased soluble Tau levels in Tau OE, TauPL OE, and TauPL/SF OE neurons and reduced Tau levels in Tau KD neurons. Glia were removed from cultures by AraC treatment. data shown as mean±SD, n = 2 experiments. One-way ANOVA with Dunnett post-test.

(C) Quantification of Tau levels in neuronal somata and nuclei based on Tau immunofluorescence intensity. Positions of nuclei, determined from DAPI channel (not shown), are outlined in white. data shown as mean±SD, n = 3 images and 50-100 neurons per condition. One-way ANOVA with Dunnett post-test. Scale bars = 5 µm.

(D) Nuclear circularity determined based on Lamin A/C signal in hippocampal neurons with different Tau levels (Tau variant overexpression or Tau KD) compared to Tau base neurons. Representative images of Tau base (Tau immunostaining), Tau OE, TauPL OE, TauPL/SF OE, and Tau KD neurons. Nuclear circularity was quantified using Lamin A/C signal to define the nuclear boundary. n = 20-48 neurons per condition, data shown as mean±SD, one-way ANOVA with Tukey post-test. Scale bar = 1 µm.

(E) Schematic model of NE rupture and repair, showing local accumulation of BAF at sites of NE damage and subsequent recruitment of Emerin during the repair process.

(F) Tau constructs to test effect of (mostly) cytoplasmic or nuclear Tau on NE damage. Cytoplasmic: GFP-Tau, GFP-Tau^{P301L} and GFP-$Tau^{P301L/S320F}$. Nuclear (NLS): Tau-GFP–NLS, Tau^{P301L}-GFP-NLS, and $Tau^{P301L/S320F}$-GFP-NLS. Negative controls were untransfected or expressed GFP.

(G) Representative images of HEK293 cells co-expressing the GFP-labeled Tau constructs and SNAP-BAF. BAF accumulates at NE damage sites. Fluorescence intensity line plots along white dashed lines in BAF channel show colocalization of BAF and Emerin, indicating initiated NE repair processes in all conditions. Scale bars = 10 µm.

(H) Quantification of SNAP-BAF accumulation at the NE of HEK293 cells co-expressing GFP (control) or Tau constructs (see panel G) and SNAP-BAF. For each condition, the SNAP-BAF signal area at the NE was calculated for BAF+ cells. Data shown as mean±SD, normalized to controls (SNAP-BAF+GFP). n=15-20 cells per condition from 3 experiments. One-way ANOVA with Tukey post-test.

Figure 3. Nuclear Tau proximity labeling identifies nuclear envelope and nuclear transport proteins.

(A) Domain structures of human Tau (2N4R isoform) with indicated position of the P301L FTD-mutation in repeat R2. Tau domain structure shows the position of the N-terminal inserts, N1 and N2, and proline-rich regions P1 and P2 in the N-terminal projection domain, the 4 pseudo-repeats R1-R4 in the microtubule-binding domain.

(B) Workflow of nucleus-specific proximity biotinylation and identification of proteins associated with HA-TurboID-Tau, HA-TurboID-Tau^{P301L}, and HA-TurboID control. TurboID constructs are expressed in SH-SY5Y cells, biotinylation of interacting proteins enabled by addition of biotin to the culture medium. Nuclear biotinylated proteins are enriched through streptavidin pulldown from nuclear enriched fractions, followed by MS analysis.

(C) Expression of TurboID constructs in SH-SY5Y neuroblastoma cells. Anti-HA shows expression and cellular localization of HA-TurboID constructs, successful biotinylation is verified by anti-Streptavidin staining. Tau immunostaining detects both endogenous and recombinant Tau. Scale bars = 10 µm.

(D) Example western blot for streptavidin pull-down experiments. Anti-HA antibody detects TurboID constructs in nuclear lysates (input). Biotinylated proteins in streptavidin bead pull-down factions are detected with using anti-Biotin antibody. Histone-3 (H3) was used as loading control for nuclear fractions/inputs. Nuclear lysates from cells expressing TurboID fused to the C-terminal fragment of TDP-43 (TurboID-TDP-43ctf) were included as positive control.

(E) Volcano plots of proximity-biotinylated proteins in TurboID-Tau (left) and TurboID-Tau^{P301L} (right) each compared to TurboID only control. Significant differences between experimental groups and control were identified using a two-sided t-test. A log2[fold change] >1.5 and p-value < -log10[1] were used as threshold for significance. Selected interactors are indicated as orange data points and labeled with gene/protein identities. Data retrieved from 5 biological replicates.

(F) Venn diagram showing overlap of significant interactors between Tau and Tau^{P301L}.

(G) Pathway enrichment analysis (Gene ontology (GO), Cellular compartment) for Tau (left) and Tau^{P301L} (right).

(H) STRING analysis of potential Tau interactors (log2[fold change] >1.5 and p-value < -log10[1]) identified several functional clusters, corresponding to related biological modules (e.g., Integral component of nuclear inner membrane, regulation of endoplasmic reticulum (ER) organization, integral component of synaptic vesicle membrane, target of rapamycin complex 1 (TORC1), cholesterol biosynthesis, and phospholipid synthesis).

(I) STRING analysis of potential Tau^{P301L} interactors (log2[fold change] >1.5 and p-value < -log10[1]) identified several functional clusters, corresponding to related biological modules (e.g., Integral component of plasma membrane, microtubule transport, lipid synthesis, and L-type voltage-gated calcium channel complex).

(J) Heat map representing deregulation of selected nuclear envelope (NE) and nuclear transport proteins relative to TurboID control.

(K) Scheme showing identified potential Tau and TauP301L interactors in and at the nuclear envelope. Identified proteins can be categorized as (i) chromatin organizers in the NE (LEM2, LBR, EMD), (ii) structural membrane and nuclear pore complex (NPC) proteins (Nup210, NDC1, Nup155, Nup188, Nup205, Nup93), (iii) LINC complex proteins (SUN1, SYNE2), and (iv) nuclear transport receptors (XPO6, XPOT, TNPO2, IPO11).

Figure 4. Tau interacts with NE-associated chromatin organizers in cells, neurons, and the brain.

(A) Co-immunoprecipitation (Co-IP) of endogenous Tau with NE proteins Nesprin, Lamin A/C and LBR in SH-SY5Y cell lysates using high-salt buffer for cell lysis. Input (total lysate) and pulldown (IP) samples for NE proteins and control IgG are shown. The flow-through (FT) fraction is also included. Tau is detected at ~55 kDa. Intensity line plots along gel lanes (direction indicated by dashed lines) show increased signal over background for LBR.

(B) Co-IP of SUN1 and LBR with GFP-Tau in SH-SY5Y cell lysates using high-salt buffer for cell lysis.

(C) Principle of proximity ligation assays (PLAs) for *in situ* detection of proteins in close proximity (<40 nm) to Tau.

(D) Positive and negative controls for endogenous Tau PLAs in naive SH-SY5Y cells. The negative control (Tau+IgG) shows few unspecific fluorescent PLA signal spots, whereas the Tau positive control using two Tau antibodies (Tau-13+Tau DAKO) results in high PLA signal throughout the cell body. The positive control for nuclear envelope localization, LaminA/C+SUN1, leads to PLA signal around the nucleus. Scale bars = 10 µm.

(E) PLA of endogenous Tau with NE proteins in SH-SY5Y cells. Quantification of PLA signal per nucleus indicate Tau proximity to SUN1 and Nesprin-2. PLA signal quantified in nuclear ROIs. n = 200-400 nuclei per condition. One-way ANOVA with Dunnett post-test. Scale bars = 10 µm.

(F) PLA of endogenous Tau with inner NE proteins in SH-SY5Y cells. Quantification of PLA signal per nucleus indicated Tau proximity to Emerin and LBR. PLA signal quantified in nuclear ROIs. n = ~200 per condition. One-way ANOVA with Dunnett post-test. Scale bars = 10 µm.

(G) PLA of endogenous Tau with intranuclear proteins in SH-SY5Y cells. Quantification of PLA signal per nucleus validates HP1γ as interactor of Tau. PLA signal was quantified in nuclear ROIs. n = ~300 nuclei per condition. One-way ANOVA with Dunnett post-test. Scale bars = 10 µm.

(H) PLA of endogenous Tau in mouse hippocampal neurons (DIV12). The negative Control (Tau+IgG) leads to few unspecific fluorescent spots, whereas Tau positive control (Tau-5+Tau DAKO) results in high PLA signal throughout the soma and projections. PLA signal quantified in nuclear ROIs. Note, strong PLA signal is produced for Tau+LBR and Tau+HP1γ, but not for MAP2+LBR and MAP2+HP1γ. n = ~50 nuclei per condition. One-way ANOVA with Dunnett multiple comparison test. Scale bars = 10 µm.

(I) Immunostaining of potential Tau interactors (SUN1, LBR, HP1γ) in human AD brain sections (hippocampal CA1). Zoom-ins show selected neuronal nuclei/cell bodies having different phospho-Tau (pS202/pT205/pT231) levels and aggregation states. Note, LBR seems to co-aggregate with p-Tau in NFTs in neuronal somata (arrow heads in zoom-ins). Scale bars = 10 µm.

(J) Immunostaining for MAP2 (cyan) and total Tau (pink) in combination with PLAs (yellow) for total Tau with SUN1 (left), LBR (middle), and HP1γ (right) in AD brain sections (hippocampal CA1 and dentate gyrus). White squares indicate location of zoom-ins shown below for combined IHC+PLA and PLA with DAPI. Scale bars = 10 µm.

(K) PLA negative controls (SUN1 only, hippocampal CA1; SUN1+PSD-95, dentate gyrus) show no PLA signal in human brain. Scale bars = 10 µm.

Figure 5. Tau induced NE invaginations and cytoplasm-filled nuclear inclusions.

(A) Tau-induced nuclear envelope (NE) invaginations and nuclear inclusions in HEK293 cells. Cells expressing iRFP670–Tau or mRFP-FKBP-Tau alone, or in combination with LBR–eCFP–SNAP (left) or SUN1–eCFP–SNAP (right) in the absence or presence of the chemical coupler rCD1 inducing FKBP-SNAP binding. Normalized fluorescence intensity line plots along white lines in merged images illustrate the spatial relationship between Tau, LBR or SUN1, and DNA in/at NE invaginations and inclusions. Scale bars = 10 µm.

(B) Percentage of cells with NE invaginations and/or inclusions (left) upon mRFP-FKBP-Tau overexpression alone or in combination with LBR-eCFP-SNAP or SUN1-eCFP-SNAP, with and without rCD1 addition. Fractions of cells having NE invaginations or inclusions (right) in mRFP-FKBP-Tau plus SUN1-eCFP-SNAP (Tau+SUN1) and mRFP-FKBP-Tau plus LBR-eCFP-SNAP (Tau+LBR) expressing cells, with and without rCD1 treatment. Data shown as mean±SD, N=20-99 cells from 3 experiments, one-way ANOVA with Tukey post-test.

(C) Co-localization of NE proteins with nuclear Tau inclusions. Cells co-expressing mRFP–FKBP–Tau and SUN1–eCFP–SNAP were immunostained for endogenous NE proteins LBR, Lamin B1, Lamin A/C, and nuclear pore complex (NPC). White squares indicate regions shown at higher magnification. Scale bar = 10 µm.

(D) Co-localization of cytoplasmic proteins with nuclear Tau inclusions. Cells co-expressing mRFP–FKBP–Tau and SUN1–eCFP–SNAP were immunostained for cytoplasmic proteins (vimentin, GAPDH, and β-tubulin). White squares indicate regions shown at higher magnification. Scale bar = 10 µm. Box shows proposed model for transition of invaginations into nuclear cytoplasm inclusions

(E) Tau nuclear inclusions in relation to nuclear organelle markers. Cells co-expressing mRFP–FKBP–Tau and LBR–eCFP–SNAP (left) or SUN1–eCFP–SNAP (right) were immunostained for nucleolar markers NPM1, nuclear speckle protein SRRM2, and chromatin binding protein HP1γ. White

squares indicate regions shown at higher magnification used for normalized intensity line plots. Scale bar = 10 µm.

Figure 6. Tau changes LBR-npd condensates and its binding to DNA.

(A) Schematics of the inner nuclear membrane protein LBR and the interaction of its N-terminal nuclear projection domain (npd) with DNA - direct or via HP1 proteins. In addition, PONDR predictions of protein disorder along the peptide sequences of LBR, HP1γ and Tau are shown. LBR-npd, the central region of HP1γ, and Tau's N-terminal projection domain are largely disordered (PONDR > 0.5).

(B) SDS-PAGE of purified recombinant Tau, LEM2-npd, LBR-npd, and HP1γ used for *in vitro* assays.

(C) LBR-npd (including 1% LBR-npd-Dylight488) condensation in the presence and absence of HP1γ (including 1% HP1γ-Dylight555), Tau (including 2% Tau-Dylight650), or both. Left: in the absence of DNA, LBR-npd readily forms grape-like assemblies of spherical condensates, into which HP1γ and Tau co-partition. In the presence of λ-DNA (right), LBR-npd attaches to and bundles DNA. HP1γ joins LBR-npd on thin DNA threads an in thicker LBR-npd condensates. Tau is found only in condensed LBR-npd on DNA. Scale bars = 10 µm.

(D) Control conditions showing no condensation of HP1γ, Tau, or both with and without λ-DNA in the used assay buffer conditions. Scale bars = 10 µm.

(E) FRAP of LBR-npd shows liquid-like recovery in the absence of DNA, whereby HP1γ and Tau reduce the mobile fraction of LBR-npd independently and co-cooperatively. Bound to DNA, LBR-npd shows no FRAP regardless of the absence or presence of HP1γ and/or Tau. Data shown as mean±SD, n=10-15 condensates per condition from 3 experiments. One-way ANOVA with Tukey post-test comparing the average of last 10 mean values of each condition. Scale bars = 1 µm.

(F) Electrophoretic mobility shift assays (EMSA) of LBR-npd (400 ng) binding to DNA (500 bp, 20 ng) in the presence of 0, 25, 50, or 75 ng Tau. Upshift of DNA signal in gel lanes (blue/green rectangles) indicates binding of added proteins to DNA. Unbound DNA runs at the lower end of the gel (pink rectangle). Bottom: Quantification of % bound DNA upon addition of LBR-npd and Tau (blue), or Tau only (green). N=2 independent experiments.

Figure 7. Somatodendritic and nuclear soluble Tau induces heterochromatin alterations.

(A) Modulation of Tau levels in primary mouse hippocampal neurons via adeno-associated viruses (AAVs) used to study heterochromatin alterations. Overexpression of GFP (endogenous Tau levels, Tau base), GFP-tagged human wild-type Tau (2N4R isoform) (Tau OE), FTD-mutant GFP-Tau^{P301L} (TauPL OE), or the gene silencing zinc-finger protein transcription factor (Wegmann *et al*, 2021), ZFP90, that decreases endogenous Tau levels (Tau KD).

(B) Histone modifications associated with gene repression (H3K9me3) and gene activation (H3K9ac).

(C) H3K9me3 chromocenter number in neurons with different Tau levels. n = number of nuclei (indicated), 3 biological replicates, and 3 images analyzed per condition. One-way ANOVA with Dunnett post-test. Scale bars = 10 µm.

(D) H3K9ac immunofluorescence intensity in neurons with different Tau levels. n = number of nuclei (indicated), 3 biological replicates, and 3 images analyzed per condition. One-way ANOVA with Dunnett post-test. Scale bars = 10 µm.

(E) DNA (siR-DNA) distribution in nuclei of neurons with different Tau levels. Representative images of individual nuclei for each treatment. Line-scan intensity profile (middle right) show siR-DNA intensity along white dashed lines in images. Lower right: Radial DNA profiles (clock scan analyses; n= 5-13 nuclei) show DNA enrichment at the nuclear envelope in Tau OE and TauPL OE compared to Tau base and Tau KD neurons. Scale bars = 5 µm.

(F) FLIM of siR-DNA in neurons with different Tau levels. Compaction/condensation of DNA correlates with a decrease in siR-DNA lifetime. Representative intensity and lifetime maps of nuclear ROIs are shown for GFP (Tau base) and GFP-Tau (Tau OE) expressing neurons. White arrows indicate position of chromocenters. Middle and right: Quantification of most probable SiR-DNA lifetimes for nuclear sub-compartments: Chromocenters (ChrC), open chromatin (opChr), and nuclear envelope (NE). Note that Tau OE and TauPL OE nuclei show increased siR-DNA lifetime in ChrCs. n = 11-17 nuclei per condition from two experiments. Data shown as ChrC, NE, and opChr for individual nuclei (before/after plot; Two-way ANOVA with Tukey post-test) and for comparison of NE and ChrC between groups (box-whisker plots, median with 5-95 percentile, one-way ANOVA with Tukey post-test.

(G) Representative chromosome FISH images collected from non-transduced (Tau base), Tau OE, and Tau KD neurons show the positioning of chromosome territories (CT) in the equatorial plane of neuronal nuclei for chromosomes ChrX, 1, 13, and 18. DNA (DAPI) is shown in blue, CTs in green. Scale bar = 10 µm.

(H) Radial positioning of chromosomes ChrX, 1, 13, and 18 in the equatorial plane of neuronal nuclei with different Tau levels. Radial positioning of Chr's was determined by measuring the absolute FISH signal intensity across concentric nuclear shells from the nuclear interior (1–20%) to the periphery (81–100%). N = 9-19 nuclei per condition, two-way ANOVA with Tukey post-test.

Figure 8. Impact of Tau levels on neuronal transcription

(A) Schematics of RNAseq (total RNA, rRNA depletion) in Tau base, Tau OE, and Tau KD neurons.

(B) Number of significant DEGs in Tau OE and Tau KD compared to Tau base, and Tau OE compared to Tau KD neurons. Data were collected from N = 5-6 neuronal cultures.

(C) Heatmap of significant differentially expressed genes (DEGs) in Tau OE, Tau KD and Tau base neurons.

(D) Volcano plots of DEGs in Tau OE vs Tau base, and Tau KD vs Tau base neurons. Threshold of significance was set to log2[Fold Change] > 1 and adjusted p-value < 0.05. Names of selected genes (mouse) are indicated.

(E) Gene set enrichment "Hallmark" for all DEGs. Up and down-regulated hallmark pathways are shown for Tau OE vs Tau base, and Tau OE vs Tau KD.

(F) Gene ontology (GO *Biological Processes*) of significant DEGs in Tau OE compared to Tau base neurons are shown separately for up- (top) and down (bottom)-regulated DEGs.

(G) Networks of transcription factors (TFs) among significant DEGs in Tau OE vs. Tau base neurons, grouped by their (main) activity as transcriptional repressors and activators. Notably, except *Neurod6* and *Foxo6*, all TFs are upregulated in Tau OE neurons (see Figure EV10B). Quantitative PCR (qPCR) of selected genes (*hmgcs1, nsdhl* and *tgif1*) involved in cholesterol biosynthesis in Tau base and Tau OE neurons. Expression values were determined from RNA isolated from neuronal cultures and normalized to GAPDH expression. Data shown as mean±SD, n=3 experiments.

(H) Hmgcr protein levels are reduced in AD brain. Representative immunofluorescence images and quantification of Hmgcr signal intensity in neuronal somata in control and AD hippocampal sections. Student's t-test. For AD, signal intensity of neurons having no phosphorylated Tau (no p-Tau), diffuse p-Tau, or aggregated p-Tau in neurofibrillary tangles (NFTs) are compared as well. One-way ANOVA with Tukey post-test. Scale bar = 50 µm.

(I) LAD association of DEGs in Tau OE compared to Tau base neurons. Of 142 total DEGs, 22 DEGs (15%) are located in LADs type1 and 57 DEGs (40%) are located in LAD type2. Selected gene names of DEGs for each LAD type are indicated. LAD type2 genes include cholesterol biosynthesis genes *Hmgcr*, *Hmgcs1*, and *Nsdhl* that are downregulated in Tau OE neurons.

(J) Chromosome location of DEGs in Tau OE compared to Tau base (left) or Tau KD (right) neurons, for up- and down-regulated and all DEGs. Number in heat map gives exact number of DEGs in chromosomes.

(K) Gene names of DEGs overlapping with LAD type2 and significantly enriched in chromosomes Chr13 and ChrX for Tau o/e versus Tau base neurons, and in chromosomes Chr13, 18, and X for Tau OE vs. Tau KD neurons.

(L) Chromosomal distribution of LAD-associated DEGs. DEGs in LADs type2 are distributed across Chr1-19 and ChrX. Significant enrichment of LAD type2 DEGs occurs in chromosomes Chr13 and ChrX for Tau OE compared to Tau base neurons (left), and in chromosomes Chr13, Chr18 and ChrX for Tau OE compared to Tau KD neurons (right).

Expanded View Figure Legends

Figure EV1. Additional data for AAV-mediated modulation of Tau levels in hippocampal neurons.

(A) Representative images of primary mouse hippocampal neuron cultures (DIV12), in which Tau levels were modulated using AAVs added on DIV5. Total Tau is detected by immunofluorescence. AraC treatment was used to deplete glia cells in cultures. Scale bars = 20 µm.

1148 (B) Schematics AAV ZFP72, a non-gene targeting control AAVs for the MAPT-silencing ZFP90. Scale
1149 bar = 50 µm
1150 (C) Tau level variation in cell bodies (= soma) of hippocampal (CA1) neurons of AD brain. Levels were
1151 determined based on total Tau immunofluorescence in cell bodies outlined in the MAP2 channel
1152 and normalized to tissue background measured in neuropil. Data points represent individual cell
1153 bodies in the image shown, as indicated by the colored circles.
1154 (D) Full western blots to determine Tau levels in neuronal lysates (related to Figure 2B).

1155 **Figure EV2. Additional data for Tau and TDP-43ctf nuclear proximity labeling.**

1156 (A) Full western blots (anti-HA, H3 and Biotin) for nuclear-enriched cell lysates (input), related to Figure
1157 3D.
1158 (B) Full western blots for nuclear-enriched cell lysates (input) and pulldown (Streptav.PD), related to
1159 Figure 3D.
1160 (C) Domain structure of full-length TDP-43, comprised of an N-terminal domain harboring a nuclear
1161 localization signal (NLS), two RNA-binding domains (RRM1+2, with a nuclear export signal (NES)
1162 in RRM2), and a C-terminal domain. Aggregation-prone TDP-43ctf (C-terminal fragment, aa 208-
1163 414) is generated in the brain via autocleavage at amino acid R208. TurboID constructs and
1164 workflow for proximity biotinylation of potential nuclear TDP-43ctf interactors.
1165 (D) Expression of TurboID-TDP-43ctf construct in SH-SY5Y neuroblastoma cells. Anti-HA staining
1166 (cyan) shows expression and cellular localization of HA-TurboID construct, successful biotinylation
1167 (magenta) is verified by anti-Streptavidin staining. TDP-43 staining was included (yellow). Scale
1168 bars = 10 µm.
1169 (E) Volcano plots of proximity-biotinylated proteins associated with TurboID-TDP-43ctf compared to
1170 TurboID control. Significant differences in proteins between experimental groups and control were
1171 identified using a two-sided t-test. A log2[fold change] >1.5 and p-value < -log10[1] were used as
1172 threshold for significance. Selected interactors are indicated as orange data points and labeled with
1173 protein names. Data retrieved from 5 biological replicates.
1174 (F) Pathway enrichment analysis (GO Cellular compartment) for proteins biotinylated by TurboID-TDP-
1175 43ctf.
1176 (G) Venn diagram showing overlap of biotinylated proteins significantly enriched in TurboID-Tau,
1177 TurboID-Tau^{P301L}, and TurboID-TDP-43ctf compared to TurboID control (created with
1178 https://bioinfogp.cnb.csic.es/tools/venny/)
1179 (H) Pathway enrichment analysis (ORA, over-representation analysis, Gene ontology (GO), Biological
1180 Processes analysis of potential nuclear Tau (left), TauP301L (middle), and TDP-43ctf (right)
1181 interactors.

1182 **Figure EV3. Additional data for Tau co-IPs and PLAs in cells and neurons.**

1183 (A) Full western blot of endogenous Tau Co-IP with Nesprin, LaminA/C and LBR (related to Figure 4A).
1184 (B) SH-SY5Y cells expressing GFP or GFP-Tau for co-IP of NE proteins using GFP-Trap beads.
1185 (C) Full western blot of LBR Co-IP with GFP-Tau in different buffer conditions (related to Figure 4B).
1186 (D) Full western blots of SUN1 co-IP with GFP or GFP-Tau in high salt buffer (related to Figure 4B).
1187 (E) PLA of endogenous Tau with H4K20me3 or H3K9me3 in SH-SY5Y cells. PLA signal was quantified
1188 in nuclear ROIs. N = ~300 nuclei. One-way ANOVA with Dunnett post-test. Scale bars = 10 µm.
1189 (F) PLAs of endogenous Tau with heterochromatin markers in hippocampal neurons (DIV12). PLA
1190 signal was quantified in nuclear ROIs. Scale bars = 10 µm.

1191 **Figure EV4. Additional data for human brain IHCs and PLAs.**

1192 (A) Example low magnification overview images of human brain sections immunolabeled for MAP2,
1193 phospho-Tau (pS202/pT205/pT231 or pT205/pS199), and respective Tau interacting nuclear
1194 envelope protein (SUN1, LBR or HP1γ in hippocampal CA1; LEM-2 in cortex). Scale bars = 100
1195 µm.
1196 (B) Representative image of immunofluorescently labeled Tau interactor LEM-2 in cortical sections from
1197 human AD brain. Zoom-ins show selected neuronal nuclei/cell bodies (MAP2+) having different
1198 phospho-Tau (pS202/pT205/pT231) levels and aggregation states. Scale bar = 10 µm.
1199 (C) "Cart wheel"-like DNA structure in neuronal nuclei of human hippocampus. Example images of AD
1200 hippocampal section labeled for phospho-Tau (p-Tau), MAP2, and DNA (DAPI). At higher
1201 magnification (white boxes; zooms show inverted DAPI signal), the cart wheel like DNA
1202 arrangement in the nuclei becomes visible. Quantification of Cart wheel-like neuronal DNA
1203 arrangement in AD vs. control brain hippocampi. Data shown as mean±SD, data points indicate 8-

11 images analyzed from three 3 AD/Ctrl cases. Unpaired Student's t-test. Scale bar = 20 µm. Bottom: Example image and radial DNA profile (clock scan) of neuronal cart wheel DNA arrangement.

(D) Immunostaining for MAP2 (cyan) and total Tau (pink) in combination with PLA (yellow) for endogenous Tau with LEM-2 in AD brain sections (hippocampal CA1 and dentate gyrus). White squares indicate location of zoom-ins shown below for combined IHC+PLA and PLA with DAPI. Scale bars = 10 µm.

Figure EV5. TauP301L induced cytoplasm-filled nuclear NE invaginations

(A) HEK293 Cells expressing eGFP–TauP301L alone, or mRFP–FKBP–TauP301L co-expressed with LBR–eCFP–SNAP or SUN1–eCFP–SNAP in the absence or presence of rCD1, are shown. Normalized fluorescence intensity line plots along white lines in merged images show spatial distribution of Tau, LBR or SUN1, and DNA. Scale bar = 10 µm.

(B) Co-localization of TauP301L nuclear inclusions with nuclear organelle markers. Cells co-expressing mRFP–FKBP–TauP301L and either LBR–eCFP–SNAP (top) or SUN1–eCFP–SNAP (bottom) were immunostained for the nucleolar NPM1, nuclear speckle protein SRRM2, or chromatin binding HP1γ. White boxes indicate location of enlarged regions shown on the right. Normalized intensity line plots are generated along dashed white lines. Note, HP1γ is enriched around inclusions where DNA (see panel A) is condensed as well. Scale bar = 10 µm

Figure EV6. Additional data for LBR-npd condensation and DNA binding.

(A) Disorder (PONDR > 0.5) and LLPS propensity (CatGranule > 0.75) of identified (potential) nuclear Tau interactors.

(B) PhaSePred meta-prediction (10-feature model) for potential nuclear Tau interactors.

(C) Representative overview images showing LBR-npd coating of λ-DNA in the absence and presence of HP1γ and/or Tau. Scale bars = 10 µm.

(D) LBR-npd mobile fractions in the absence and presence of λ-DNA, determined from last 10 data points of average FRAP curves in Figure 5K. One-way ANOVA with Tukey post-test.

Figure EV7. Heterochromatin analysis in neurons with different Tau levels.

(A) Workflow of H3K9me3 chromocenter analysis in neuronal nuclei. Projections of z-stacks covering the entire nucleus were analyzes using CellProfiler: Primary objects (Nuclei from DAPI channel) were identified, position and size of chromocenters detected in H3K9me3 channel applying a size threshold (5-10 pixels).

(B) Quantification of H3K9me3 chromocenter number in neurons with different Tau levels. N = number of nuclei (indicated), 3 biological replicates, and 3 images analyzed per condition. One-way ANOVA with Dunnett post- test.

(C) Western blot of heterochromatin markers shows increased repressive H3K9me3 levels in Tau OE and TauPL OE neurons. H3K9ac changes are not significant. n = 3 experiments. One-way ANOVA with Dunnett post-test.

(D) Full blots for data analyzed in S7C.

Figure EV8. Neuronal cultures and PCA of RNAseq samples.

(A) Immunostaining shows reduction of astrocytes/glia cells without impairing neuronal integrity after treatment with AraC (1 µM, 8 h). Scale bar = 50 µm.

(B) Principal component analysis (PCA) of RNAseq data per condition (Tau base, Tau OE, Tau KD).

(C) Adjusted R^2 values from linear regression for each batch used for RNAseq.

(D) Batched-corrected gene expression of *MAPT* across the conditions.

Figure EV9. Additional analysis of DEGs in neurons with high and low Tau levels.

(A) Number of differentially expressed genes (DEGs) by gene classes for Tau OE versus Tau base, Tau KD versus Tau base, and Tau OE versus Tau KD neurons.

(B) Gene set enrichment analysis (GSEA) of all DEGs in Tau o/e versus Tau base and Tau OE vs. Tau KD neurons using GO Biological processes.

(C) Non-protein coding DEGs in Tau OE versus Tau base, Tau OE versus Tau base, and Tau OE vs. Tau KD neurons organized by condition and classes.

Figure EV10. Transcription factor (TF) analysis

(A) UniProt keyword enrichment analysis of transcription factors. Bubble plot showing significantly enriched UniProt annotated keywords identified by STRING analysis of transcription factors differentially regulated in the RNAseq dataset of Tau OE vs Tau base (see Figure 8G). Enriched categories include Activator, Repressor, DNA-binding, and Transcription regulation. The x-axis indicates the enrichment signal. Bubble size represents the number of genes associated with each keyword, and color denotes the false discovery rate (FDR).

(B) Table summarizing transcription factors (TFs) identified among significant DEGs in Tau OE vs Tau base neurons, obtained by comparison with the AnimalTFDB v4.0 database. For each TF, chromosome location, regulatory activity (activator or repressor), direction of regulation (up- or downregulated), log2(fold change, FC), and p-value are indicated. Functional clustering of transcription factors into activators and repressors was derived from STRING protein–protein interaction analysis.

(C) Transcription factor (TF) analysis (wPGSA) of RNA sequencing data considering all gene expression data except transposable elements. Positive wPSGA t-score of a TF indicates overall upregulation of its target genes, a negative wPSGA t-score an overall down-regulation of the target genes. Threshold of significance was set as [wPSGA t-score] >4 and adjusted p-value < 10^{-5}. Nomenclature from wPGSA analysis was used.

Figure EV11. CUT&Tag for H3K9ac.

(A) Experimental outline for CUT&Tag.

(B) Heat map of significant enriched H3K9ac loci in different genomic regions, clustered by condition.

Figure EV12. LAD type 1 association of DEGs in neurons with high Tau levels.

DEG association with LAD type1 and chromosomes for Tau OE vs. Tau base (top) or Tau OE vs. Tau KD (bottom) shows no significant enrichment of DEGs in LAD type1.

1283 **Material and Methods**

1284

1285 *Human samples*

1286 DAPI and Tau imaging: Images of AD and control brain array tomography sections stained for
1287 misfolded Tau (Alz50) and DAPI were provided by Prof. Tara Spires-Jones (Centre for
1288 Discovery Brain Science, University of Edinburgh). The use of human tissue for these post-
1289 mortem studies was reviewed and approved by the Edinburgh Brain Bank ethics committee
1290 and the medical research ethics committee. Post-mortem brains of 61- to 96-year-old (24
1291 female, 41 male) AD patients (Braak V-VI, n=40) and healthy controls (n=25) were used
1292 (Supplemental Table T10).

1293 IHC and PLA: Post-mortem, FFPE-fixed AD and control brain samples for IHC and PLA were
1294 received from the Biobank of the Department of Neuropathology, Charité-Universitätsmedizin
1295 Berlin, Germany (Supplemental Table T11). All experiments performed were approved by the
1296 local ethics committee at the Charité Berlin, patient consensus to the use of the tissue was
1297 given to the biobanks the tissue was received from.

1298

1299 *Animals*

1300 All experiments involving mice were carried out according to the guidelines stated in the
1301 directive 2010/63/EU of the European Parliament on the protection of animals used for
1302 scientific purposes and were approved by local authorities in Berlin and the animal welfare
1303 committee of the Charité university in Berlin, Germany.

1304

1305 *Plasmid constructs*

1306 Mammalian expression plasmids:

1307 Tau (human full-length wild-type Tau, 2N4R isoform), FTD-mutant Tau^{P301L}, and TDP-43ctf
1308 (aa208-414) were cloned into 3xHA-TurboID-NLS_pCDNA3 plasmid (Addgene #107171)
1309 under a CMV promotor. The TurboID-NLS_pCDNA3 backbone was cut with EcoRI/XhoI to
1310 remove the NLS sequence and enable cytoplasmic expression and localization. Tau, Tau^{P301L}
1311 or TDP-43ctf inserts were PCR-amplified from different sources (key resource table) and
1312 inserted into the backbone using Gibson Assembly cloning. A flexible linker [(SGGG)]3 was
1313 inserted between TurboID and the fusion partners to enable correct protein folding. 3xHA-
1314 TurboID was cloned from 3xHA-TurboID-NLS_pCDNA3 plasmid (Addgene #107171) using
1315 EcoRI to remove the NLS sequence, followed by blunting using T4 polymerase and ligation
1316 using T4 ligase.

1317 The eGFP-Tau (human, 2N4R) sequence was subcloned from a pRK5 backbone (kindly
1318 provided by Eckhard Mandelkow) into an AAV vector with CAG promotor. GFP-Tau^{P301L} and
1319 GFP-Tau$^{P301L/S320F}$ were generated by site directed mutagenesis. Tau-GFP-NLS was
1320 generated by fusing GFP-3xNLS (three tandem repeats of a classical SV40 large T-antigen
1321 nuclear localization signal (DPKKKRKV)\$_3$) C-terminally to full-length human Tau (2N4R),
1322 separated by a 3xGSSS linker. Tau^{P301L} and Tau$^{P301L/S320F}$ variants were generated by site
1323 directed mutagenesis.

1324 For iRFP670-Tau or iRFP670-Tau^{P301L}, human full-length Tau (2N4R) or Tau^{P301L} were fused
1325 to PCR amplified iRFP670 (Addgene #45466) and inserted into a pRK5-EGFP backbone with
1326 CMV promotor (Addgene #46904) using Gibson Assembly cloning.

1327 For mRFP-FKBP-Tau or mRFP-FKBP-Tau^{P301L}, human full-length wild-type Tau (2N4R) or
1328 Tau^{P301L} were cloned into a pmRFP-FKBP-PRPF38A backbone carrying a CMV promotor
1329 (kindly provided by Florian Heyd, FU Berlin). SUN1 (aa1-916) and full-length LBR were fused
1330 to eCFP and SNAP.

1331 AAV constructs:

1332 Plasmids for eGFP, eGFP-Tau, eGFP-Tau^{P301L}, eGFP.p2a.ZFP90, and eGFP.p2a.ZFP72
1333 were sub-cloned into an AAV backbone using standard cloning procedures. Genes for ZFP90
1334 and ZFP70 were synthesized based on their published protein sequence (Wegmann *et al*,
1335 2021). AAV particles (AAV 2/9 PhP.B) were produced by the Charité viral core facility (VCF).

1336

1337 *Cell culture and transfection*

1338 Human SH-SY5Y cells obtained from ATCC (CRL-2266) were cultured in DMEM (Life
1339 Technologies) containing 10% FBS, 1% Pen/Strep (Sigma-Aldrich) and 2 mM L-Glutamine
1340 (ThermoFisher) and maintained at 37°C and 5% CO2. Cells were grown in 10 cm dishes (60-
1341 70% confluency) for proximity biotinylation pulldowns as well as co-immunoprecipitations (co-
1342 IPs)/WBs and in µ-slide 8-well imaging dishes (ibidi; ibiTreat) for proximity ligation assays
1343 (PLA) and immunofluorescence (IF). Cells were transfected with Lipofectamine 2000 (Life
1344 Technologies) according to the manufacturer's protocol.

1345 Human HEK-293 cells obtained from ATCC (CRL-1573) were cultured in DMEM (Life
1346 Technologies) containing 5% FBS and 1% Pen/Strep (Sigma-Aldrich) and maintained at 37°C
1347 and 5% CO2. Cells were passaged in 0.05% Trypsin-EDTA (Life Technologies) and plated in
1348 µ-slide 8-well imaging dishes (ibidi; ibiTreat) for immunofluorescence (IF) and for co-
1349 transfection of Tau with LBR/Sun1.

1350

1351 *Primary hippocampal neurons*

1352 *Primary mouse neurons* were prepared from hippocampi dissected from P0-P1 wildtype mice
1353 (C57/B6) of either sex. Hippocampi were dissected in ice-cold HBSS (Millipore) containing 1%
1354 P/S. Hippocampal tissue was digested in enzyme solution (DMEM, ThermoFisher Scientific)
1355 with 3.3 mM Cystein, 2 mM $CaCl_2$, 1 mM EDTA and papain (20U/ml, Worthington) at 37°C for
1356 30 min. Papain reaction was inhibited by incubating digested hippocampi in DMEM containing
1357 10% FBS (ThermoFisher Scientific), 1% P/S, 38 mM BSA, and 95 mM trypsin inhibitor at 37°C
1358 for 5 min. Cells were triturated in complete Neurobasal-A (NBA) medium containing 10% FBS,
1359 2% B-27, 1% Glutamax, 1% penicillin/streptomycin (P/S) and seeded in PLL (0.1 mg/mL)
1360 coated glass bottom µ-slide 8-well imaging dishes (ibidi) at a seeding density of ~30'000
1361 cells/cm^2 (for IF/PLA experiments). For Neuronal nuclear levels of Tau, Cut&Tag and RNA
1362 sequencing experiments, cells were seeded into PLL-coated 6-well dishes (300'000 cells/dish).
1363 Every second day, one-fifth of the media was replaced by fresh complete NBA medium.

1364 *AraC treatment:* To inhibit glial proliferation and obtain mostly neuronal cultures, seeded cells
1365 were subjected to a treatment with cytosine arabinoside (AraC) on DIV2. For that, 50% of the
1366 medium was removed and kept at 4°C as conditioned medium. Cells were treated with 1 µM
1367 (f.c.) AraC for 8 h at 37°C. Then, 80% of the medium containing AraC was removed and
1368 conditioned and fresh medium added to obtain the final volume. Success of AraC treatment
1369 was exemplary verified by immunostaining with anti-GFAP, anti-MAP2, and anti-Tau
1370 antibodies, showing almost full removal of astrocytes without obvious neurotoxicity.

1371 *AAV transduction:* AAV particles for Tau expression (AAV CAG.eGFP-Tau, AAV CAG.eGFP-
1372 Tau^{P301L}, AAV CAG.eGFP-Tau$^{P301L/S320F}$), GFP expression (AAV CAG.eGFP), knockdown of
1373 endogenous mouse Tau (AAV hSyn.ZFP90-p2A-eGFP and control AAV hSyn.ZFP72-p2A-
1374 eGFP) were added directly into the medium of cultured hippocampal neurons on DIV5, excess
1375 particles removed via culture medium change on DIV7, and expression was allowed until
1376 DIV12.

1377 *Neuronal nuclear levels of Tau*

1378 Hippocampal mouse neurons were seeded in PLL-coated 6-well plates, AraC-treated on DIV2,
1379 transduced with AAVs as needed on DIV5. On DIV 12, cells were washed once with PBS and
1380 scraped in hypotonic buffer (250 mM sucrose, 10 mM KCl, 2 mM CaCl2, 1.5 mM MgCl2, 20 mM
1381 HEPES pH 7.4, supplemented with protease and phosphatase inhibitors). Cells were lyzed by
1382 passing the cell suspension 10-20 times through a 25-26-gauge needle. The cytosolic fraction

1383 was obtained as supernatant from centrifugation for 5 min at 1,000 g. For the nuclear fraction,
1384 the pellet was washed 1-2 times in hypotonic buffer and centrifugation for 10 min at 1,000 g.
1385 The final nuclei pellet was resuspended in RIPA supplemented with 1.25 mM MgCl2 and
1386 protease and phosphatase inhibitor, and then treated with nuclease (1 units/25 µl) for 10 min
1387 at 4 °C and collected as the supernatant of a final centrifugation for 10 min at 10,000 g. Protein
1388 samples were mixed with 6x reducing SDS-containing loading buffer, boiled at 95°C for 5 min,
1389 and separated by SDS–PAGE (NuPAGE 4-12% Bis-Tris, Invitrogen).

1390

1391 *Streptavidin pulldown of biotinylated proteins from nuclear-enriched fractions*

1392 SH-SY5Y cells seeded in 10 cm dishes were lipotransfected (0.8% lipofectamine 2000, Life
1393 Technologies) with expression plasmids for 3xHA-TurboID-Tau, 3xHA-TurboID-Tau^{P301L},
1394 3xHA-TurboID-TDP-43ctf (10 µg DNA) or 3xHA-TurboID control (5 µg DNA) to achieve similar
1395 expression levels. After 15 h, Biotin (50 µM f.c.; Sigma) was added to the medium for 10 min,
1396 before cells were washed once with ice-cold phosphate-buffered saline (1xPBS) to stop the
1397 biotinylation reaction. Cells were immediately subjected to a cellular fractionation protocol to
1398 obtain nuclear-enriched fractions. For this, cells were scraped in ice-cold hypotonic buffer (250
1399 mM sucrose, 10 mM KCl, 2 mM $CaCl_2$, 1.5 mM $MgCl_2$, 20 mM HEPES pH 7.4; supplemented
1400 with protease and phosphatase inhibitors (ThermoFisher Scientific); 0.5 ml/10 cm dish) and
1401 kept on ice for 10 min. Cell lysis was achieved by passing the cells four-times through a 25/26-
1402 gauge needle (Omnifix). The crude nuclear fraction (nuclei and some cell debris) was obtained
1403 as a pellet from a 1'000 g spin for 5 min. The nuclear pellet was washed once in hypotonic
1404 buffer (0.5 ml/sample), passed 5x through a 25/26-gauge and subsequently centrifugated
1405 again at 1'000 g for 10 min. After removal of the supernatant, the nuclei pellet was resuspended
1406 in 50 µl Urea buffer (8 M urea, 50 mM Tris-HCl pH 7.5; supplemented with 1.25 mM $MgCl_2$ and
1407 DNAse-I (ThermoFisher Scientific), and protease and phosphatase inhibitor), mixed for 20 min
1408 on a rotating wheel, and sonicated three times with 2 s-pulses. Nuclear lysates were
1409 centrifuged at 20000 g at 4°C for 15 min and the supernatant transferred into a fresh Eppendorf
1410 tube. Total protein concentration of nuclear-enriched fractions was measured by BCA assay,
1411 and the lysates stored at -80°C until further use.

1412 For the pulldown of biotinylated proteins, streptavidin agarose beads (GE Healthcare) were
1413 used in combination with spin columns with inserted 10 µm filter (MoBiTec). Streptavidin-
1414 agarose bead slurry (20 µl) was added to each column, washed once with 300 µl PBS, and
1415 centrifuged for 1 min at 2'000 rpm. To block unspecific binding, beads were incubated with
1416 300 µl 1% BSA in PBS for 1 h at room temperature under rotation. Meanwhile, all sample
1417 protein concentrations were adjusted by dilution in urea buffer to a volume of 400 µl and 1%
1418 of input samples was withdrawn and saved for analysis by western blot. For protein pulldown,
1419 blocked beads were incubated with nuclear-enriched fractions over night at 4°C under rotation.
1420 Columns were centrifuged to separate flow-through from the pulled-down biotinylated proteins,
1421 beads were washed 3-times with 300 µl wash buffer (2 M urea buffer) and once with detergent-
1422 free PBS. Finally, beads were resuspended in PBS supplemented with protease and
1423 phosphatase inhibitor (50 µl/sample). 20% of the samples were used for immunoblotting, the
1424 remaining 80% were kept at -20°C until analysis by mass spectrometry. Five independent
1425 biological replicates (proteins extracted from five different cell cultures at 5 different days) were
1426 performed for mass spectrometry.

1427

1428 *Mass spectrometry*

1429 *In solution tryptic digest:* First, proteins in samples were denatured in 8 M urea in 50 mM TEAB,
1430 pH 8.5, then samples were reduced with 5 mM DTT at 37°C for 60 min. This was followed by
1431 alkylation with 40 mM chloroacetamide at room temperature for 30 min in the dark. Protein
1432 digestion was carried out using Lysyl endopeptidase C (Wako) in a first step at an enzyme-to-
1433 protein ratio of 1:150 (w/w) at 37°C for 4 h. The sample was diluted using 50 mM TEAB, pH
1434 8.0 to 2 M urea. The second digestion step was performed with trypsin (Serva) at an enzyme-

1435 to-protein ratio of 1:100 (w/w) at 37°C overnight. Samples were desalted with C8 material
1436 (Waters) in 300 µl pipette tips, dried under vacuum, and stored at -20°C until further use.

1437 *LC-MS analysis:* LC-MS analysis was performed using an UltiMate 3000 RSLC nano LC
1438 system coupled online to an Orbitrap Fusion mass spectrometer (Thermo Fisher Scientific)
1439 with instrument software version 3.4. Proteins were separated by an in-house packaged 50 cm
1440 analytical column (Material: Poroshell 120 EC-C18, 2.7 µm, Agilent Technologies) with
1441 120 min gradients of linearly increasing ACN concentration. Data acquisition for proteomics
1442 was performed in positive mode using a MS1(orbitrap)-MS2(ion trap) method. The following
1443 parameters were applied: MS1 resolution 120,000; scan range 375 – 1500 m/z; 400k AGC
1444 target; 50 ms max. injection time; MS2 scan rate rapid; first mass 110 m/z; 10k AGC target, 35
1445 ms max. injection time; charge state 2-4 enable for MS2; HCD energy 30%; dynamic exclusion
1446 duration: 40 s.

1447 *Data analysis:* LC-MS data were searched using MaxQuant (v.1.6.2.6a) with default
1448 parameters against the human proteome (retrieved from Uniprot, 2020, reviewed sequences
1449 only). A mass tolerance of 10 ppm was set for precursors on MS1 level, 0.5 Da for fragments
1450 on MS2 level. Methionine oxidation and N-terminal acetylation were set as variable,
1451 carbamidomethylation of cysteines was set as fixed modification. Proteins were quantified
1452 using label free quantification (LFQ) within MaxQuant. Statistical data from five replicates were
1453 processed using Perseus (v.1.6.7.0) with default parameters for imputation. For volcano plots
1454 and further analysis, a log2-fold change of 1.5 and p-value of 1 were used as threshold for
1455 significance. Pathway enrichment analysis was performed using WEB-based Gene Set
1456 Analysis Toolkit (https://www.webgestalt.org/) using over-representation (ORA) analysis as
1457 enrichment method and geneontology (GO)/cellular component as enrichment categories
1458 (default background). The Venn diagram for the representation of overlapping hits was
1459 produced using https://csbg.cnb.csic.es/BioinfoGP/venny.html. Cluster analysis was
1460 performed using only significantly enriched interactors (log2 fold change > 1.5 and a $-\log_{10}$(p-
1461 value) > 1), using the k-means clustering algorithm implemented in STRING (https://string-
1462 db.org/).

1463

1464 *SDS-PAGE and Western blots*

1465 Protein samples were mixed with 6x reducing SDS-containing loading buffer, boiled at 95°C
1466 for 5 min, and separated by SDS–PAGE (NuPAGE 4-12% Bis-Tris, Invitrogen). Following
1467 electrophoresis, proteins were transferred to a nitrocellulose membrane, then the membrane
1468 was blocked with 3% BSA in PBS containing 0.05% Tween (PBS-T) at room temperature for
1469 1 h. Membranes were incubated with primary antibodies diluted in blocking solution (PBS-T,
1470 3% BSA), overnight at 4°C, washed 3-times for 5 min in PBS-T, and then incubated with
1471 fluorescent dye conjugated secondary antibodies diluted in blocking solution for 1 h at room
1472 temperature. Membranes were imaged using a Licor imaging system (Odyssey DLx). A
1473 complete list of antibodies used in Western blots can be found in the key resource table.

1474

1475 *Co-immunoprecipitation (co-IP) from nuclear-enriched fraction*

1476 SH-SY5Y cells were lipotransfected with eGFP-Tau or eGFP (Addgene #176015) plasmids
1477 (10 µg/10 cm dish) and allowed to express the constructs for 24 h. The nuclear-enriched
1478 fraction was prepared as described above via cellular fractionation with the following changes:
1479 i) For co-IP experiments under high-salt conditions, HEPES buffer (20 mM HEPES pH 7.9, 400
1480 mM NaCl, 1 mM EDTA, and 1 mM EGTA, containing protease/ phosphatase inhibitors) was
1481 used to resuspend the final nuclear pellet, followed by sonication 3-times for 3 sec. After nuclei
1482 lysis, GFP-trap magnetic particles M-270 (#gtd-20) were used for immunoprecipitation
1483 following the manufacturer protocol. In short, 25 µl beads slurry were used per sample and
1484 beads were equilibrated once with wash buffer (10 mM Tris/Cl pH 7.5, 150 mM NaCl, 0.05 %
1485 NP40, 0.5 mM EDTA; 0.5 ml/sample). For pulldown, nuclear lysates were adjusted to 0.5 ml
1486 in dilution Buffer (10 mM Tris/Cl pH 7.5, 150 mM NaCl, 0.5 mM EDTA, containing

1487 protease/phosphatase inhibitors) and incubated for 1 h at 4°C under rotation. Flow-through
1488 was separated from magnetic beads using a magnet, and beads were washed 3 times with
1489 wash Buffer. Protein elution was achieved by resuspending the beads in 80 µl educing 2x SDS
1490 sample buffer and boiling at 95°C for 5 min. Supernatants containing proteins were loaded
1491 on SDS-PAGE gels.

1492

1493 *Co-Immunoprecipitation (co-IP) of endogenous Tau*

1494 SH-SY5Y cell suspension was centrifuged for 5 min at 1000 g and 4°C. The cell pellet was
1495 resuspended in HEPES buffer (20 mM HEPES pH 7.9, 400 mM NaCl, 1 mM EDTA, and 1 mM
1496 EGTA, 0.5% NP-40, containing 25 U/µL nuclease, MgCl2, and protease/phosphatase
1497 inhibitors), followed by homogenization using 10-15 passes through a 26G needle. The cell
1498 suspension was kept 30 min on ice and sonicated 3-times for 3 s on ice. Samples were
1499 centrifuged at 10000x g for 20 min at 4°C. The supernatants were transferred to LowBind
1500 Eppendorf tube, and total protein was quantified in a Nanodrop. Protein G magnetic
1501 Dynabeads (Life Technologies, #10003D) were washed three times with PBS and blocked for
1502 1 h at room temperature with 5% BSA in PBS at constant rotation. After blocking, beads were
1503 washed twice with PBS, and blocked beads (30 µL per antibody) incubated with 8 µg antibody
1504 in PBS containing 0.02% Tween-20 for 30 min at room temperature with constant rotation. The
1505 following antibodies were used: mouse anti-Nesprin-2 (Invitrogen, MA5-18075), mouse anti-
1506 Lamin A/C (Abcam, ab238303), mouse anti-LBR (Abcam, ab232731), and mouse IgG
1507 (Invitrogen) as a negative control. Beads were washed three times with PBS containing 0.02%
1508 Tween-20. For co-IP, lysate containing 250 µg of total protein was added to antibody-coupled
1509 beads in a final volume of 500 µl PBS and incubated overnight at 4°C at constant rotation. 5%
1510 of the lysate was retained for Western Blots (input). Next day, beads were collected using a
1511 magnetic rack, and the flow-through fraction was retained for Western Blot. Beads were
1512 washed three times with PBS. Proteins were eluted by boiling beads in 2xSDS sample buffer
1513 at 95°C for 5 min. Eluates, input (5%), and acetone-precipitated flow-through samples were
1514 analyzed by SDS-PAGE followed by immunoblotting using anti–total Tau antibody (DAKO).
1515 VeriBlot secondary antibody (1:1000) was used to minimize IgG heavy and light chain
1516 detection. Signal was detected by enhanced chemiluminescence (ECL).

1517

1518 *Immunocytochemistry (ICC) and immunohistochemistry (IHC)*

1519 Cells (SH-SY5Y, HEK-293T, or primary mouse hippocampal neurons, DIV12) were washed
1520 with PBS before fixation with 4% PFA in PBS for 15 min, followed by a wash with TBS for 10
1521 min. After fixation, cells were permeabilized using 0.5% Triton-X100 in PBS for 20 min, blocked
1522 with 3% normal goat serum (NGS) in PBS for 1 h at room temperature, and incubated with
1523 primary antibodies diluted in 3% NGS/PBS over night at 4°C, or at room temperature for 2 h.
1524 After 3x10 min washes in PBS, cells were incubated with secondary antibodies in 3%
1525 NGS/PBS for 2 h at room temperature, then washed 3-times in PBS again before nuclei were
1526 counterstained with DAPI (1:1000 in PBS) for 15 min.

1527 For IHC of human brain tissue, glass slide-mounted 3 µm-thick formalin-fixed, paraffin-
1528 embedded human hippocampus and temporal cortex sections were deparaffinized and baked
1529 in citrate buffer for antigen retrieval using Ventana Benchmark GX Staining System according
1530 to manufacturer protocol, followed by 3x10 min washes in PBS. Sections were surrounded
1531 with a hydrophobic barrier, followed by permeabilization in PBS containing 0.5% Triton-X for
1532 10 min and washing in PBS for 10 min. Sections were blocked at room temperature for 1 h in
1533 PBS containing 10% NGS and 0.2% Triton-X100 (150-200 µl/slide). Primary antibodies were
1534 diluted in blocking solution and applied to sections overnight at 4°C in a humidity chamber
1535 under gentle agitation (100-200 µl/slide, depending on tissue size). After 3x10 min washes in
1536 PBS at room temperature, sections were incubated secondary antibodies diluted in 10% NGS
1537 and 0.2% Triton-X100 (150-200 µl/slide) for 1 h at room temperature. Finally, tissue auto-
1538 fluorescence was reduced by immersing the sections in 0.1% Sudan Black B in 70% ethanol
1539 for 20 min at room temperature followed by washing in PBS. The sections were mounted with

1540 mounting medium containing DAPI (DAKO). A complete list of antibodies used for ICC/IHC
1541 can be found in the key resource table.

1542

1543 *Nuclear envelope circularity in neurons*

1544 Hippocampal mouse neurons were seeded in PLL-coated 8-well plates (ibidi), AraC-treated on
1545 DIV2, transduced with AAVs on DIV5. On DIV12, cells were fixed and immunolabeled for
1546 Lamin A/C. Nuclear circularity was analyzed by detecting nuclei in the Lamin A/C channel and
1547 analyzing their shape using standard Image J plugins.

1548

1549 *BAF analysis*

1550 Human HEK-293T cells were plated in µ-slide 8-well imaging dishes (ibidi; ibiTreat) and
1551 lipotransfected (0.8% lipofectamine 2000, Life Technologies) with plasmids expressing SNAP-
1552 BAF in combination with eGFP and eGFP-Tau variants. After 24 h, cells were treated with 0.1
1553 µM of SNAP dye650 diluted in DMEM for 30 min at 37°, immediately fixed with 4% PFA/PBS,
1554 and processed for Emerin immunostaining.

1555

1556 *Proximity ligation assays (PLAs)*

1557 PFA fixed cells (SH-SY5Y or primary mouse hippocampal neurons, DIV12) or FPPE human
1558 brain tissue were permeabilized as described above and subsequently blocked (Cells: 3%
1559 BSA in PBS/0.1% Triton-X100; Tissue: Duolink blocking solution) for 1 h at room temperature.
1560 Proximity ligation assays were performed according to manufacturer protocol
1561 (Duolink®InSituDetection Reagents Red, Sigma-Aldrich). Cells/tissue were incubated with
1562 diluted primary antibodies (Cells: in 3%BSA, 0.1% Triton in PBS, 80µl per sample; Tissue: in
1563 Duolink antibody diluent, 120 µl per sample) for 1 h at 37°C or overnight at 4°C in a humidity
1564 chamber under gentle agitation. Unbound primary antibodies were removed by washing
1565 samples 3-times in wash buffer A (0.01 M Tris, 0.15 M NaCl, 0.05%Tween) under gentle
1566 agitation. Samples were incubated with PLA probes (Duolink®Anti-Rabbit PLUS and Anti-
1567 Mouse MINUS) diluted 1:5 in antibody diluent (80-120 µl/sample) for 1 h at 37°C in a humidity
1568 chamber, then washed 2-times for 5 min in wash buffer A under gentle agitation to remove
1569 unbound PLA probes. For the ligation reaction, samples were incubated with Duolink®Ligation
1570 reagent (Ligation stock 1:5 in antibody diluent plus ligase, 1:40; 80-120 µl/sample) for 30-
1571 60min at 37°C in a humidity chamber, followed by 2x5 min washes with wash buffer A. For
1572 signal amplification, Duolink®Amplification stock was diluted 1:5 in high-purity water, and
1573 polymerase (1:80) was added before slides were incubated in 80-120 µl/sample for 120 min at
1574 37°C in a humidity chamber. Final washing was performed twice for 10 min in 1X wash buffer
1575 B (0.2 M Tris, 0.1 M NaCl) and once for 1 min 0.01 X wash buffer B. Cells in 8-well chambers
1576 were incubated with DAPI in PBS (1:1000; D9542, Sigma) for 15 min at room temperature.
1577 Human tissue was additionally counterstained after PLA reaction by incubating the sections
1578 with primary antibody diluted in 10% NGS/PBS overnight at 4 °C under gentle agitation,
1579 washing 10 min with PBS at room temperature, and incubating with secondary antibody in 10%
1580 NGS/PBS for 1 h at room temperature. To reduce tissue autofluorescence, sections were
1581 immersed in 0.1% Sudan Black B in 70% ethanol for 20 min at room temperature and washed
1582 with PBS. Brain sections were mounted with mounting medium containing DAPI (DAKO). A
1583 complete list of antibodies used for ICC/IHC and PLA can be found in the key resource table.
1584 Imaging of PLAs was performed on a scanning confocal microscope (Nikon Spinning Disk
1585 Confocal CSU-X) using a 60x oil objective.

1586

1587 *Array tomography of human brains*

1588 For high resolution imaging of human nuclei, tissue from inferior temporal gyrus, BA20/21 from
1589 40 AD and 25 control cases was collected at autopsy, fixed for 2 hours in 4%

1590 paraformaldehyde, dehydrated and embedded in LR white resin(Kay *et al*, 2013). Per case
1591 two blocks of tissues from Brodmann area 20/21 (BA20/21) were cut, stained and imaged as
1592 confocal z-stacks, and then analyzed blinded for case ID and Tau channel. Ribbons of 70 nm
1593 ultra-thin sections were cut on a Leica Ultracut and stained with Alz50 (courtesy Peter Davies)
1594 and DAPI. Images were acquired at 63x magnification on a Zeiss AxioImager and aligned with
1595 custom macros (https://github.com/Spires-Jones-Lab/Array_tomography_analysis_tool). Each
1596 stack contained 12 to 24 planes. For each case, at least three stacks from different sections
1597 with and without NFT pathology were analyzed.

1598

1599 *Recombinant proteins*

1600 All plasmids were verified by Sanger sequencing prior to protein production. Final protein
1601 concentrations were measured by BCA assays (Pierce) and the proteins were stored at
1602 −80°C.

1603 Tau: Human full-length wild-type Tau (2N4R) was expressed in *E. coli* BL21 Star (DE3)
1604 (Invitrogen) and as previously described (Barghorn *et al*, 2005). Protein expression was
1605 induced with 0.5 mM IPTG at OD600 = 0.6 for ~3 h at 37°C. Cells were harvested, resuspended
1606 in lysis buffer (20 mM MES, 1 mM EGTA, 0.2 mM $MgCl_2$, 1 mM PMSF, 5 mM DTT, protease
1607 Inhibitors (Pierce Protease Inhibitor Mini Tablets, EDTA-free) and lysed using a French press.
1608 After initial purification by adding 500 mM NaCl and boiling at 95°C for 20 min, cell debris was
1609 removed by centrifugation (50'000 g, 40 min) and the supernatant was dialyzed against low
1610 salt buffer (Buffer A: 20 mM MES, 50 mM NaCl, 1 mM $MgCl_2$, 1 mM EGTA, 2 mM DTT, 0.1 mM
1611 PMSF, pH 6.8), filtered (0.22 µm membrane filter), run through a cation exchange column
1612 (HiTrap SP HP,5 ml, GE Healthcare), and eluted with a high salt buffer (Buffer B: 20 mM MES,
1613 1000 mM NaCl, 1 mM $MgCl_2$, 1 mM EGTA, 2 mM DTT, 0.1 mM PMSF, pH 6.8). Fractions
1614 containing Tau were pooled, concentrated using spin column concentrators (Protein
1615 concentrators; 10–30 kDa MWCO, Pierce), and run through a size exclusion column (Superose
1616 6 10/300, GE Healthcare). Fractions containing purified monomeric Tau were concentrated as
1617 before and buffer exchanged to PBS, 1 mM DTT, pH 7.4.

1618

1619 LBR-npd: For His-tagged LBR-NPD, the nucleoplasmic domain of human Lamin B receptor
1620 (LBR-npd; aa 1-211) was codon-optimized, and the gene synthesized by VectorBuilder and
1621 provided to us in a pET vector for protein expression (pET.LBR-npd(1-211)-TEV-10xHis).
1622 Protein expression (E. coli BL21 Star (DE3) (Invitrogen)) was induced with 0.5 mM IPTG at
1623 OD600 = 0.6 for 2 h at 37°C. Cells were harvested (6'000 rpm, 20 min), resuspended in lysis
1624 buffer (10 mM Tris-HCL, pH 7.5, 500 mM NaCl, 35 mM Imidazole, 1 mM DTT, protease
1625 Inhibitors (Pierce Protease Inhibitor Mini Tablets, EDTA-free) and lyzed using a french press.
1626 Afterwards, 10 µl Benzonase and 5 mg Lysozyme (Sigma-Aldrich) was added and incubated
1627 for 1 h at 4°C under rotation. After centrifugation (1 h at 35'000 g at 4°C), the supernatant of
1628 the lysate was filtered through a 0.22 µm membrane filter and loaded onto a Ni-NTA column
1629 (HiTrap, 5 ml, GE Healthcare) using a low imidazole buffer (Buffer 1: 10 mM Tri-HCl, pH 7.5 -
1630 8.0, 500 mM NaCl, 35 mM Imidazole, 1 mM DTT), and eluted with a high imidazole buffer
1631 (Buffer 2: with 500 mM Imidazole). Fractions containing the protein were pooled, concentrated
1632 using spin column concentrators (Amicon Ultra 15 concentrators; 10kDa MWCO, Millipore),
1633 and buffer exchanged, using 25 mM HEPES, 500 mM NaCl, 1 mM DTT as final storage buffer.

1634

1635 HP1γ: GST-tagged HP1γ (Addgene: #24076) was expressed in *E. coli* BL21 Star (DE3)
1636 (Invitrogen). Protein expression was induced with 0.5 mM IPTG at OD600 = 0.6 for 2 h at 37°C.
1637 Cells were harvested (6'000 rpm, 20min), resuspended in lysis buffer (25 mM HEPES-KOH,
1638 pH 7.9, 0.1 mM EDTA, 12.5 mM $MgCl_2$, 20 % glycerol, 0.1 mM KCl, 0.1% NP-40 Alternative
1639 (Millipore), 1 mM DTT, protease Inhibitors (Pierce Protease Inhibitor Mini Tablets, EDTA-free)
1640 and lysed using a French press. Afterwards, 10 µl Benzonase and 5 mg Lysozyme (Sigma-
1641 Aldrich) was added and incubated for 1 h at 4°C under rotation. After centrifugation (1 h, 30'000

1642 g, at 4°C) the supernatant of the lysate was filtered through a 0.22 µm membrane filter. The
1643 purification was carried out using Glutathion-Sepharos 4B (GE Healthcare) beads, the
1644 supernatant was incubated with the beads overnight at 4°C with end-to-end rotation. After
1645 incubation the beads were washed with lysis buffer (25 mM HEPES-KOH, pH 7.9, 0.1 mM
1646 EDTA, 12.5 mM $MgCl_2$, 20% glycerol, 0.1 mM KCl, 0.1% NP-40 Alternative (Millipore), 1 mM
1647 DTT, protease Inhibitors (Pierce Protease Inhibitor Mini Tablets, EDTA-free) and the protein
1648 was eluted using 50 mM Tris, 200 mM NaCl, 20 mM reduced glutathione, 0.3 mM TCEP buffer.
1649 Fractions containing the protein were pooled, concentrated using spin column concentrators
1650 (Amicon Ultra 15 concentrators; 30 kDa MWCO, Millipore). The GST tag was cleaved using
1651 Glutathion-Sepharose 4B (GE Healthcare) beads and thrombin protease (Sigma-Aldrich). After
1652 overnight incubation with protease, the supernatant was run through a size exclusion column
1653 (Superose 6 10/300, GE Healthcare) and buffer exchanged, using PBS containing 5% glycerol,
1654 1 mM DTT as final storage buffer.

1655

1656 *Fluorescent labeling of proteins*

1657 Recombinant proteins were fluorescently labeled using amine-reactive DyLight-NHS ester
1658 dyes (Thermo Scientific; Tau: DyLight488/DyLight650; LBR-npd: DyLight650; HP1γ:
1659 DyLight550) following manufacturer instructions. The dye was dissolved in DMSO to a final
1660 concentration of 10 µg/µl, then added in 5- to 10-fold molar excess to the protein in PBS with
1661 1 mM DTT, and the labeling reaction was performed for 2 h at room temperature at 250 rpm.
1662 Excess dye was removed by dialysis (Pur-A-Lyzer Mini Dialysis tubes, Sigma-Aldrich; MWCO
1663 12–14 kDa) against PBS, pH 7.4, 1 mM DTT at 4°C. The labeling degree (amount of dye per
1664 molecule protein) was determined by measuring the final protein concentration and correlating
1665 it to the maximum absorbance of the attached dye. For calculations see manufacturer
1666 instructions.

1667

1668 *Protein condensation assays*

1669 LBR-npd: 8 µM LBR-npd (1% LBP-npd-DyLight561) were imaged alone or in the presence of
1670 5.4 µM HP1γ (containing 1% HP1γ-DyLight650), 4 µM Tau (containing 2% Tau-DyLight488),
1671 and/or 75 ng/µl λ-DNA in 20 mM HEPES, pH 7.4, 130 mM NaCl. Samples (3 µl) were pipetted
1672 onto amine-coated 35-mm dishes (Matek), equipped with ddH_2O-soaked tissue to maintain
1673 humidity, and imaged after 1-2 hours.

1674 LBR-npd condensates were imaged after 1 h on a spinning disk confocal microscope (Nikon
1675 Spinning Disk Confocal CSU-X) using a 60x oil immersion objective. DNA was visualized by
1676 adding DAPI (1:1000 diluted) to the assay mix. FRAP was assessed by bleaching individual
1677 condensates in grape-like condensates assemblies (in the absence of DNA) to 20-30% of their
1678 pre-bleach intensity, or by bleaching LBR-npd on DNA to ~10% pre-bleach intensity.

1679

1680 *Tau-related NE distortions (membrane invaginations and inclusions)*

1681 HEK293 cells plated in µ-slide 8-well imaging dishes (ibidi; ibiTreat) were transfected using
1682 lipofectamine 2000 and expression allowed for 48h. Cells were treated with DMSO or 6 µM of
1683 the reversible chemical dimerizer 1 (rCD1) for 2.5 h before washing with 1XPBS followed by
1684 fixation with 4%PFA/PBS for 15 min at room temperature, and washing with TBS 3-times for
1685 10 min. CMV-mRFP encoded in a pFUGW backbone was used as fluorophore only control
1686 (kindly provided by Craig Garner). Immunostaining was performed after permeabilization for
1687 NPM1, HP1γ, SRRM2, Lamin B1, Lamin A/C, Lamin B receptor (LBR), nuclear pore complex
1688 proteins, vimentin, GAPDH, and TUBA4A. Antibody details are listed in the Key Resources
1689 Table. Nuclei were stained with either 1:1000 siRDNA or 1:3000 DAPI dilutions for 10 minutes
1690 at room temperature. Invaginations and inclusions were counted manually, blinded for
1691 condition.

1692

Electrophoretic mobility shift assay (EMSA)

To analyze binding of recombinant LBR-npd and Tau to DNA, electrophoretic mobility shift assays (EMSAs) were performed using an EMSA Kit (Cat# E33075) following manufacturer instructions. In brief, 20 ng DNA fragments (500 bp NoLimit DNA fragments Cat#SM1641) were incubated with recombinant protein at indicated amounts in 20 µl 5x binding buffer (50 mM Tris HCl, pH 7.4, 750 mM KCl, 0.5 mM DTT, 0.5 mM EDTA) for 30 min at 30°C. Samples were supplemented with 6x EMSA gel-loading solution and separated via non-denaturing PAGE on 6% DNA retardation gels 0.5x TBE gel running buffer at 110 V for 150 min. Afterwards, DNA in the gel was stained using SYBR® Green EMSA Nucleic Acid Gel Stain and visualized using a laser-based Typhoon scanner with parameters and filter sets to visualize 488 dyes. Band intensities at the end of the lanes was interpreted as unshifted DNA, all signal above as DNA bound to protein.

RNA sequencing

Hippocampal neurons were seeded in PLL-coated 6-well plates, AraC-treated on DIV2, transduced with AAVs for Tau expression (AAV eGFP-Tau) or mouse Tau knockdown (AAV ZFP90.P2a.GFP) on DIV5. On DIV12, cells were washed once with warm PBS before they were scraped-off in Trizol (ThermoFisher). RNA isolation was carried out using a RNeasy Micro Kit (Qiagen) following the manufacturer's protocol. RNA quantity and integrity were evaluated using the High Sensitivity RNA assay on the TapeStation 4200 system (Agilent). For RNA sequencing, mRNA libraries were constructed using the TruSeq Stranded mRNA Library Prep Kit (Illumina), with 500 ng of total RNA as the input material. Library quantification was conducted with the Qubit High Sensitivity dsDNA assay, and the size distribution of library fragments was assessed using the D1000 ScreenTape assay on the TapeStation 4200 system (Agilent). Sequencing was performed in paired-end mode (75 cycles) on a NovaSeq 6000 system (Illumina) using the NovaSeq S4 v1.5 (200 Cycles) chemistry. Raw sequencing data were demultiplexed using bcl2fastq2 v2.20. RNA seq was performed on 2 biological replicates with 4 technical replicates each.

RNA Seq analysis: For RNAseq data, fastq files were aligned to GRCm38 using STAR (Dobin *et al*, 2013) with the following settings to maximize repeat mapping (--outFilterMultimapNmax 100, --winAchnorMultimapNmax 100). The TETranscripts (Jin *et al*, 2015) package was used to generate a count table using gencode.vM25.basic.annotation.gtf and the prepared repeat masker file mm10_rmsk_TE.gtf (https://labshare.cshl.edu/shares/mhammelllab/www-data/TEtranscripts/TE_GTF/). The following analysis steps were performed in R (v4.3.0) and R Studio (v1.4.1717). The count table was re-annotated using biomaRt (v.2.56.1) (Durinck *et al*, 2009). Genes with less than 10 counts in at least 5 samples were excluded from the analysis resulting in 19,214 genes kept in the analysis. Normalization of the count matrix was computed with R/DESeq2 (v1.40.2) (Love *et al*, 2014a) and a variance stabilizing transformation applied using the DESeq2 vst function at default settings. A batch between experiment days was corrected with limma (v3.56.2) for the visualizations and included as covariate in the following analysis. Differential expression analysis based on the DESeq2 package was performed adjusting p-values according to independent hypothesis weighting from the IHW package (v1.28.0) (Ignatiadis *et al*, 2016) and applying apeglm shrinkage from the apeglm package (v1.22.1) (Zhu *et al*, 2019). DEGs were defined based on a fold change threshold >2 and an adjusted p-value threshold of <0.05. A gene set enrichment analysis (GSEA) was performed with the transformed data as the input using R/fgsea (v1.26.0) (Korotkevich *et al*, 2021), whereby the Gene Ontology (GO) (Ashburner *et al*, 2000; Carbon *et al*, 2021) and the Molecular Signature Database (MSigDB) (Subramanian *et al*, 2005; Liberzon *et al*, 2015) Hallmark gene set was used.

Transposable elements (TEs): The technique used for the locus-specific TE analysis is based on the method established by Schwarz et al. (Schwarz *et al*, 2022), who modified the work process of SalmonTE (v1.9.0; "SalmonTE*: a modified version for locus-specific expression analysis of transposable elements."HackMD, 2023.

https://hackmd.io/@fgaudilliere/B1nlcJ66o) to count TE on a locus level instead of on a family level (Jeong *et al*, 2018). In brief, a library of TEs was generated from the reference genome (GRCm38) using RepeatMasker (v4.0.9; http://www.repeatmasker.org) and transformed to a fasta file format with the *alignToFasta.sh* helper script. Short repeats and N-rich repeated sequences were excluded, and a salmonTE index was subsequently created. With the indices locus-specific quantification using the *SalmonTE.py* script was performed.

The DESeq2 analysis was done as above described with the following changes. TEs with fewer than 16 counts were filtered out, resulting in a final dataset of 212,571 TEs. For DE analysis the Benjamini-Hochberg method for multiple testing correction and the normal shrinkage estimator for fold change moderation was applied(Love *et al*, 2014b).

Transcriptional Factors (TFs): Differentially expressed genes (DEGs) identified as upregulated or downregulated, were compared against a curated list of mouse (*Mus musculus*) transcription factors obtained from AnimalTFDB v4.0. This analysis yielded 17 transcription factors, which were subsequently subjected to network analysis using STRING, confirming their involvement in gene regulatory processes. Activator and repressor transcription factors were identified based on STRING functional annotations and clustering.

LADs: For the LAD association data from mid brain human neurons was used and converted to mouse(Shah *et al*, 2023). The overlap between DEGs and LADs was tested with R/GenomicRanges (v1.52.0) (Lawrence *et al*, 2013) and a hyper-geometric test was performed per chromosome followed by a Benjamini-Hochberg adjustment with R/stats (v4.3.0).

wPGSA analysis: To predict transcription factor (TF) changes upstream of altered gene expression, wPGSA (Kawakami *et al*, 2016) analysis was performed as previously reported(Sakurai *et al*, 2024). In brief, normalized count matrixes generated by R/DESeq2 were used, and count values of each perturbed sample (Tau o/e or Tau k/d) were normalized to the mean count value of control samples (Tau base) using R (v4.3.3) and R Studio (v2023.12.1+402). The count matrixes normalized to the mean control values were imputed into the wPGSA package (v1.1.0) to predict altered TF activity in the perturbed samples. Significantly altered transcription factors were defined on a t-value threshold of >4 and an adjusted p-value (FDH) threshold of $<1*10^{-5}$. We looked for TFs that are included in the DEG list using R.

qPCR

Hippocampal neurons were seeded in PLL-coated 6-well plates, AraC-treated on DIV2, transduced with AAVs for Tau expression (AAV eGFP-Tau) or mouse Tau knockdown (AAV ZFP90.P2a.GFP) on DIV5. On DIV12, the culture medium was removed, cells were gently washed once with warm PBS, and then lyzed directly on the plate by adding 65 µL of lysis buffer per well, followed by cell scraping and pipetting to ensure complete cell disruption. Total RNA was purified from cell lysates using High Pure RNA Isolation Kit (ROCHE, Cat. No. 11828665001), according to the manufacturer's instructions with minor modifications. The purified RNA was used immediately for RNA quantification in a Nanodrop and stored at −80°C until further analysis. Complementary DNA (cDNA) was synthesized from total RNA using the Transcriptor High Fidelity cDNA Synthesis Kit (Roche, Cat. No. 05081955001) according to the manufacturer's instructions, using random hexamer primers. The resulting cDNA was either used immediately for downstream applications, including quantitative PCR, or stored at −20°C until further use. Quantitative real-time PCR (qPCR) was performed using LightCycler® SYBR Green I Master (Roche, Cat. No. 04707516001) on a LightCycler® 480 Instrument (Roche). Reactions were carried out on 96-well plates. Each qPCR reaction had a final volume of 25 µL and contained 12.5 µL of 2× SYBR Green I Master, 8.5 µL nuclease-free water, 1 µL of each forward and reverse primer (10 µM), and 2 µL of cDNA template. Primers were obtained from OriGene, and primer accession numbers and sequences are provided in the Key Resources Table. The genes analyzed were *GAPDH*, *NSDHL*, *TGIF1*, and *HMGCS1*. All samples were run in technical duplicates. Thermal cycling was performed under the following conditions: an initial denaturation step at 95°C for 10 min, followed by 40 cycles of amplification

consisting of 95°C for 30 s, 60°C for 20 s, and 72°C for 30 s. Melt curve was conducted with continuous fluorescence acquisition from 95°C to 60°C following a brief denaturation step at 95°C. The run concluded with a cooling step at 37°C for 1 s. Gene expression analysis was performed in the Light Cycler 480 Software (Roche). Primer efficiency was determined by standard curve analysis and incorporated into the relative quantification calculations using the Advanced Relative Quantification method. Amplification efficiencies ranged from 1.895 to 2.429 across all primer pairs. GAPDH was used as the endogenous reference gene. Relative expression levels for each target gene were normalized to non-transduced neurons and are presented as fold change.

Cleavage under targets & tagmentation (CUT&Tag) assay

For the genome-wide analysis of H3K9ac histone mark in primary mouse neurons the CUT&Tag-IT assay kit (Active Motif) was used according to manufacturer's instructions. Hippocampal neurons were seeded in PLL-coated 6-well plates, AraC-treated on DIV2, transduced with AAVs for Tau expression (AAV eGFP-Tau) ort mouse Tau knockdown (AAV ZFP90.P2a.GFP) on DIV5. On DIV12 cells were harvested from 6-Wells by scratching in medium, pooling 3 Wells per condition. Cells were bound to Concavalin A beads, followed by incubation with 1.5 µg primary antibody (H3K9ac) o/n at 4°C using an orbital mixer. Following, Guinea Pig Anti-Rabbit secondary antibody was added to bind to primary bound antibody. The following steps included i) binding of CUT&Tag-IT™Assembled pA-Tn5 Transposomes (protein A fused to Tn5 transposase enzyme that is pre-loaded with sequencing adapters and binds to secondary antibody), ii) Tagmentation (fragmentation and tagging with sequencing adaptors) and iii) DNA extraction according to the protocol. PCR amplification was performed using unique combinations of one i7 Indexed Primer and one i5 Indexed Primer per condition. The final step to obtain libraries for sequencing contained a clean-up using magnetic SPRI beads. After library generation, the quality was assessed using Agilent TapeStation, yielding mostly fragments below 500 bp. Libraries were sequenced in a paired end configuration using NextSeq2000, 10-15 million reads per sample at the BIH/MDC Genomics Technology Platform, Berlin.

Analysis: Demultiplexed reads were aligned to GRCm39 using bowtie2 (Langmead & Salzberg, 2012) with the parameters --end-to-end --very-sensitive --no-mixed --no-discordant –phred33 -I 10 -X 700, and sorted and indexed using samtools. Duplicate reads were removed using picard. Read fragments from aligned reads were prepared using bedtools bamtobed to extract read pairs on the same chromosome with fragments smaller than 1000bp. Fragment bed files were converted to bedgraphs suitable for SEACR (Meers *et al*, 2019) using bedtools genomecov -bg. SEACR was run on each prepared bedgraph file with 0.005 (top 0.05%) norm stringent as parameters. Peaks identified in each sample were merged into a single master peak file. A count matrix of counts from each sample over all peaks was generated using the getCounts from the chromVAR package (Schep *et al*, 2017). Differential peaks were tested using DESeq2 and annotated with genes and genomic region using annotatePeak with tss region (-3000, 3000) from the ChIPseeker library. Overlaps with Repeat elements and T1 and T2 LAD elements were detected using findOverlaps.

Chromosome painting

Hippocampal neurons were seeded in PLL-coated 12-well plates equipped with glass coverslips, AraC-treated on DIV2, and transduced with AAVs on DIV5. None-transduced neurons were included as controls (Tau base). On DIV12, neurons were fixed in 4% paraformaldehyde (PFA) for 10 min at room temperature, washed for 3 min in 0.1 M Tris-HCl (pH 7.4), and subsequently rinsed twice for 5 min in PBS. Cells were permeabilized with 0.5% Triton X-100 in PBS for 15 min at room temperature, followed by equilibration in 20% glycerol in PBS for 1.5 h at room temperature. Coverslips with cells were subjected to five freeze–thaw cycles: each cycle consisted of the immersion in liquid nitrogen for 30 s, thawing on tissue until the frozen layer disappeared, and incubation in 20% glycerol/PBS for 3 min. Coverslips were

then washed three times for 10 min in PBS. For DNA depurination and probe accessibility, cells were incubated in freshly made 0.1 N HCl for 5 min at room temperature, washed three times for 3 min in 2X saline-sodium citrate (SSC) buffer, and three times for 5 min in PBS. Coverslips were prehybridized in freshly made 50% v/v formamide (pH 7.0) in 2X SSC for 1 h on ice. Chromosome painting probes (Metasystem, see key resource table for each probe information) were applied to a cleaned glass slide (2–2.5 µl per ¼ coverslip), and coverslips were placed cell-side down on the probe and sealed with nail polish. Samples and probes were denatured simultaneously on a hotplate at 75°C (±1°C) for 2 min and hybridized overnight for at least 16 h in a humidified chamber at 37°C (±1°C). Post-hybridization washes were performed by carefully removing the nail polish and detaching the coverslips from the slide, followed by washing the coverslips in 0.4X SSC at 72°C (±1°C) for 2 min. Coverslips were then rinsed in 2X SSC with 0.05% Tween-20 at RT for 30 s, briefly rinsed in distilled water, and air-dried. Cells were counterstained with DAPI/antifade mounting medium (MetaSystems, D-0902-500-DA) by applying a 2 - 3 µl drop into a clean glass slide and placing the coverslips cell-side down on DAPI, allowing to incubate for 10 min at room temperature, and sealed with nail polish. Slides were stored at 4°C protected from light until imaging. Confocal images were acquired as serial z-stacks with a step size of 0.3 µm using a 60x objective at 3x digital zoom.

Fluorescence microscopy

Fluorescent images were acquired with a Nikon scanning Confocal A1Rsi+ microscope with a DS-Q12 Nikon camera at the Advanced Medical BIOimaging (Ambio) Core Facility at the Charité, Berlin. To prevent crosstalk among the fluorophores, channels were scanned sequentially, starting from the highest excitation wavelength to the lowest. Fluorescence lifetime imaging microscopy (FLIM) of SiR-DNA in primary mouse neurons and NesprinTS in HEK293 cells was performed using a Leica Stellaris 8-Falcon-STED confocal microscope at the Systems Biology Imaging core at BIMSB/MDC, Berlin. FRAP for LBR and LEM2 condensates, as well as co-transfections with SUN1 or LBR and Tau in HEK-293 cells, were performed on a Nikon Spinning Disk Confocal CSU-W1 SoRa microscope, as well as in a Zeiss Axio Observer Laser Scanning Confocal Microscope at DZNE, Berlin. Epifluorescence images of immunolabeled human brain slices, primary hippocampal neurons for nuclear circularity and HEK cells for BAF analysis, were collected on a Keyence BZ-X system. All images were processed with ImageJ or CellProfiler.

Image modality / Microscope	**Point scanning confocal / Nikon A1Rsi+ microscope**
Illumination /Wavelength Selection	Excitation: DAPI = 405 nm; GFP = 488 nm; mCherry = 561 nm; Cy5 = 647 nm
	Emission filters/Bandwidth: DAPI = 450/50; GFP = 525/50; mCherry = 595/50; Cy5 = 700/75
Optics	Magnification: 20x; Type: Plan Apo; Immersion: Air; NA: 0.8; WD (µm) 1,000
	Magnification: 40x; Type: Plan Fluor; Immersion: Oil; NA: 1.3; WD (µm) 200
	Magnification: 60x; Type: Plan Apo; Immersion: Oil; NA: 1.4; WD (µm) 130
Image modality / Microscope	**Inverted fluorescence-phase contast microscope / Keyence BZ-X800**
Illumination /Wavelength Selection	Excitation: DAPI = 360/40 nm; GFP = 470/40 nm; TRITC = 545/25 nm; Cy5 = 620/60 nm

	Emission filters/Bandwidth: DAPI = 460/50; GFP = 525/50; TRITC = 605/70; Cy5 = 700/75
Optics	Magnification: 60x; Type: Plan Apo; Immersion: Oil; NA: 1.40; WD (µm): 130
Image modality / Microscope	**Nikon SoRa Spinning Disk Confocal CSU-W1**
Illumination /Wavelength Selection	Excitation: DAPI = 405 nm; CFP = 455 nm; GFP = 488 nm; mCherry = 561 nm; Cy5 = 647 nm
	Emission filters/Bandwidth: DAPI = 447/60; CFP = 472/30; GFP = 525/50; mCherry = 600/50; Cy5 = 685/40
Optics	Magnification: 60x; Type: Plan Apo; Immersion: Oil; NA: 1.4; WD (µm) 130
Image modality / Microscope	**Carl Zeiss Axio Observer Z1 Laser Scanning Confocal with iXon ultra (Andor) camera**
Illumination /Wavelength Selection	Excitation: CFP = 455 nm; RFP = 561 nm; Cy5 = 647 nm
	Emission filters/Bandwidth: CFP = 480; RFP = 584; Cy5 = 670 nm
Optics	Magnification: 63x; Type: Plan Apo; Immersion: Oil; NA: 1.40; WD (µm): 512
Image modality / Microscope	**Confocal Leica SP8 Stellaris**
Illumination /Wavelength Selection	Excitation: CFP = 450 nm; GFP = 480 nm; YFP/Venus = 510 nm; iRFP/SirDNA = 645 nm
Optics	Emission filters/Bandwidth: CFP/TFP1 = 500/50; GFP = 525/50; YFP/Venus = 555/50; iRFP/SirDNA = 700/75
Sample Preparation	
	8-well imaging dishes (ibiTreat; Polymer coverslip No. 1.5H)
	8-well glass bottom imaging dishes (Glass coverslip No. 1.5H)
	35 mm dishes (Glass coverslip No. 1.5H)

Image analysis

Heterochromatin markers: An image analysis pipeline was created in CellProfiler to analyze heterochromatin intensity and chromocenter number and size. The pipeline for nuclear intensity consisted of: IdentifyPrimaryObjects (in DAPI channel) > MeasureObjectIntensity (in DAPI and HC channel) > MeasureObjectSizeShape. The pipeline for chromocenter analysis consisted of: IdentifyPrimaryObjects (in DAPI channel) > EnhanceOrSuppressFeatures (Enhance: HC in heterochromatin channel) > MasImage > IdentifyPrimaryObjects > MeasureObjectSizeShape > MeasureObjectIntensityDistribution (Bin =4). > RelateObjects

Line plots: Define horizontal line of same length as ROI; ImageJ > Analyze > Plot profile.

Clock scan: For the chromatin and the chromosome territories analysis, the *Clock scan* plugin of ImageJ was used. This plugin (i) measures the fluorescence intensity profile along a line (radial line) from the center to the outer boundary of an ROI, and (ii) creates an average of all 360 intensity profiles measured upon 360° rotation of the radial line. The output is a graph presenting average fluorescence intensity (y-axis) over the distance to the center in % of radius (x-axis; 100% = nuclear border). For the analysis of the average radial distribution of chromatin, neuronal nuclei were analyzed in SiR-DNA images collected from living neurons. For the

analysis of the averaged radial distribution of chromosome territories, chromosome signals were quantified in the equatorial plane of the z-stacks acquired from neuronal nuclei of fixed neurons. Clock scans of nuclei with fluorescence signal accumulation at the NE produced a graph with a peak of ~90-100% radius.

Nuclear invaginations in human brain: Z-stacks of DAPI-stained nuclei in AD brain were obtained. Nuclei were identified as "invaginated" when at least one membrane fold (=invagination) was spotted across the z-stack. The presence of misfolded Tau (Alz50+) around nuclei was determined afterwards by merging DAPI and ALZ50 channels.

TurboID constructs: In representative confocal images (60x) of TurboID constructs expressed in SH-SY5Y cells, nuclei were outlined using the DAPI channel and added as white outlines using *Flatten* in ROI Manager.

PLAs: To quantify PLA signals, nuclei ROIs were defined by thresholding images in the DAPI channel (ImageJ) and defining them as individual particles. Afterwards, PLA signal spots within nuclear ROIs were detected in the PLA channel (Cy3) using the *Find maxima* function. The number of PLA signal spots were normalized to the number of cell nuclei. 2-3 experiments were performed for each condition, and 3-6 images analyzed per condition.

Protein condensates: Surface coverage was determined on an image-by-image base by measuring the area covered by condensates after thresholding the image to remove surface background in ImageJ. Co-partitioning coefficients (= $c_{dense\ phase}/c_{light\ phase}$) were determined on an image-by-image base by dividing the mean fluorescence intensities measured inside condensates by the one measured outside of condensates. Coefficient variance of DNA inside condensates was determined on a condensate-by-condensate base by dividing the standard deviation by the mean of individual condensates (CoeffVar = SD/mean). Line Plots: Lines of same length were drawn across condensates in the LEM2 channel using ImageJ, and the intensity profiles for all channels along the same line measured by the plot profile function. The y-values for each channel were normalized to min=0 and max=1 and plotted in GraphPad Prism 10.

Nuclear circularity: An image analysis pipeline was created in CellProfiler to analyze the circularity and eccentricity of the nuclei using LaminA/C staining from the different transduced groups. Individual nuclei were cropped using the DAPI channel > IdentifyPrimaryObjects (in Lamin A/C channel) > MeasureObjectSizeShape.

BAF area: For each image, HEK293 cells expressing Tau constructs were identified based on GFP fluorescence. The SNAP-BAF channel was then analyzed to quantify the total BAF positive area per cell. In parallel, the number of discrete BAF foci (dots) per cell was manually counted. For each cell, the BAF area was normalized to the number of BAF foci, and the resulting values were used for statistical analysis and plotting.

Statistical analysis

For the Statistical analysis GraphPad Prism versions 9 and 10 (GraphPad Software, San Diego, CA, USA; www.graphpad.com) were used. For comparison of two groups, unpaired two-tailed Student's t-tests were used. For comparison of multiple groups, one-way ANOVAs with Tukey post-test (comparison between all means) or Dunnett post-test (comparison to mean of control) were applied. Significance is indicated as *$p<0.05$, **$p<0.01$, ***$p<0.001$, ****$p<0.0001$.

Data Availability

Mass spectrometry: Proteomics data have been deposited to the ProteomeXchange Consortium via the PRIDE partner repository with the dataset identifier PXD058565 (Reviewer access details: Username: reviewer_pxd058565@ebi.ac.uk; Password**:** yPkItu6tXRW5).

Sequencing data: The bulkRNAseq and Cut&Tag data are available under the following GEO accession number: GSE283514.

Contributions

L.D. and S.W. conceived the project, conceptualized the study, curated data, designed figures, and wrote the manuscript.
L.D. and R.P-L. designed and performed experiments and interpreted data.
S.W. conducted FLIM and LLPS experiments and analysis.
C.K. and C.B. helped with PLA experiments.
B.A. developed AAV and TurboID vectors and deigned cloning of cell constructs
T.K. developed experimental protocols and tools for TurboID experiments.
C.W. performed Mass Spectrometry.
K.S. and P.G. performed RNA-Seq data analysis.
K.T. analyzed human array tomography images.
R.A., A.D.-B., M. M., S.H., S.M., B.K.N-H., R.S., M.F. assisted with experiments.
H.R. supplied human brain tissue for PLA and IHC analysis.
T.S.-J. supplied array tomography images from human brain tissue.
E.DeD. and M.B. performed RNA-Seq.
A.N. analyzed CUT&Tag data and consulted in RNA-Seq and CUT&Tag experiments.
T.U. discussed data and reviewed manuscript.
F.L. discussed MS data.
A.v.A. discussed data, reviewed manuscript.
T.T. discussed data and reviewed manuscript.
All authors reviewed and approved the manuscript.

Acknowledgements

We thank Britta Eickholt, Charité Berlin, for enabling the use of Charité department equipment and general support, Carmelo Ferrai, University Göttingen, for data discussions and advise on chromatin imaging, Gabriele Kaminski Schierle, University Cambridge, for advice on SiR-DNA FLIM, Francsico Garciá-Sierra, Cinvestav Mexico City, for sharing protocols for immunofluorescence in human brain tissue, Donato Di Monte and his team, DZNE Bonn, for sharing protocols for PLA in brain tissue, and Eda Yildrim, Koc University, for chromosome PAINT advise. We thank Thorsten Trimbuch and the Charité viral core facility for AAV vectors production, Bettina Brokowski from Charité viral core facility for help with qPCR experiments, the Jan Schmoranzer and the Charité Bioimaging core (AMBIO) for support in confocal microscopy, Robert Zinzen, MDC BIMSB, for support in FLIM imaging, the single cell sequencing core PRECISE in Bonn, for RNA sequencing and data analysis, the Core Facility Genomics, Berlin Institute of Health at Charité (BIH), for Cut&Tag sequencing, and Max Ruwolt for help with the MS data upload. The authors are most grateful to the individuals and their relatives for consenting to autopsy and subsequent research, which were facilitated by the Biobank of the Department of Neuropathology, Charité-Universitätsmedizin Berlin.

Funding

Funding for this study was granted to S.W. by the BrightFocus Foundation (A2021044S), the Verum Foundation, the Rainwater Foundation, the German Research Foundation (DFG, SPP2191, 506373047), the European Union (ERC 101126140) and the Helmholtz Association. B.A. and L.R. were supported by the Einstein Foundation. T.S.-J. received funding for this collaboration from the UK Dementia Research Institute (award number UK DRI-4004) through UK DRI Ltd, principally funded by the UK Medical Research Council. T.T. and K.S. received funding by the European Union (ERC, 804468) and DFG (SPP2202, TO 1347/5-1). F.L. and C.W. received funding by the European Union (ERC 949184).

2003 **Declaration of interests**

2004 F.L. is a shareholder and advisory board member of Absea Biotechnology Ltd and VantAI.

2005

2006 **References**

2007 Abasi LS, Elathram N, Movva M, Deep A, Corbett KD & Debelouchina GT (2024)
2008 Phosphorylation regulates tau's phase separation behavior and interactions with
2009 chromatin. *Communications Biology 2024 7:1* 7: 1–17

2010 Aguado F, Díaz-Ruiz C, Parlato R, Martínez A, Carmona MA, Bleckmann S, Ureña JM,
2011 Burgaya F, Del Río JA, Schütz G, *et al* (2009) The CREB/CREM Transcription Factors
2012 Negatively Regulate Early Synaptogenesis and Spontaneous Network Activity. *The*
2013 *Journal of Neuroscience* 29: 328

2014 Alexander C, Li T, Hattori Y, Chiu D, Frost GR, Jonas L, Liu C, Anderson CJ, Wong E, Park
2015 L, *et al* (2022) Hypoxia Inducible Factor-1α binds and activates γ-secretase for Aβ
2016 production under hypoxia and cerebral hypoperfusion. *Mol Psychiatry* 27: 4264

2017 An H, Williams NG & Shelkovnikova TA (2018) NEAT1 and paraspeckles in
2018 neurodegenerative diseases: A missing lnc found? *Noncoding RNA Res* 3: 243–252

2019 Aron L, Qiu C, Ngian ZK, Liang M, Drake D, Choi J, Fernandez MA, Roche P, Bunting EL,
2020 Lacey EK, *et al* (2023) A neurodegeneration checkpoint mediated by REST protects
2021 against the onset of Alzheimer's disease. *Nat Commun* 14

2022 Ashburner M, Ball CA, Blake JA, Botstein D, Butler H, Cherry JM, Davis AP, Dolinski K,
2023 Dwight SS, Eppig JT, *et al* (2000) Gene Ontology: tool for the unification of biology.
2024 *Nature Genetics 2000 25:1* 25: 25–29

2025 Askin B, Gomez CC, Duong SL-L, Kilic C, Goihl A, Newman A, Wagner J, Thomas V,
2026 Lamberty J, Huebschmann S, *et al* (2024) Autoimmune antibody-induced neuronal
2027 hyperactivity triggers pathological Tau in IgLON5 disease. *bioRxiv*: 2024.03.10.584272

2028 Balusu S, Praschberger R, Lauwers E, De Strooper B & Verstreken P (2023)
2029 Neurodegeneration cell per cell. *Neuron* 111: 767–786

2030 Barry G, Briggs JA, Hwang DW, Nayler SP, Fortuna PRJ, Jonkhout N, Dachet F, Maag JLV,
2031 Mestdagh P, Singh EM, *et al* (2017) The long non-coding RNA NEAT1 is responsive to
2032 neuronal activity and is associated with hyperexcitability states. *Sci Rep* 7

2033 Bengtsson L & Otto H (2008) LUMA interacts with emerin and influences its distribution at
2034 the inner nuclear membrane. *J Cell Sci* 121: 536–548

2035 Benhelli-Mokrani H, Mansuroglu Z, Chauderlier A, Albaud B, Gentien D, Sommer S,
2036 Schirmer C, Laqueuvre L, Josse T, Buée L, *et al* (2018) Genome-wide identification of
2037 genic and intergenic neuronal DNA regions bound by Tau protein under physiological
2038 and stress conditions. *Nucleic Acids Res* 46: 11405–11422

2039 Von Bergen M, Friedhoff P, Biernat J, Heberle J, Mandelkow EM & Mandelkow E (2000)
2040 Assembly of τ protein into Alzheimer paired helical filaments depends on a local
2041 sequence motif (306VQIVYK311) forming β structure. *Proc Natl Acad Sci U S A* 97:
2042 5129–5134

2043 Berghoff SA, Spieth L, Sun T, Hosang L, Depp C, Sasmita AO, Vasileva MH, Scholz P, Zhao
2044 Y, Krueger-Burg D, *et al* (2021) Neuronal cholesterol synthesis is essential for repair of
2045 chronically demyelinated lesions in mice. *Cell Rep* 37: 109889

2046 Bikkul MU, Faragher RGA, Worthington G, Meinke P, Kerr ARW, Sammy A, Riyahi K, Horton
2047 D, Schirmer EC, Hubank M, *et al* (2019) Telomere elongation through hTERT
2048 immortalization leads to chromosome repositioning in control cells and genomic

2049 instability in Hutchinson-Gilford progeria syndrome fibroblasts, expressing a novel SUN1
2050 isoform. *Genes Chromosomes Cancer* 58: 341

2051 Bolognesi B, Gotor NL, Dhar R, Cirillo D, Baldrighi M, Tartaglia GG & Lehner B (2016) A
2052 Concentration-Dependent Liquid Phase Separation Can Cause Toxicity upon Increased
2053 Protein Expression. *Cell Rep* 16: 222–231

2054 Borden J & Manuelidis L (1988) Movement of the X chromosome in epilepsy. *Science (1979)*
2055 242: 1686–1691

2056 Branon TC, Bosch JA, Sanchez AD, Udeshi ND, Svinkina T, Carr SA, Feldman JL, Perrimon
2057 N & Ting AY (2018) Efficient proximity labeling in living cells and organisms with
2058 TurboID. *Nat Biotechnol* 36: 880–898

2059 Braun NJ, Yao KR, Alford PW & Liao D (2020) Mechanical injuries of neurons induce tau
2060 mislocalization to dendritic spines and tau-dependent synaptic dysfunction. *Proc Natl*
2061 *Acad Sci U S A* 117: 29069–29079

2062 Canchi S, Raao B, Masliah D, Rosenthal SB, Sasik R, Fisch KM, De Jager PL, Bennett DA &
2063 Rissman RA (2019) Integrating Gene and Protein Expression Reveals Perturbed
2064 Functional Networks in Alzheimer's Disease. *Cell Rep* 28: 1103

2065 Carbon S, Douglass E, Good BM, Unni DR, Harris NL, Mungall CJ, Basu S, Chisholm RL,
2066 Dodson RJ, Hartline E, *et al* (2021) The Gene Ontology resource: enriching a GOld
2067 mine. *Nucleic Acids Res* 49: D325–D334

2068 Carley E, Stewart RK, Zieman A, Jalilian I, King DE, Zubek A, Lin S, Horsley V & King MC
2069 (2021) The linc complex transmits integrin-dependent tension to the nuclear lamina and
2070 represses epidermal differentiation. *Elife* 10

2071 Chai WN, Wu YF, Wu ZM, Xie YF, Shi QH, Dan W, Zhan Y, Zhong JJ, Tang W, Sun XC, *et*
2072 *al* (2022) Neat1 decreases neuronal apoptosis after oxygen and glucose deprivation.
2073 *Neural Regen Res* 17: 163–169

2074 Chang CW, Shao E & Mucke L (2021) Tau: Enabler of diverse brain disorders and target of
2075 rapidly evolving therapeutic strategies. *Science (1979)* 371: eabb8255

2076 Chantranupong L, Wolfson RL & Sabatini DM (2015) Nutrient Sensing Mechanisms Across
2077 Evolution. *Cell* 161: 67

2078 Chatoo W, Abdouh M, David J, Champagne MP, Ferreira J, Rodier F & Bernier G (2009) The
2079 Polycomb Group Gene Bmi1 Regulates Antioxidant Defenses in Neurons by Repressing
2080 p53 Pro-Oxidant Activity. *Journal of Neuroscience* 29: 529–542

2081 Chen CK, Blanco M, Jackson C, Aznauryan E, Ollikainen N, Surka C, Chow A, Cerase A,
2082 McDonel P & Guttman M (2016) Xist recruits the X chromosome to the nuclear lamina
2083 to enable chromosome-wide silencing. *Science (1979)* 354: 468–472

2084 Chen Z, Hou C, Wang L, Yu C, Chen T, Shen B, Hou Y, Li P & Li T (2022) Screening
2085 membraneless organelle participants with machine-learning models that integrate
2086 multimodal features. *Proc Natl Acad Sci U S A* 119: e2115369119

2087 Cheng Y, Yin Y, Zhang A, Bernstein AM, Kawaguchi R, Gao K, Potter K, Gilbert HY, Ao Y,
2088 Ou J, *et al* (2022) Transcription factor network analysis identifies REST/NRSF as an
2089 intrinsic regulator of CNS regeneration in mice. *Nature Communications 2022 13:1* 13:
2090 1–22

2091 Chou CC, Zhang YYJ, Umoh ME, Vaughan SW, Lorenzini I, Liu F, Sayegh M, Donlin-Asp
2092 PG, Chen YH, Duong DM, *et al* (2018) TDP-43 pathology disrupts nuclear pore
2093 complexes and nucleocytoplasmic transport in ALS/FTD. *Nat Neurosci* 21: 228–239

2094 Chuang DM, Leng Y, Marinova Z, Kim HJ & Chiu CT (2009) Multiple roles of HDAC inhibition
2095 in neurodegenerative conditions. *Trends Neurosci* 32: 591–601

2096 Cichocki F, Wu CY, Zhang B, Felices M, Tesi B, Tuininga K, Dougherty P, Taras E, Hinderlie
2097 P, Blazar BR, *et al* (2018) ARID5B regulates metabolic programming in human adaptive
2098 NK cells. *J Exp Med* 215: 2379

2099 Cornelison GL, Levy SA, Jenson T & Frost B (2019) Tau-induced nuclear envelope
2100 invagination causes a toxic accumulation of mRNA in Drosophila. *Aging Cell* 18

2101 Cremer T & Cremer C (2001) Chromosome territories, nuclear architecture and gene
2102 regulation in mammalian cells. *Nature Reviews Genetics 2001 2:4* 2: 292–301

2103 Decourt B, Lahiri DK & Sabbagh MN (2017) Targeting Tumor Necrosis Factor Alpha for
2104 Alzheimer's Disease. *Curr Alzheimer Res* 14: 412–425

2105 Depp C, Sun T, Sasmita AO, Spieth L, Berghoff SA, Nazarenko T, Overhoff K, Steixner-
2106 Kumar AA, Subramanian S, Arinrad S, *et al* (2023) Myelin dysfunction drives amyloid-β
2107 deposition in models of Alzheimer's disease. *Nature* 618: 349–357

2108 Diez L, Kapinos LE, Hochmair J, Huebschmann S, Dominguez-Baquero A, Vogt A, Rankovic
2109 M, Zweckstetter M, Lim RYH & Wegmann S (2022) Phosphorylation but Not
2110 Oligomerization Drives the Accumulation of Tau with Nucleoporin Nup98. *Int J Mol Sci*
2111 23: 3495

2112 Dobin A, Davis CA, Schlesinger F, Drenkow J, Zaleski C, Jha S, Batut P, Chaisson M &
2113 Gingeras TR (2013) STAR: ultrafast universal RNA-seq aligner. *Bioinformatics* 29: 15–
2114 21

2115 Durinck S, Spellman PT, Birney E & Huber W (2009) Mapping identifiers for the integration of
2116 genomic datasets with the R/Bioconductor package biomaRt. *Nat Protoc* 4: 1184–1191

2117 Eftekharzadeh B, Daigle JG, Kapinos LE, Coyne A, Schiantarelli J, Carlomagno Y, Cook C,
2118 Miller SJ, Dujardin S, Amaral AS, *et al* (2018) Tau Protein Disrupts Nucleocytoplasmic
2119 Transport in Alzheimer's Disease. *Neuron*

2120 Essepian N, Yuan S, Roberts R, Sherman E, Gniadzik W, Wang Q, Erisir A & Jiang L (2025)
2121 Tau Oligomerization Drives Neurodegeneration via Nuclear Membrane Invagination and
2122 Lamin B Receptor Binding in Alzheimer's disease. *bioRxiv*: 2025.05.21.655370

2123 Fernández-Nogales M & Lucas JJ (2020) Altered Levels and Isoforms of Tau and Nuclear
2124 Membrane Invaginations in Huntington's Disease. *Front Cell Neurosci* 13: 1–12

2125 Frost B (2016) Alzheimer's disease: An acquired neurodegenerative laminopathy. *Nucleus* 7:
2126 275–283 doi:10.1080/19491034.2016.1183859 [PREPRINT]

2127 Frost B, Bardai FH & Feany MB (2016) Lamin Dysfunction Mediates Neurodegeneration in
2128 Tauopathies. 26: 129–136

2129 Frost B, Hemberg M, Lewis J & Feany MB (2014) Tau promotes neurodegeneration through
2130 global chromatin relaxation. *Nature Neuroscience 2014 17:3* 17: 357–366

2131 Gates LA, Shi J, Rohira AD, Feng Q, Zhu B, Bedford MT, Sagum CA, Jung SY, Qin J, Tsai
2132 MJ, *et al* (2017) Acetylation on histone H3 lysine 9 mediates a switch from transcription
2133 initiation to elongation. *J Biol Chem* 292: 14456

2134 Goelzer M, Howard S, Zavala AG, Conway D, Rubin J & Uzer G (2025) Depletion of SUN1/2
2135 induces heterochromatin accrual in mesenchymal stem cells during adipogenesis.
2136 *Communications Biology 2025 8:1* 8: 1–14

2137 Gottschall PE & Howell MD (2015) ADAMTS expression and function in central nervous
2138 system injury and disorders. *Matrix Biol* 44–46: 70

2139 Guo C, Jeong HH, Hsieh YC, Klein HU, Bennett DA, De Jager PL, Liu Z & Shulman JM
2140 (2018) Tau Activates Transposable Elements in Alzheimer's Disease. *Cell Rep* 23:
2141 2874–2880

Guo S, Zhu W, Bian Y, Li Z, Zheng H, Li W, Yang Y, Ji X & Zhang B (2024) Developing diagnostic biomarkers for Alzheimer's disease based on histone lactylation-related gene. *Heliyon* 10: e37807

Halfmann CT, Sears RM, Katiyar A, Busselman BW, Aman LK, Zhang Q, O'Bryan CS, Angelini TE, Lele TP & Roux KJ (2019) Repair of nuclear ruptures requires barrier-to-autointegration factor. *Journal of Cell Biology* 218: 2136–2149

Hochmair J, Exner C, Franck M, Dominguez-Baquero A, Diez L, Brognaro H, Kraushar ML, Mielke T, Radbruch H, Kaniyappan S, *et al* (2022) Molecular crowding and RNA synergize to promote phase separation, microtubule interaction, and seeding of Tau condensates. *EMBO J* 41

Hochmair J, van den Oetelaar MCM, Ravatt L, Diez L, Lemmens LJM, Ponce-Lina R, Sankar R, Franck M, Nolte G, Semenova E, *et al* (2025) Stoichiometric 14-3-3ζ binding promotes phospho-Tau microtubule dissociation and reduces aggregation and condensation. *Communications Biology 2025 8:1* 8: 1–17

Hockings C, Poudel C, Feeney KA, Novo CL, Hamouda MS, Mela I, Fernandez-Antoran D, Vallejo-Ramirez PP, Rugg-Gunn PJ, Chalut K, *et al* (2020) Illuminating chromatin compaction in live cells and fixed tissues using SiR-DNA fluorescence lifetime. *bioRxiv*: 2020.05.02.073536

Hu Z, Raucci S, Jaquenoud M, Hatakeyama R, Stumpe M, Rohr R, Reggiori F, De Virgilio C & Dengjel J (2019) Multilayered Control of Protein Turnover by TORC1 and Atg1. *Cell Rep* 28: 3486-3496.e6

Hua Q, He RQ, Haque N, Qu MH, Del Carmen Alonso A, Grundke-Iqbal I & Iqbal K (2003) Microtubule associated protein tau binds to double-stranded but not single-stranded DNA. *Cell Mol Life Sci* 60: 413–421

Hwang JY & Zukin RS (2018) REST, a master transcriptional regulator in neurodegenerative disease. *Curr Opin Neurobiol* 48: 193

Hyun Kim D, Perdomo G, Zhang T, Slusher S, Lee S, Phillips BE, Fan Y, Giannoukakis N, Gramignoli R, Strom S, *et al* (2011) FoxO6 Integrates Insulin Signaling With Gluconeogenesis in the Liver. *Diabetes*: 2763–2774

Igaz LM, Kwong LK, Xu Y, Truax AC, Uryu K, Neumann M, Clark CM, Elman LB, Miller BL, Grossman M, *et al* (2008) Enrichment of C-terminal fragments in TAR DNA-binding protein-43 cytoplasmic inclusions in brain but not in spinal cord of frontotemporal lobar degeneration and amyotrophic lateral sclerosis. *Am J Pathol* 173: 182–194

Ignatiadis N, Klaus B, Zaugg JB & Huber W (2016) Data-driven hypothesis weighting increases detection power in genome-scale multiple testing. *Nat Methods* 13: 577–580

Jeganathan S, Von Bergen M, Mandelkow EM & Mandelkow E (2008) The natively unfolded character of Tau and its aggregation to Alzheimer-like paired helical filaments. *Biochemistry* 47: 10526–10539

Jeong HH, Yalamanchili HK, Guo C, Shulman JM & Liu Z (2018) An ultra-fast and scalable quantification pipeline for transposable elements from next generation sequencing data. *Pacific Symposium on Biocomputing* 0: 168–179

Jiang L, Lin W, Zhang C, Ash PEA, Verma M, Kwan J, van Vliet E, Yang Z, Cruz AL, Boudeau S, *et al* (2021) Interaction of tau with HNRNPA2B1 and N6-methyladenosine RNA mediates the progression of tauopathy. *Mol Cell* 81: 4209-4227.e12

Jiang L & Wolozin B (2021) Oligomeric tau disrupts nuclear envelope via binding to lamin proteins and lamin B receptor. *Alzheimer's & Dementia* 17: e054521

Jin Y, Tam OH, Paniagua E & Hammell M (2015) TEtranscripts: a package for including transposable elements in differential expression analysis of RNA-seq datasets. *Bioinformatics* 31: 3593–3599

2191 Jorge-Oliva M, van Weering JRT & Scheper W (2023) Structurally and Morphologically
2192 Distinct Pathological Tau Assemblies Differentially Affect GVB Accumulation. *Int J Mol*
2193 *Sci* 24: 10865

2194 Kang SG, Han ZZ, Daude N, McNamara E, Wohlgemuth S, Molina-Porcel L, Safar JG, Mok
2195 SA & Westaway D (2021) Pathologic tau conformer ensembles induce dynamic, liquid-
2196 liquid phase separation events at the nuclear envelope. *BMC Biol* 19: 1–21

2197 Karin M & Chang L (2001) AP-1--glucocorticoid receptor crosstalk taken to a higher level. *J*
2198 *Endocrinol* 169: 447–451

2199 Kawakami E, Nakaoka S, Ohta T & Kitano H (2016) Weighted enrichment method for
2200 prediction of transcription regulators from transcriptome and global chromatin
2201 immunoprecipitation data. *Nucleic Acids Res* 44: 5010–5021

2202 Kay KR, Smith C, Wright AK, Serrano-Pozo A, Pooler AM, Koffie R, Bastin ME, Bak TH,
2203 Abrahams S, Kopeikina KJ, *et al* (2013) Studying synapses in human brain with array
2204 tomography and electron microscopy. *Nat Protoc* 8: 1366–1380

2205 King MR & Petry S (2020) Phase separation of TPX2 enhances and spatially coordinates
2206 microtubule nucleation. *Nature Communications 2020 11:1* 11: 1–13

2207 Klein HU, McCabe C, Gjoneska E, Sullivan SE, Kaskow BJ, Tang A, Smith R V., Xu J,
2208 Pfenning AR, Bernstein BE, *et al* (2019) Epigenome-wide study uncovers large-scale
2209 changes in histone acetylation driven by tau pathology in aging and Alzheimer's human
2210 brains. *Nat Neurosci* 22: 37–46

2211 Korotkevich G, Sukhov V, Budin N, Shpak B, Artyomov MN & Sergushichev A (2021) Fast
2212 gene set enrichment analysis. *bioRxiv*: 060012

2213 Koudinov AR & Koudinova N V. (2001) Essential role for cholesterol in synaptic plasticity and
2214 neuronal degeneration. *FASEB J* 15: 1858–1860

2215 Kovács KA, Steullet P, Steinmann M, Do KQ, Magistretti PJ, Halfon O & Cardinaux JR
2216 (2007) TORC1 is a calcium- and cAMP-sensitive coincidence detector involved in
2217 hippocampal long-term synaptic plasticity. *Proc Natl Acad Sci U S A* 104: 4700–4705

2218 Kumari S, Dhapola R & Reddy DHK (2023) Apoptosis in Alzheimer's disease: insight into the
2219 signaling pathways and therapeutic avenues. *Apoptosis* 28: 943–957

2220 Langmead B & Salzberg SL (2012) Fast gapped-read alignment with Bowtie 2. *Nature*
2221 *Methods 2012 9:4* 9: 357–359

2222 Lawrence M, Huber W, Pagès H, Aboyoun P, Carlson M, Gentleman R, Morgan MT & Carey
2223 VJ (2013) Software for Computing and Annotating Genomic Ranges. *PLoS Comput Biol*
2224 9: e1003118

2225 Leng K, Li E, Eser R, Piergies A, Sit R, Tan M, Neff N, Li SH, Rodriguez RD, Suemoto CK, *et*
2226 *al* (2021) Molecular characterization of selectively vulnerable neurons in Alzheimer's
2227 disease. *Nat Neurosci* 24: 276–287

2228 Lewis CA, Griffiths B, Santos CR, Pende M & Schulze A (2011) Regulation of the SREBP
2229 transcription factors by mTORC1. *Biochem Soc Trans* 39: 495–499

2230 Li D, Zhang J & Liu Q (2022) Brain cell type-specific cholesterol metabolism and implications
2231 for learning and memory. *Trends Neurosci* 45: 401–414

2232 Li S, Ye T, Hou Z, Wang Y, Hao Z & Chen J (2025) FOXO6: A unique transcription factor in
2233 disease regulation and therapeutic potential. *Pharmacol Res* 214: 107691

2234 Li S, Zhang C, Takemori H, Zhou Y & Xiong ZQ (2009) TORC1 Regulates Activity-
2235 Dependent CREB-Target Gene Transcription and Dendritic Growth of Developing
2236 Cortical Neurons. *Journal of Neuroscience* 29: 2334–2343

2237 Li X, Wang S, Xie Y, Jiang H, Guo J, Wang Y, Peng Z, Hu M, Wang M, Wang J, *et al* (2023)
2238 Deacetylation induced nuclear condensation of HP1γ promotes multiple myeloma drug
2239 resistance. *Nature Communications 2023 14:1* 14: 1290-

2240 Liberzon A, Birger C, Thorvaldsdóttir H, Ghandi M, Mesirov JP & Tamayo P (2015) The
2241 Molecular Signatures Database (MSigDB) hallmark gene set collection. *Cell Syst* 1:
2242 417–425

2243 Liu C & Götz J (2013) Profiling murine tau with 0N, 1N and 2N isoform-specific antibodies in
2244 brain and peripheral organs reveals distinct subcellular localization, with the 1N isoform
2245 being enriched in the nucleus. *PLoS One* 8: 1–18

2246 Liu S, Heumüller SE, Hossinger A, Müller SA, Buravlova O, Lichtenthaler SF, Denner P &
2247 Vorberg IM (2023) Reactivated endogenous retroviruses promote protein aggregate
2248 spreading. *Nat Commun* 14

2249 Lopes S, Vaz-Silva J, Pinto V, Dalla C, Kokras N, Bedenk B, Mack N, Czisch M, Almeida
2250 OFX, Sousa N, *et al* (2016) Tau protein is essential for stress-induced brain pathology.
2251 *Proc Natl Acad Sci U S A* 113: E3755–E3763

2252 Love MI, Huber W & Anders S (2014a) Moderated estimation of fold change and dispersion
2253 for RNA-seq data with DESeq2. *Genome Biol* 15: 1–21

2254 Love MI, Huber W & Anders S (2014b) Moderated estimation of fold change and dispersion
2255 for RNA-seq data with DESeq2. *Genome Biol* 15: 1–21

2256 Lu T, Aron L, Zullo J, Pan Y, Kim H, Chen Y, Yang TH, Kim HM, Drake D, Liu XS, *et al*
2257 (2014) REST and stress resistance in ageing and Alzheimer's disease. *Nature* 507:
2258 448–454

2259 Luna-Muñoz J, Chávez-Macías L, García-Sierra F & Mena R (2007) Earliest stages of tau
2260 conformational changes are related to the appearance of a sequence of specific
2261 phospho-dependent tau epitopes in Alzheimer's disease. *Journal of Alzheimer's*
2262 *Disease* 12: 365–375

2263 Mailman T, Hariharan M & Karten B (2011) Inhibition of neuronal cholesterol biosynthesis
2264 with lovastatin leads to impaired synaptic vesicle release even in the presence of
2265 lipoproteins or geranylgeraniol. *J Neurochem* 119: 1002–1015

2266 Maina MB, Bailey LJ, Wagih S, Biasetti L, Pollack SJ, Quinn JP, Thorpe JR, Doherty AJ &
2267 Serpell LC (2018) The involvement of tau in nucleolar transcription and the stress
2268 response. *Acta Neuropathol Commun* 6: 1–13

2269 Mandelkow EM, Biernat J, Drewes G, Gustke N, Trinczek B & Mandelkow E (1995) Tau
2270 domains, phosphorylation, and interactions with microtubules. *Neurobiol Aging* 16: 355–
2271 362

2272 Mansuroglu Z, Benhelli-Mokrani H, Marcato V, Sultan A, Violet M, Chauderlier A, Delattre L,
2273 Loyens A, Talahari S, Bégard S, *et al* (2016) Loss of Tau protein affects the structure,
2274 transcription and repair of neuronal pericentromeric heterochromatin. *Sci Rep* 6: 1–16

2275 Manuelidis L & Borden J (1988) Reproducible compartmentalization of individual
2276 chromosome domains in human CNS cells revealed by in situ hybridization and three-
2277 dimensional reconstruction. *Chromosoma* 96: 397–410

2278 Martínez M & Inestrosa NC (2021) The transcriptional landscape of Alzheimer's disease and
2279 its association with Wnt signaling pathway. *Neurosci Biobehav Rev* 128: 454–466

2280 McClelland S, Brennan GP, Dubé C, Rajpara S, Iyer S, Richichi C, Bernard C & Baram TZ
2281 (2014) The transcription factor NRSF contributes to epileptogenesis by selective
2282 repression of a subset of target genes. *Elife* 3: e01267

2283 McClelland S, Flynn C, Dubé C, Richichi C, Zha Q, Ghestem A, Esclapez M, Bernard C &
2284 Baram TZ (2011) Neuron-restrictive silencer factor-mediated hyperpolarization-activated

2285 cyclic nucleotide gated channelopathy in experimental temporal lobe epilepsy. *Ann*
2286 *Neurol* 70: 454–465

2287 Meers MP, Tenenbaum D & Henikoff S (2019) Peak calling by Sparse Enrichment Analysis
2288 for CUT&RUN chromatin profiling. *Epigenetics Chromatin* 12: 1–11

2289 Mehta IS, Amira M, Harvey AJ & Bridger JM (2010) Rapid chromosome territory relocation by
2290 nuclear motor activity in response to serum removal in primary human fibroblasts.
2291 *Genome Biol* 11: R5-

2292 Melhuish TA, Chung DD, Bjerke GA & Wotton D (2010) Tgif1 represses apolipoprotein gene
2293 expression in liver. *J Cell Biochem* 111: 380–390

2294 Meuleman W, Peric-Hupkes D, Kind J, Beaudry JB, Pagie L, Kellis M, Reinders M, Wessels
2295 L & Van Steensel B (2013) Constitutive nuclear lamina–genome interactions are highly
2296 conserved and associated with A/T-rich sequence. *Genome Res* 23: 270

2297 Monroy-Ramírez HC, Basurto-Islas G, Mena R, Cisneros B, Binder LI, Avila J & Garcia-
2298 Sierra F (2013) Alterations in the nuclear architecture produced by the overexpression
2299 of tau protein in neuroblastoma cells. *Journal of Alzheimer's Disease* 36: 503–520

2300 Morchikh M, Cribier A, Raffel R, Amraoui S, Cau J, Severac D, Dubois E, Schwartz O,
2301 Bennasser Y & Benkirane M (2017) HEXIM1 and NEAT1 Long Non-coding RNA Form a
2302 Multi-subunit Complex that Regulates DNA-Mediated Innate Immune Response. *Mol*
2303 *Cell* 67: 387-399.e5

2304 Musi N, Valentine JM, Sickora KR, Baeuerle E, Thompson CS, Shen Q & Orr ME (2018) Tau
2305 protein aggregation is associated with cellular senescence in the brain. *Aging Cell* 17

2306 Olins AL, Rhodes G, Welch DBM, Zwerger M & Olins DE (2010) Lamin B receptor. *Nucleus*
2307 1: 53–70

2308 Orr ME, Sullivan AC & Frost B (2017) A Brief Overview of Tauopathy: Causes,
2309 Consequences, and Therapeutic Strategies. *Trends Pharmacol Sci* 38: 637

2310 Padeken J, Methot SP & Gasser SM (2022) Establishment of H3K9-methylated
2311 heterochromatin and its functions in tissue differentiation and maintenance. *Nature*
2312 *Reviews Molecular Cell Biology 2022 23:9* 23: 623–640

2313 Paonessa F, Evans LD, Solanki R, Larrieu D, Wray S, Hardy J, Jackson SP & Livesey FJ
2314 (2019) Microtubules Deform the Nuclear Membrane and Disrupt Nucleocytoplasmic
2315 Transport in Tau-Mediated Frontotemporal Dementia. *Cell Rep* 26: 582-593.e5

2316 Parra Bravo C, Naguib SA & Gan L (2024) Cellular and pathological functions of tau. *Nature*
2317 *Reviews Molecular Cell Biology 2024 25:11* 25: 845–864

2318 Peterson TR, Sengupta SS, Harris TE, Carmack AE, Kang SA, Balderas E, Guertin DA,
2319 Madden KL, Carpenter AE, Finck BN, *et al* (2011) mTOR complex 1 regulates lipin 1
2320 localization to control the SREBP pathway. *Cell* 146: 408

2321 Polioudaki H, Kourmouli N, Drosou V, Bakou A, Theodoropoulos PA, Singh PB,
2322 Giannakouros T & Georgatos SD (2001) Histones H3/H4 form a tight complex with the
2323 inner nuclear membrane protein LBR and heterochromatin protein 1. *EMBO Rep* 2: 920

2324 Pramfalk C, Melhuish TA, Wotton D, Jiang ZY, Eriksson M & Parini P (2014) TG-interacting
2325 factor 1 acts as a transcriptional repressor of sterol O-acyltransferase 2. *J Lipid Res* 55:
2326 709

2327 Prissette M, Fury W, Koss M, Racioppi C, Fedorova D, Dragileva E, Clarke G, Pohl T, Dugan
2328 J, Ahrens D, *et al* (2022) Disruption of nuclear envelope integrity as a possible initiating
2329 event in tauopathies. *Cell Rep* 40: 111249

2330 Ramirez P, Zuniga G, Sun W, Beckmann A, Ochoa E, DeVos SL, Hyman B, Chiu G, Roy
2331 ER, Cao W, *et al* (2022) Pathogenic tau accelerates aging-associated activation of
2332 transposable elements in the mouse central nervous system. *Prog Neurobiol* 208

2333 Rico T, Gilles M, Chauderlier A, Comptdaer T, Magnez R, Chwastyniak M, Drobecq H, Pinet
2334 F, Thuru X, Buée L, *et al* (2018) Tau Stabilizes Chromatin Compaction. *Front Cell Dev*
2335 *Biol* 9: 228–239

2336 Rothballer A & Kutay U (2013) The diverse functional LINCs of the nuclear envelope to the
2337 cytoskeleton and chromatin. *Chromosoma* 122: 415–429

2338 Rylski M, Amborska R, Zybura K, Michaluk P, Bielinska B, Konopacki FA, Wilczynski GM &
2339 Kaczmarek L (2009) JunB is a repressor of MMP-9 transcription in depolarized rat brain
2340 neurons. *Molecular and Cellular Neuroscience* 40: 98–110

2341 Sakurai K, Morita M, Aomine Y, Matsumoto M, Moriyama T, Kasahara E, Sekiyama A, Otani
2342 M, Oshima R, Loveland KL, *et al* (2024) Importin α4 deficiency induces psychiatric
2343 disorder-related behavioral deficits and neuroinflammation in mice. *Translational*
2344 *Psychiatry 2024 14:1* 14: 1–10

2345 Satoh JI, Yamamoto Y, Asahina N, Kitano S & Kino Y (2014) RNA-Seq Data Mining:
2346 Downregulation of NeuroD6 Serves as a Possible Biomarker for Alzheimer's Disease
2347 Brains. *Dis Markers* 2014: 123165

2348 Van Schaik T, Magnitov M, De Haas M, Breda J, De Wit E, Manjon AG, Medema RH, Gothe
2349 HJ, Roukos V, Buckle AJ, *et al* (2025) Coordinated control of genome-nuclear lamina
2350 interactions by topoisomerase 2B and lamin B receptor. *Nucleic Acids Res* 53

2351 Schep AN, Wu B, Buenrostro JD & Greenleaf WJ (2017) chromVAR: inferring transcription-
2352 factor-associated accessibility from single-cell epigenomic data. *Nature Methods 2017*
2353 *14:10* 14: 975–978

2354 Schmidt HB & Görlich D (2016) Transport Selectivity of Nuclear Pores, Phase Separation,
2355 and Membraneless Organelles. *Trends Biochem Sci* 41: 46–61

2356 Schneeweis A, Hillyer D, Lama T, Kim D, Palka C, Djemil S, Abdel-Ghani M, Mandella K,
2357 Zhu W, Alvarez N, *et al* (2024) Mass spectrometry identifies tau C-terminal
2358 phosphorylation cluster during neuronal hyperexcitation. *J Neurochem*

2359 Schwarz R, Koch P, Wilbrandt J & Hoffmann S (2022) Locus-specific expression analysis of
2360 transposable elements. *Brief Bioinform* 23

2361 Shah PP, Keough KC, Gjoni K, Santini GT, Abdill RJ, Wickramasinghe NM, Dundes CE,
2362 Karnay A, Chen A, Salomon REA, *et al* (2023) An atlas of lamina-associated chromatin
2363 across twelve human cell types reveals an intermediate chromatin subtype. *Genome*
2364 *Biol* 24: 1–35

2365 Shin KC, Ali Moussa HY & Park Y (2024) Cholesterol imbalance and neurotransmission
2366 defects in neurodegeneration. *Experimental & Molecular Medicine 2024 56:8* 56: 1685–
2367 1690

2368 Sjöberg MK, Shestakova E, Mansuroglu Z, Maccioni RB & Bonnefoy E (2006) Tau protein
2369 binds to pericentromeric DNA: a putative role for nuclear tau in nucleolar organization. *J*
2370 *Cell Sci* 119: 2025–2034

2371 Sohn C, Ma J, Ray WJ & Frost B (2023) Pathogenic tau decreases nuclear tension in
2372 cultured neurons. *Frontiers in Aging* 4: 1–11

2373 Sosa BA, Kutay U & Schwartz TU (2013) Structural insights into LINC complexes. *Curr Opin*
2374 *Struct Biol* 23: 285–291

2375 Spillantini MG & Goedert M (2013) Tau pathology and neurodegeneration. *Lancet Neurol* 12:
2376 609–622

2377 van Steensel B & Belmont AS (2017) Lamina-Associated Domains: Links with Chromosome
2378 Architecture, Heterochromatin, and Gene Repression. *Cell* 169: 780–791

2379 Subramanian A, Tamayo P, Mootha VK, Mukherjee S, Ebert BL, Gillette MA, Paulovich A,
2380 Pomeroy SL, Golub TR, Lander ES, *et al* (2005) Gene set enrichment analysis: A

knowledge-based approach for interpreting genome-wide expression profiles. *Proc Natl Acad Sci U S A* 102: 15545–15550

Sultan A, Nesslany F, Violet M, Bégard S, Loyens A, Talahari S, Mansuroglu Z, Marzin D, Sergeant N, Humez S, *et al* (2011) Nuclear Tau, a key player in neuronal DNA protection. *Journal of Biological Chemistry* 286: 4566–4575

Sun X, Shi Y, Saibaba S, Mandell JW & Bloom GS (2022) Extracellular Tau Oligomers Rapidly Induce Nuclear Invagination in Neurons. *Alzheimer's & Dementia* 18: e066169

Szklarczyk D, Kirsch R, Koutrouli M, Nastou K, Mehryary F, Hachilif R, Gable AL, Fang T, Doncheva NT, Pyysalo S, *et al* (2023) The STRING database in 2023: protein–protein association networks and functional enrichment analyses for any sequenced genome of interest. *Nucleic Acids Res* 51: D638–D646

Tai XY, Koepp M, Duncan JS, Fox N, Thompson P, Baxendale S, Liu JYW, Reeves C, Michalak Z & Thom M (2016) Hyperphosphorylated tau in patients with refractory epilepsy correlates with cognitive decline: a study of temporal lobe resections. *Brain* 139: 2441–2455

Tanabe H, Müller S, Neusser M, Von Hase J, Calcagno E, Cremer M, Solovei I, Cremer C & Cremer T (2002) Evolutionary conservation of chromosome territory arrangements in cell nuclei from higher primates. *Proc Natl Acad Sci U S A* 99: 4424–4429

Tao B, Gong W, Xu C, Ma Z, Mei J & Chen M (2024) The relationship between hypoxia and Alzheimer's disease: an updated review. *Front Aging Neurosci* 16: 1402774

Terry LJ, Shows EB & Wente SR (2007) Crossing the Nuclear Envelope: Hierarchical Regulation of Nucleocytoplasmic Transport. *Science (1979)* 318: 1412–1416

Tsai PL, Zhao C, Turner E & Schlieker C (2016) The Lamin B receptor is essential for cholesterol synthesis and perturbed by disease-causing mutations. *Elife* 5

Tuck BJ, Miller LVC, Katsinelos T, Smith AE, Wilson EL, Keeling S, Cheng S, Vaysburd MJ, Knox C, Tredgett L, *et al* (2022) Cholesterol determines the cytosolic entry and seeded aggregation of tau. *Cell Rep* 39: 110776

Varma VR, Büşra Lüleci H, Oommen AM, Varma S, Blackshear CT, Griswold ME, An Y, Roberts JA, O'Brien R, Pletnikova O, *et al* (2021) Abnormal brain cholesterol homeostasis in Alzheimer's disease—a targeted metabolomic and transcriptomic study. *npj Aging and Mechanisms of Disease 2021 7:1* 7: 1–14

Vester K, Preußner M, Holton N, Feng S, Schultz C, Heyd F & Wahl MC (2022) Recruitment of a splicing factor to the nuclear lamina for its inactivation. *Commun Biol* 5

Violet M, Delattre L, Tardivel M, Sultan A, Chauderlier A, Caillierez R, Talahari S, Nesslany F, Lefebvre B, Bonnefoy E, *et al* (2014) A major role for Tau in neuronal DNA and RNA protection in vivo under physiological and hyperthermic conditions. *Front Cell Neurosci* 8: 1–11

Wasser CR, Ertunc M, Liu X & Kavalali ET (2007) Cholesterol-dependent balance between evoked and spontaneous synaptic vesicle recycling. *J Physiol* 579: 413–429

Wegmann S, DeVos SL, Zeitler B, Marlen K, Bennett RE, Perez-Rando M, MacKenzie D, Yu Q, Commins C, Bannon RN, *et al* (2021) Persistent repression of tau in the brain using engineered zinc finger protein transcription factors. *Sci Adv* 7

Wente SR & Rout MP (2010) The nuclear pore complex and nuclear transport. *Cold Spring Harb Perspect Biol* 2: a000562

Yang J, Yao Y, Wang L, Yang C, Wang F, Guo J, Wang Z, Yang Z & Ming D (2017) Gastrin-releasing peptide facilitates glutamatergic transmission in the hippocampus and effectively prevents vascular dementia induced cognitive and synaptic plasticity deficits. *Exp Neurol* 287: 75–83

Zempel H, Thies E, Mandelkow E & Mandelkow EM (2010) Aβ oligomers cause localized Ca2+ elevation, missorting of endogenous Tau into dendrites, Tau phosphorylation, and destruction of microtubules and spines. *Journal of Neuroscience* 30: 11938–11950

Zhu A, Ibrahim JG & Love MI (2019) Heavy-tailed prior distributions for sequence count data: removing the noise and preserving large differences. *Bioinformatics* 35: 2084–2092

Zuccato C, Tartari M, Crotti A, Goffredo D, Valenza M, Conti L, Cataudella T, Leavitt BR, Hayden MR, Timmusk T, *et al* (2003) Huntingtin interacts with REST/NRSF to modulate the transcription of NRSE-controlled neuronal genes. *Nat Genet* 35: 76–83

Zuleger N, Robson MI & Schirmer EC (2011) The nuclear envelope as a chromatin organizer. *Nucleus* 2: 339

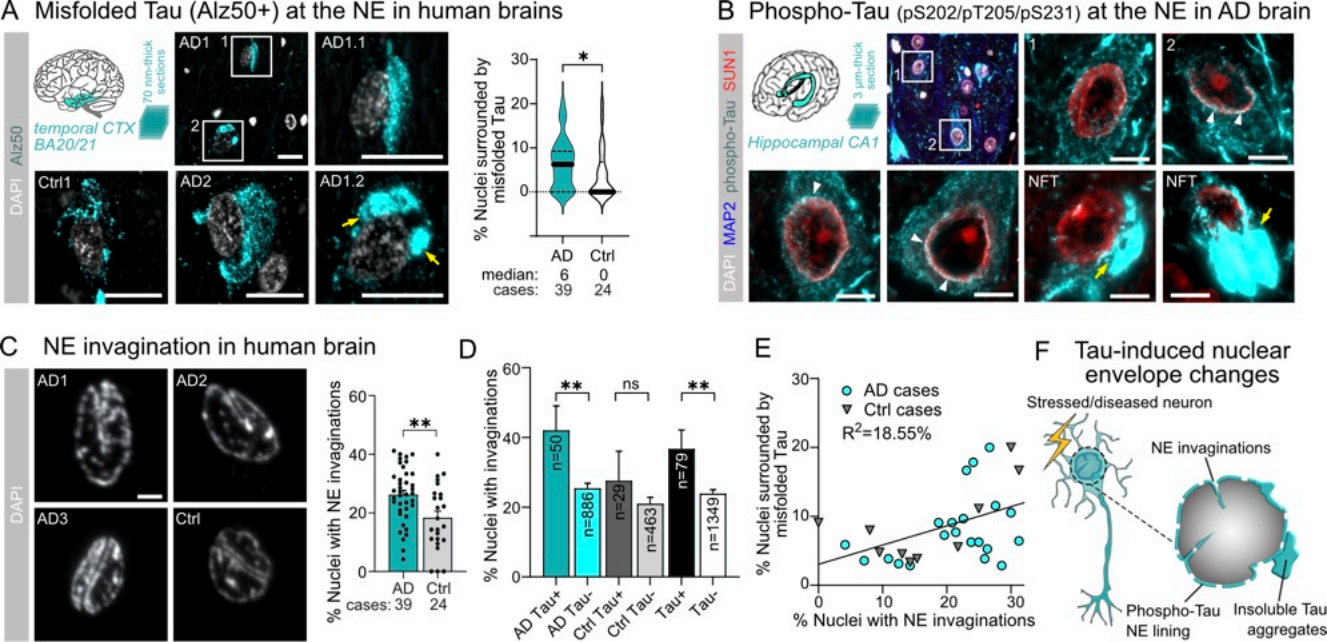
A Misfolded Tau (Alz50+) at the NE in human brains
Alz50
DAPI
temporal CTX
BA20/21
70 nm-thick sections
AD1
AD1.1
Ctrl1
AD2
AD1.2
% Nuclei surrounded by misfolded Tau
AD
Ctrl
median: 6 0
cases: 39 24
B Phospho-Tau (pS202/pT205/pS231) at the NE in AD brain
phospho-Tau
SUN1
DAPI
MAP2
3 µm-thick section
Hippocampal CA1
NFT
C NE invagination in human brain
AD1
AD2
AD3
Ctrl
% Nuclei with NE invaginations
cases: 39 24
D
% Nuclei with invaginations
n=50
n=886
n=29
n=463
n=79
n=1349
AD Tau+
AD Tau-
Ctrl Tau+
Ctrl Tau-
Tau+
Tau-
E
AD cases
Ctrl cases
R²=18.55%
% Nuclei surrounded by misfolded Tau
% Nuclei with NE invaginations
F Tau-induced nuclear envelope changes
Stressed/diseased neuron
NE invaginations
Phospho-Tau NE lining
Insoluble Tau aggregates

A AAV-mediated modulation of Tau concentration in hippocampal neurons

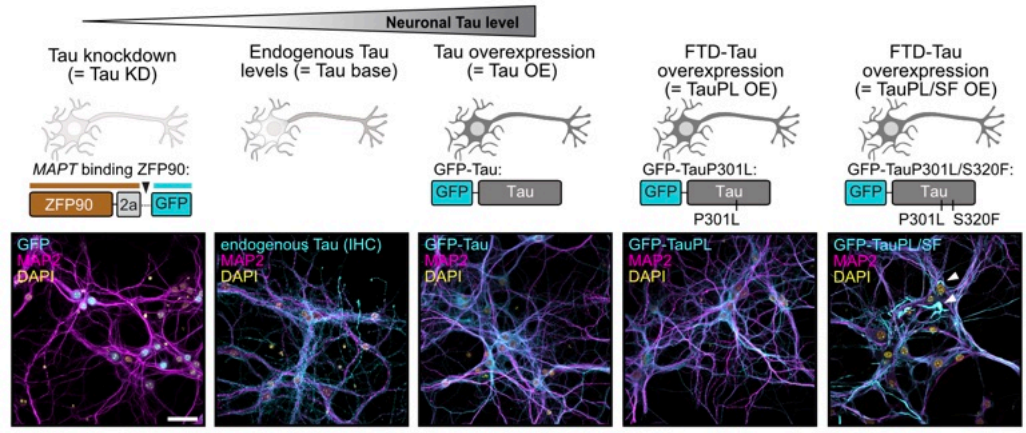

B Tau levels in neuronal lysates (by WB)

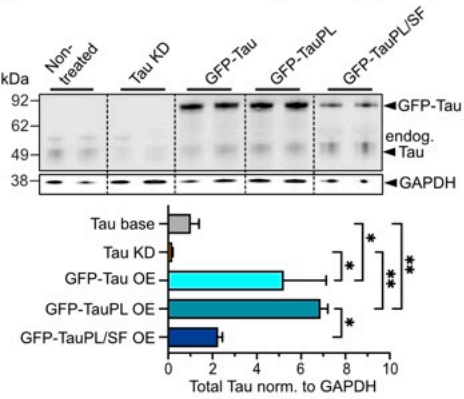

C Tau levels in neuronal cell bodies and nuclei (by IF)

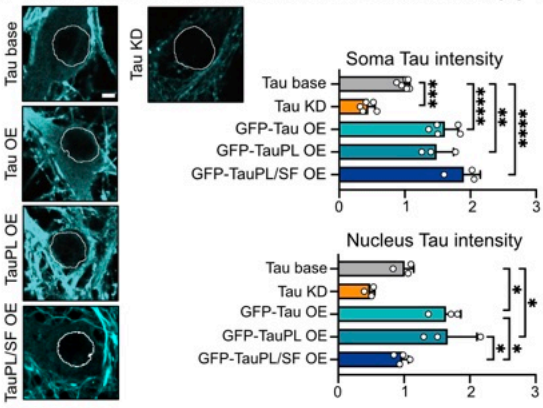

D Nuclear shape changes upon Tau modulation

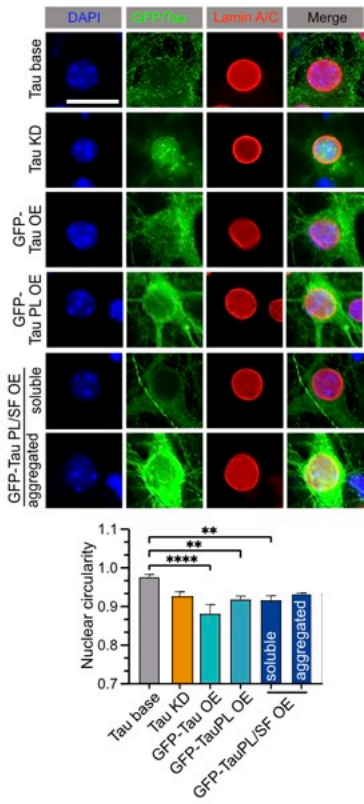

E Nuclear envelope damage & repair

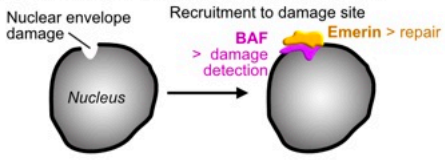

F Cytoplasmic and nuclear Tau constructs

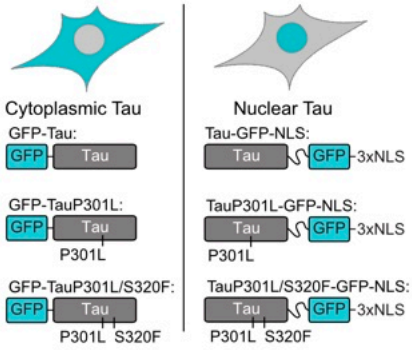

G Nuclear Tau increases NE damage in cells

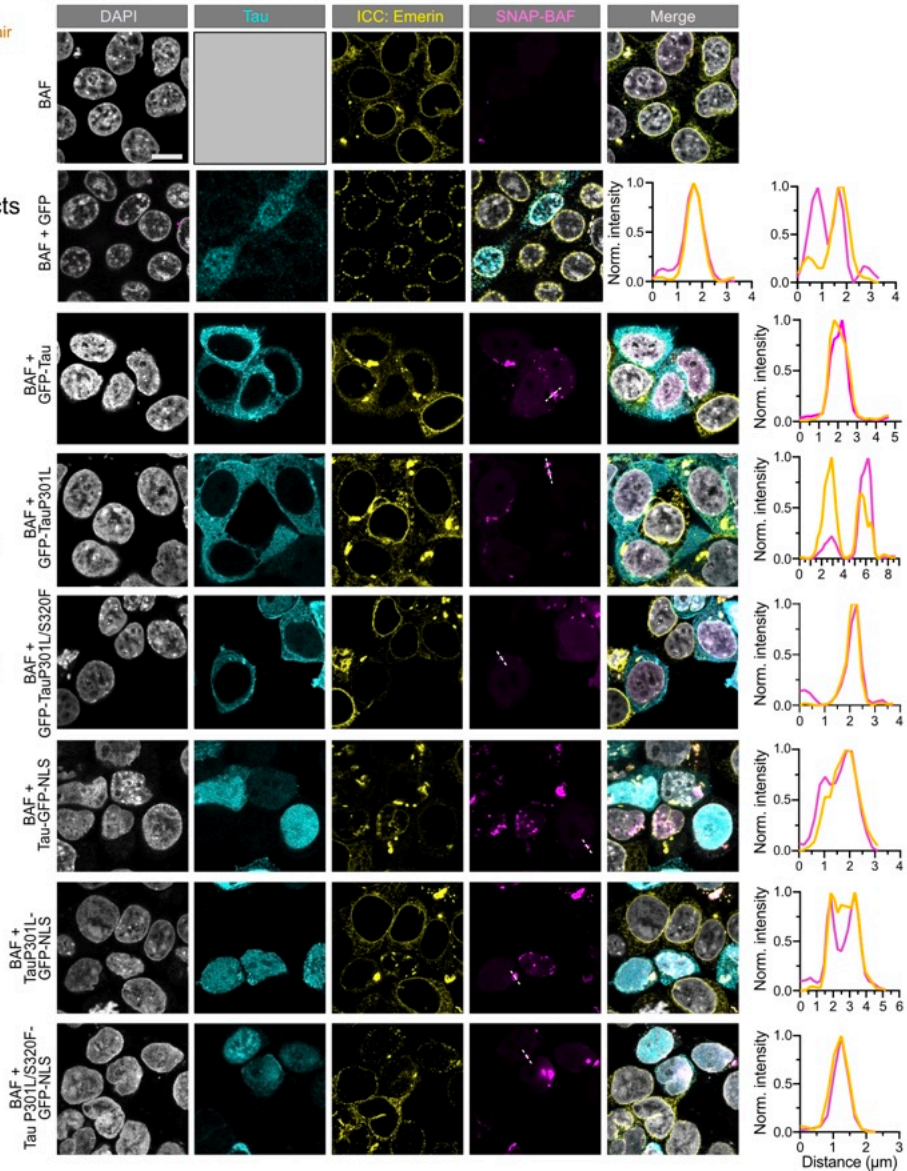

H BAF at the NE in Tau expressing cells

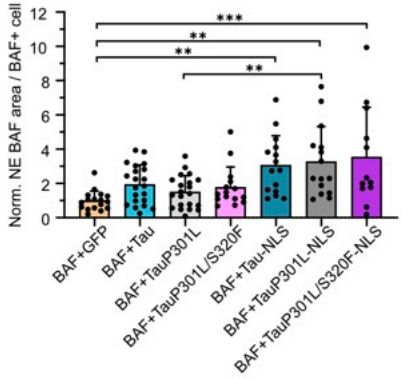

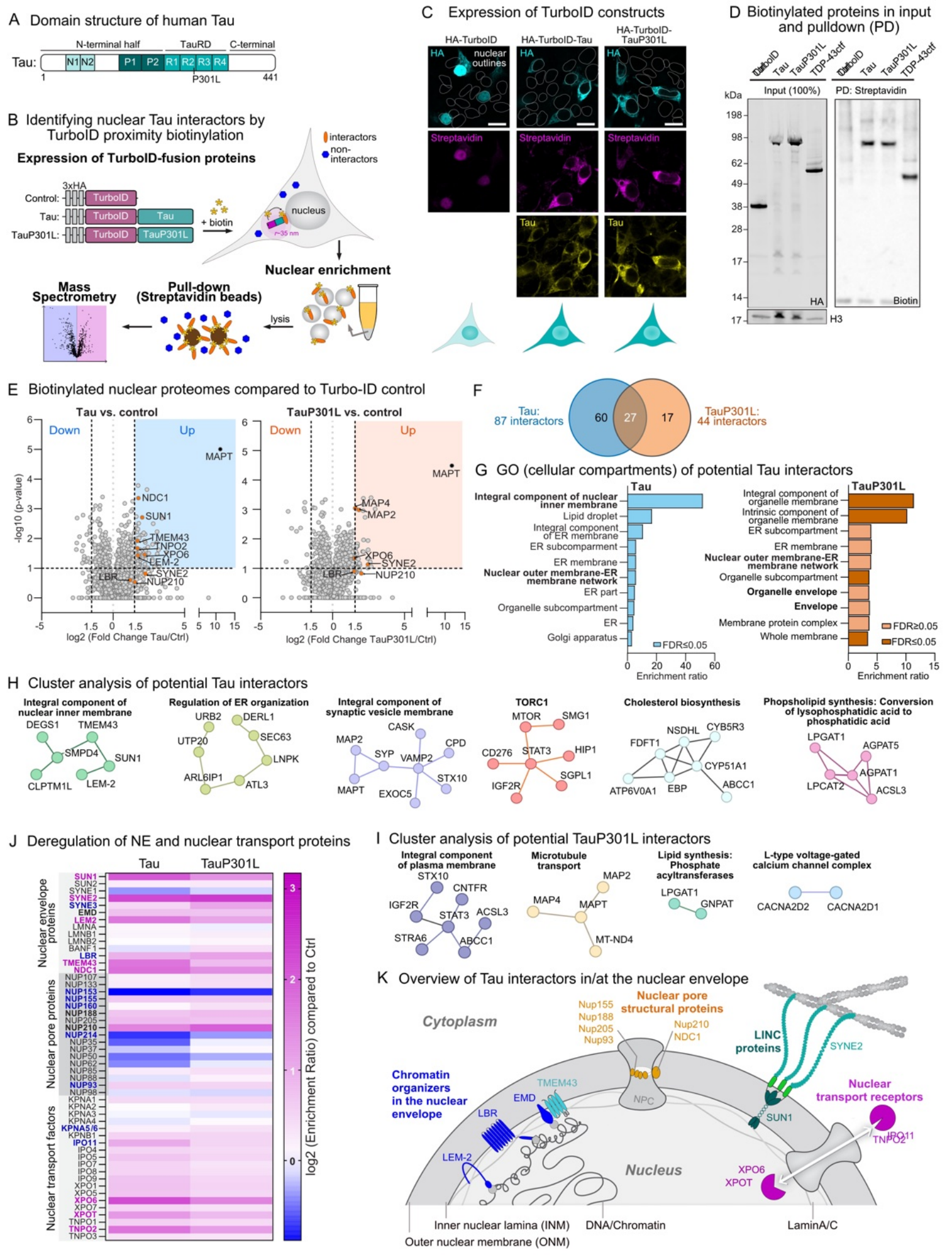
A Domain structure of human Tau
N-terminal half
TauRD
C-terminal
Tau:
N1 N2 P1 P2 R1 R2 R3 R4
1
P301L
441
B Identifying nuclear Tau interactors by TurboID proximity biotinylation
Expression of TurboID-fusion proteins
3xHA
Control:
Tau:
TauP301L:
TurboID
Tau
TauP301L
+ biotin
interactors
non-interactors
nucleus
~35 nm
Nuclear enrichment
lysis
Pull-down (Streptavidin beads)
Mass Spectrometry
C Expression of TurboID constructs
HA-TurboID
HA-TurboID-Tau
HA-TurboID-TauP301L
HA
nuclear outlines
Streptavidin
Tau
D Biotinylated proteins in input and pulldown (PD)
TurboID
Tau
TauP301L
TDP-43ctf
Input (100%)
PD: Streptavidin
kDa
198
98
62
49
38
28
17
14
17
HA
Biotin
H3
E Biotinylated nuclear proteomes compared to Turbo-ID control
Tau vs. control
TauP301L vs. control
Down
Up
-log10 (p-value)
MAPT
NDC1
SUN1
TMEM43
TNPO2
XPO6
LEM-2
SYNE2
LBR
NUP210
MAP4
MAP2
log2 (Fold Change Tau/Ctrl)
log2 (Fold Change TauP301L/Ctrl)
F
Tau: 87 interactors
60
27
17
TauP301L: 44 interactors
G GO (cellular compartments) of potential Tau interactors
Tau
TauP301L
Integral component of nuclear inner membrane
Lipid droplet
Integral component of ER membrane
ER subcomparment
ER membrane
Nuclear outer membrane-ER membrane network
ER part
Organelle subcompartment
ER
Golgi apparatus
Integral component of organelle membrane
Intrinsic component of organelle membrane
ER subcompartment
ER membrane
Nuclear outer membrane-ER membrane network
Organelle subcompartment
Organelle envelope
Envelope
Membrane protein complex
Whole membrane
FDR≤0.05
FDR≥0.05
Enrichment ratio
H Cluster analysis of potential Tau interactors
Integral component of nuclear inner membrane
DEGS1
TMEM43
SMPD4
SUN1
CLPTM1L
LEM-2
Regulation of ER organization
URB2
DERL1
UTP20
SEC63
LNPK
ARL6IP1
ATL3
Integral component of synaptic vesicle membrane
CASK
MAP2
CPD
SYP
VAMP2
STX10
MAPT
EXOC5
TORC1
MTOR
SMG1
CD276
STAT3
HIP1
SGPL1
IGF2R
Cholesterol biosynthesis
NSDHL
CYB5R3
FDFT1
CYP51A1
ATP6V0A1
EBP
ABCC1
Phopsholipid synthesis: Conversion of lysophosphatidic acid to phosphatidic acid
LPGAT1
AGPAT5
AGPAT1
LPCAT2
ACSL3
J Deregulation of NE and nuclear transport proteins
Tau
TauP301L
Nuclear envelope proteins
SUN1
SUN2
SYNE1
SYNE2
SYNE3
EMD
LEM2
LMNA
LMNB1
LMNB2
BANF1
LBR
TMEM43
NDC1
Nuclear pore proteins
NUP107
NUP133
NUP153
NUP155
NUP160
NUP188
NUP205
NUP210
NUP214
NUP35
NUP37
NUP50
NUP62
NUP85
NUP88
NUP93
NUP98
Nuclear transport factors
KPNA1
KPNA2
KPNA3
KPNA4
KPNA5/6
KPNB1
IPO11
IPO4
IPO5
IPO7
IPO8
IPO9
XPO1
XPO5
XPO6
XPO7
XPOT
TNPO1
TNPO2
TNPO3
log2 (Enrichment Ratio) compared to Ctrl
I Cluster analysis of potential TauP301L interactors
Integral component of plasma membrane
STX10
CNTFR
IGF2R
STAT3
ACSL3
STRA6
ABCC1
Microtubule transport
MAP2
MAP4
MAPT
MT-ND4
Lipid synthesis: Phosphate acyltransferases
LPGAT1
GNPAT
L-type voltage-gated calcium channel complex
CACNA2D2
CACNA2D1
K Overview of Tau interactors in/at the nuclear envelope
Cytoplasm
Nuclear pore structural proteins
Nup155
Nup188
Nup205
Nup93
Nup210
NDC1
LINC proteins
SYNE2
Chromatin organizers in the nuclear envelope
TMEM43
EMD
LBR
LEM-2
NPC
SUN1
Nuclear transport receptors
IPO11
TNPO2
XPO6
XPOT
Nucleus
Inner nuclear lamina (INM)
DNA/Chromatin
LaminA/C
Outer nuclear membrane (ONM)

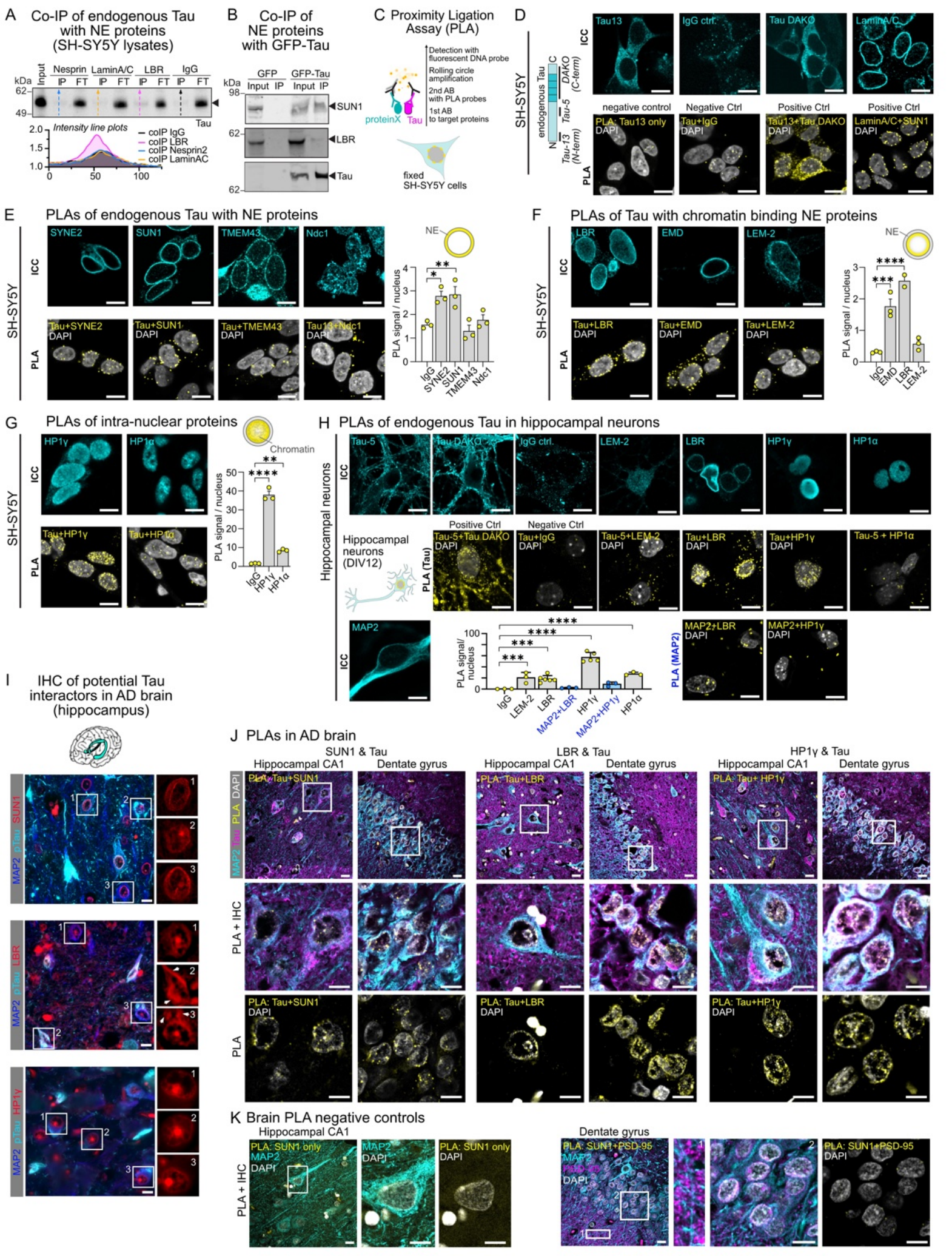
A Co-IP of endogenous Tau with NE proteins (SH-SY5Y lysates)
Input
Nesprin
LaminA/C
LBR
IgG
IP FT IP FT IP FT IP FT
kDa
62
49
Tau
Intensity line plots
coIP IgG
coIP LBR
coIP Nesprin2
coIP LaminAC
B Co-IP of NE proteins with GFP-Tau
GFP
GFP-Tau
Input IP Input IP
kDa
98
62
SUN1
LBR
Tau
C Proximity Ligation Assay (PLA)
Detection with fluorescent DNA probe
Rolling circle amplification
2nd AB with PLA probes
1st AB to target proteins
proteinX
Tau
fixed SH-SY5Y cells
D
SH-SY5Y
ICC
PLA
endogenous Tau
C
DAKO (C-term)
Tau-5
Tau-13 (N-term)
N
Tau13
IgG ctrl.
Tau DAKO
LaminA/C
negative control
Negative Ctrl
Positive Ctrl
Positive Ctrl
PLA: Tau13 only
DAPI
Tau+IgG
DAPI
Tau13+Tau DAKO
DAPI
LaminA/C+SUN1
DAPI
E PLAs of endogenous Tau with NE proteins
SH-SY5Y
ICC
PLA
SYNE2
SUN1
TMEM43
Ndc1
Tau+SYNE2
DAPI
Tau+SUN1
DAPI
Tau+TMEM43
DAPI
Tau13+Ndc1
DAPI
NE
PLA signal / nucleus
IgG
SYNE2
SUN1
TMEM43
Ndc1
F PLAs of Tau with chromatin binding NE proteins
SH-SY5Y
ICC
PLA
LBR
EMD
LEM-2
Tau+LBR
DAPI
Tau+EMD
DAPI
Tau+LEM-2
DAPI
NE
PLA signal / nucleus
IgG
EMD
LBR
LEM-2
G PLAs of intra-nuclear proteins
SH-SY5Y
ICC
PLA
HP1γ
HP1α
Tau+HP1γ
Tau+HP1α
Chromatin
PLA signal / nucleus
IgG
HP1γ
HP1α
H PLAs of endogenous Tau in hippocampal neurons
Hippocampal neurons
ICC
Tau-5
Tau DAKO
IgG ctrl.
LEM-2
LBR
HP1γ
HP1α
Hippocampal neurons (DIV12)
Positive Ctrl
Negative Ctrl
PLA (Tau)
Tau-5+Tau DAKO
DAPI
Tau+IgG
DAPI
Tau-5+LEM-2
DAPI
Tau+LBR
DAPI
Tau+HP1γ
DAPI
Tau-5 + HP1α
ICC
MAP2
PLA signal/ nucleus
IgG
LEM-2
LBR
MAP2+LBR
HP1γ
MAP2+HP1γ
HP1α
PLA (MAP2)
MAP2+LBR
DAPI
MAP2+HP1γ
DAPI
I IHC of potential Tau interactors in AD brain (hippocampus)
MAP2 pTau SUN1
MAP2 pTau LBR
MAP2 pTau HP1γ
J PLAs in AD brain
SUN1 & Tau
LBR & Tau
HP1γ & Tau
Hippocampal CA1
Dentate gyrus
MAP2 Tau PLA DAPI
PLA: Tau+SUN1
PLA: Tau+LBR
PLA: Tau+ HP1γ
PLA + IHC
PLA
PLA: Tau+SUN1
DAPI
PLA: Tau+LBR
DAPI
PLA: Tau+HP1γ
DAPI
K Brain PLA negative controls
Hippocampal CA1
Dentate gyrus
PLA + IHC
PLA: SUN1 only
MAP2
DAPI
MAP2
DAPI
PLA: SUN1 only
DAPI
PLA: SUN1+PSD-95
MAP2
PSD-95
DAPI
PLA: SUN1+PSD-95
DAPI

A Tau-induced NE invaginations and nuclear inclusions in cells

Tau-LBR co-expression

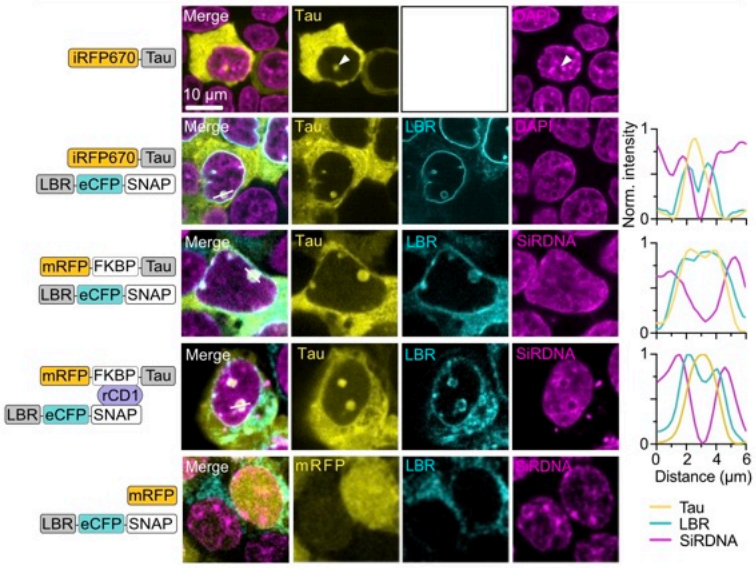

Tau-SUN1 co-expression

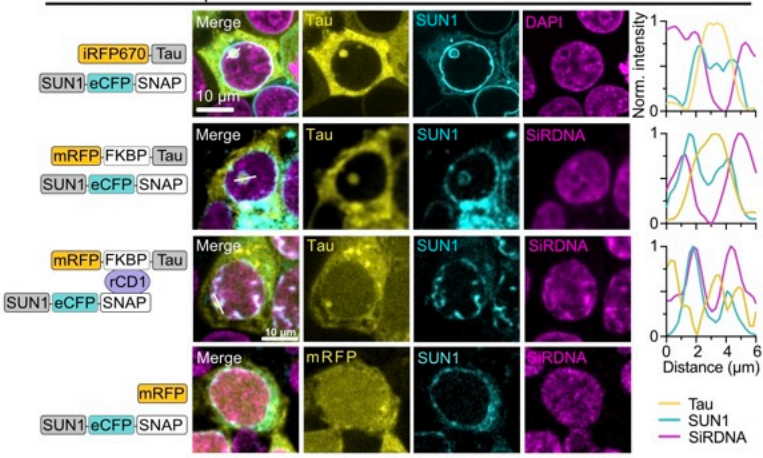

B

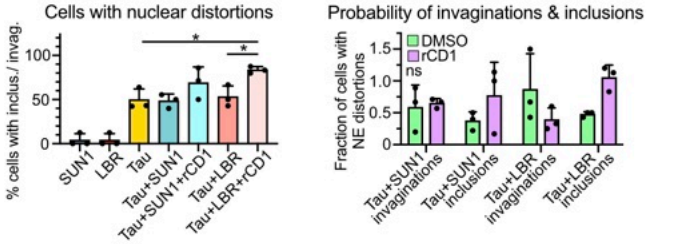

C Co-localization of NE proteins with nuclear Tau inclusions

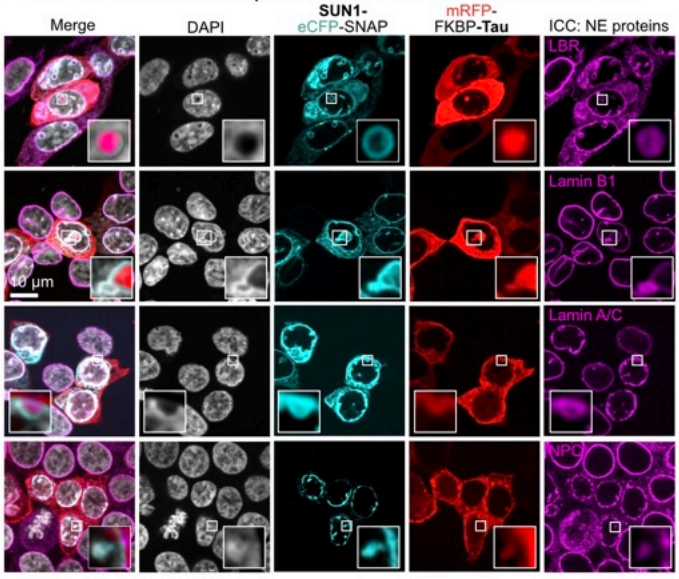

D Co-loc. of cytoplasmic proteins with nuclear Tau inclusions

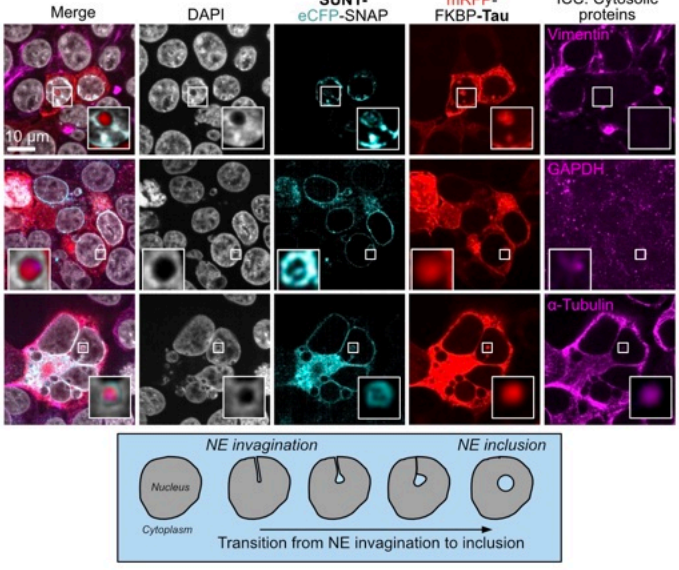

E Tau nuclear inclusions in relation to nuclear marker proteins

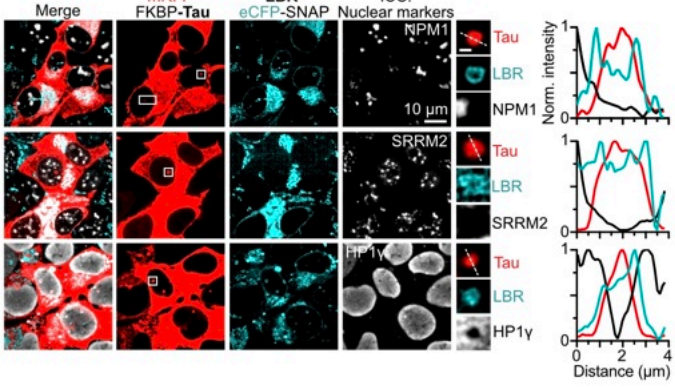

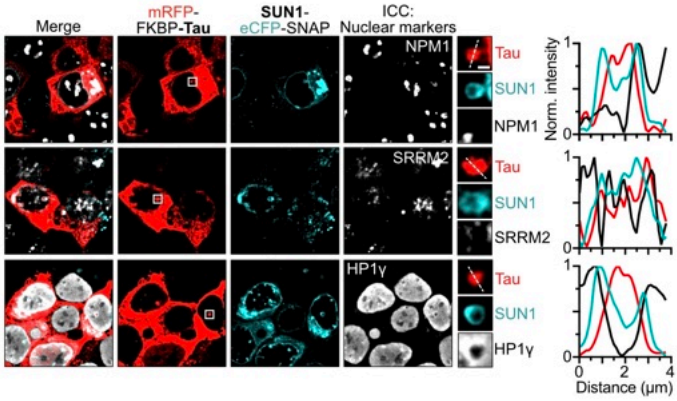

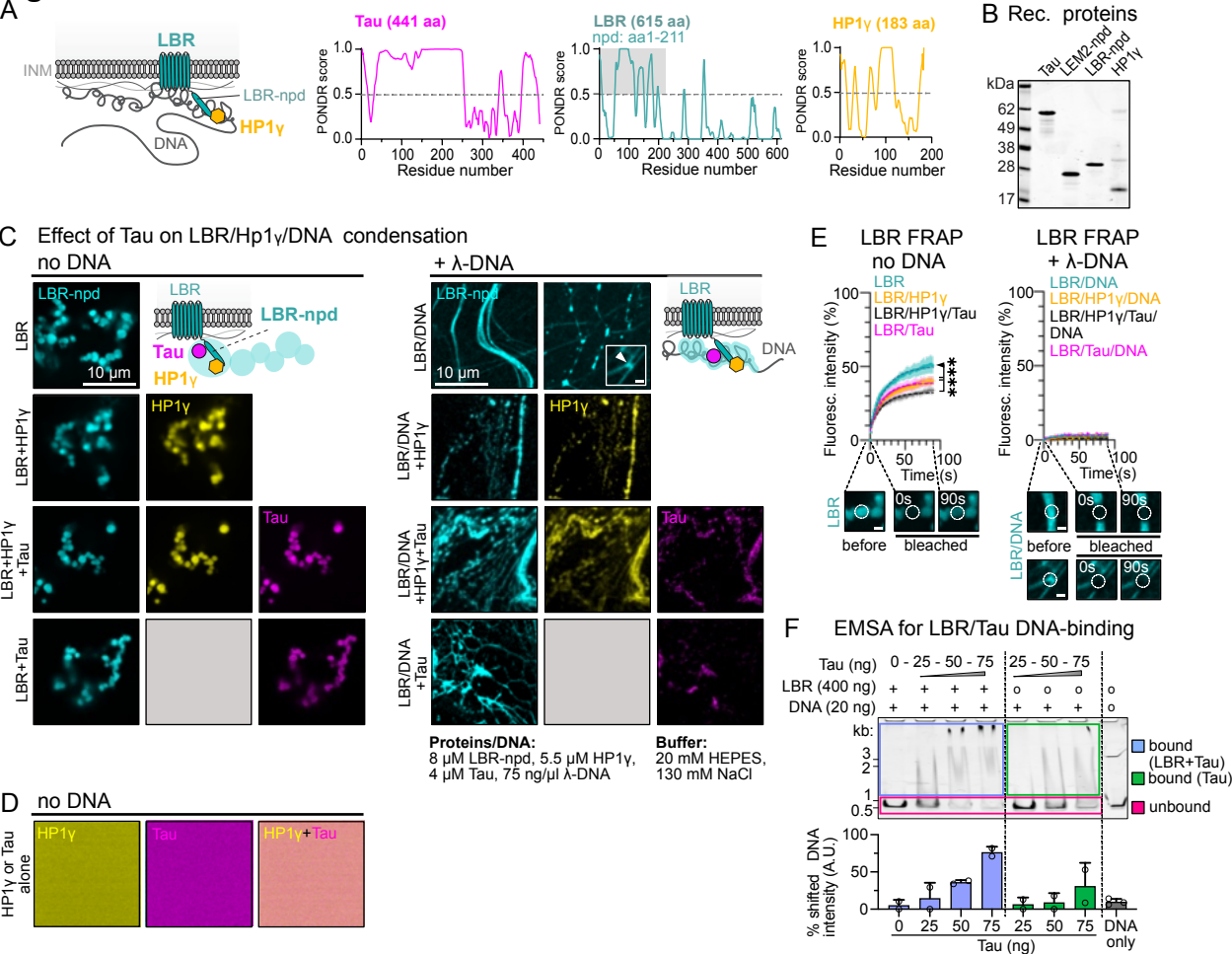
A
LBR
INM
LBR-npd
HP1γ
DNA
Tau (441 aa)
LBR (615 aa)
npd: aa1-211
HP1γ (183 aa)
PONDR score
Residue number
B Rec. proteins
Tau
LEM2-npd
LBR-npd
HP1γ
kDa
62
49
38
28
17
C Effect of Tau on LBR/Hp1γ/DNA condensation
no DNA
+ λ-DNA
LBR-npd
LBR
Tau
HP1γ
DNA
10 µm
LBR
LBR+HP1γ
LBR+HP1γ +Tau
LBR+Tau
LBR/DNA
LBR/DNA +HP1γ
LBR/DNA +HP1γ+Tau
LBR/DNA +Tau
Proteins/DNA:
8 µM LBR-npd, 5.5 µM HP1γ, 4 µM Tau, 75 ng/µl λ-DNA
Buffer:
20 mM HEPES, 130 mM NaCl
D no DNA
HP1γ or Tau alone
HP1γ
Tau
HP1γ+Tau
E LBR FRAP
no DNA
+ λ-DNA
LBR
LBR/HP1γ
LBR/HP1γ/Tau
LBR/Tau
LBR/DNA
LBR/HP1γ/DNA
LBR/HP1γ/Tau/ DNA
LBR/Tau/DNA
Fluoresc. intensity (%)
Time (s)
0s
90s
before
bleached
F EMSA for LBR/Tau DNA-binding
Tau (ng)
0 - 25 - 50 - 75
25 - 50 - 75
LBR (400 ng)
DNA (20 ng)
kb:
bound (LBR+Tau)
bound (Tau)
unbound
% shifted DNA intensity (A.U.)
DNA only

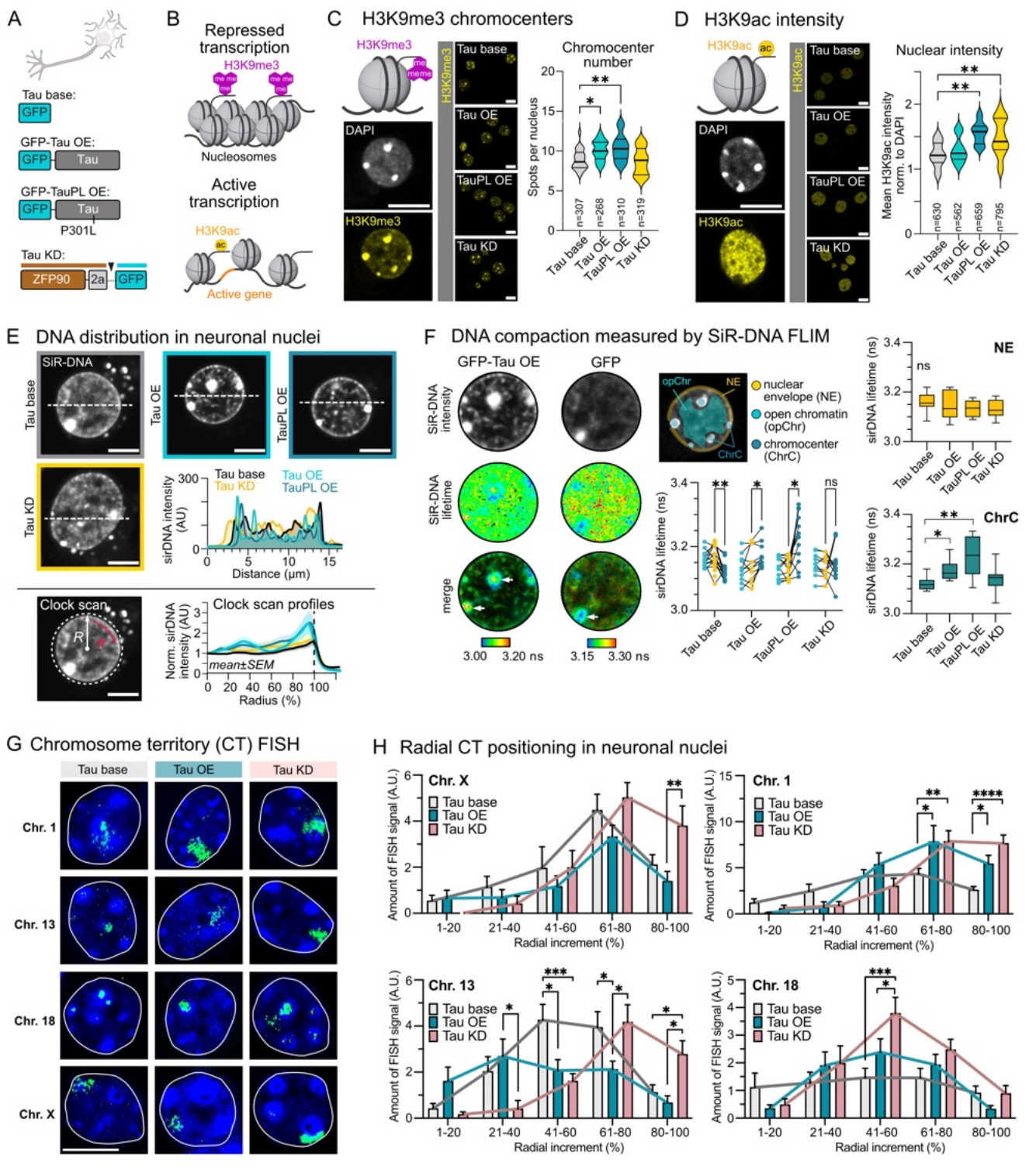
A
Tau base:
GFP
GFP-Tau OE:
GFP
Tau
GFP-TauPL OE:
GFP
Tau
P301L
Tau KD:
ZFP90
2a
GFP
B
Repressed transcription
H3K9me3
me me me
Nucleosomes
Active transcription
H3K9ac
ac
Active gene
C
H3K9me3 chromocenters
H3K9me3
me
DAPI
H3K9me3
Tau base
Tau OE
TauPL OE
Tau KD
Chromocenter number
Spots per nucleus
n=307
n=268
n=310
n=319
Tau base
Tau OE
TauPL OE
Tau KD
D
H3K9ac intensity
H3K9ac
ac
DAPI
H3K9ac
Tau base
Tau OE
TauPL OE
Tau KD
Nuclear intensity
Mean H3K9ac intensity norm. to DAPI
n=630
n=562
n=659
n=795
Tau base
Tau OE
TauPL OE
Tau KD
E
DNA distribution in neuronal nuclei
SiR-DNA
Tau base
Tau OE
TauPL OE
Tau KD
Tau base
Tau KD
Tau OE
TauPL OE
sirDNA intensity (AU)
Distance (µm)
Clock scan
R
Clock scan profiles
Norm. sirDNA intensity (AU)
mean±SEM
Radius (%)
F
DNA compaction measured by SiR-DNA FLIM
GFP-Tau OE
GFP
SiR-DNA intensity
SiR-DNA lifetime
merge
3.00
3.20 ns
3.15
3.30 ns
opChr
NE
ChrC
nuclear envelope (NE)
open chromatin (opChr)
chromocenter (ChrC)
sirDNA lifetime (ns)
Tau base
Tau OE
TauPL OE
Tau KD
NE
ns
ChrC
G
Chromosome territory (CT) FISH
Tau base
Tau OE
Tau KD
Chr. 1
Chr. 13
Chr. 18
Chr. X
H
Radial CT positioning in neuronal nuclei
Chr. X
Chr. 1
Chr. 13
Chr. 18
Tau base
Tau OE
Tau KD
Amount of FISH signal (A.U.)
Radial increment (%)
1-20
21-40
41-60
61-80
80-100

A RNAseq of neurons with different Tau levels

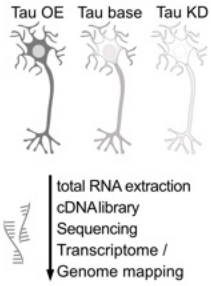

B Number of DEGs

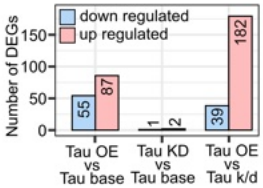

C Heatmap of DEGs *(differentially expressed genes)*

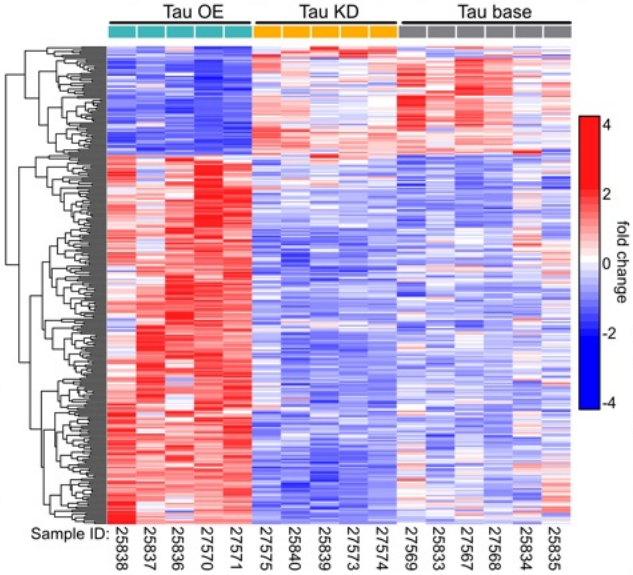

D Volcano plots of DEGs in Tau OE and Tau KD neurons

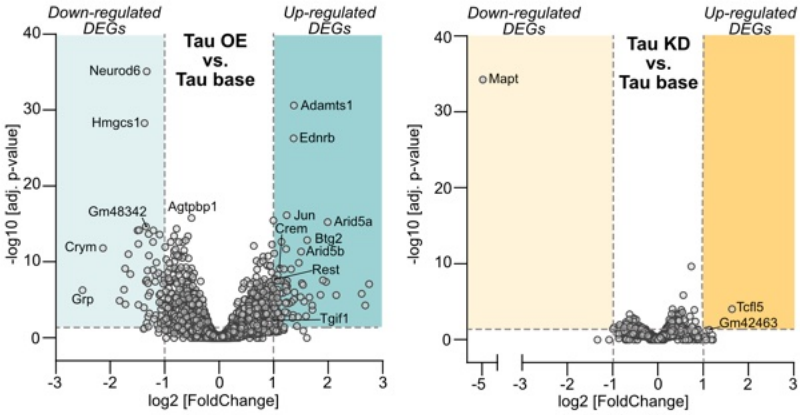

E Gene set enrichment analysis for all DEGs

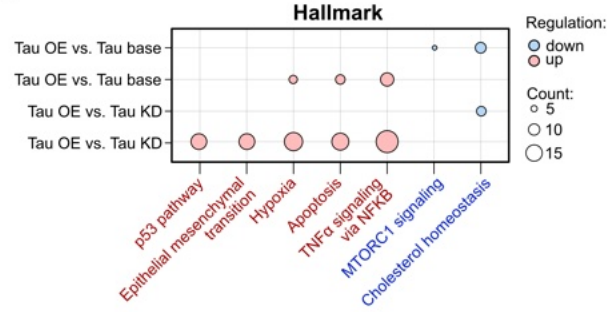

F GO of significant DEGs (Tau OE vs. Tau base)

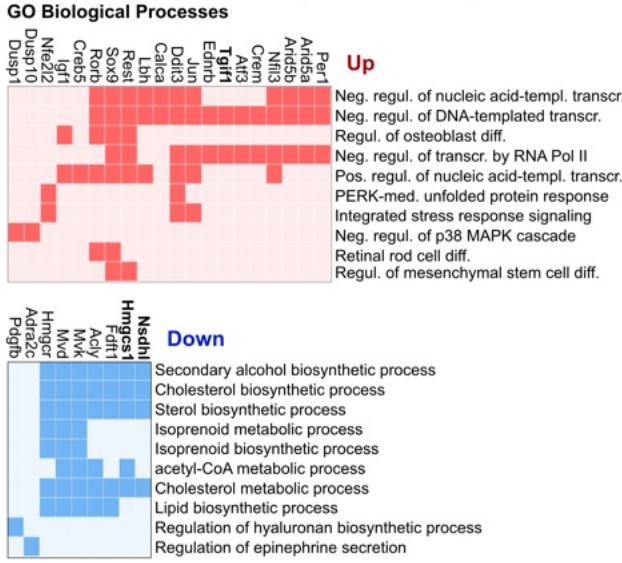

G Deregulated transcription factors Tau OE vs Tau base

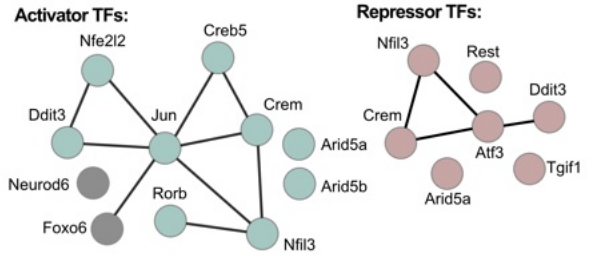

H qPCR of cholesterol synthesis related genes

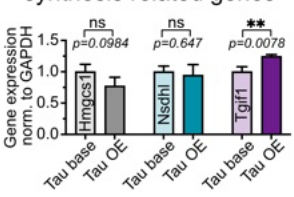

I Hmgcr protein in AD vs. ctrl CA1

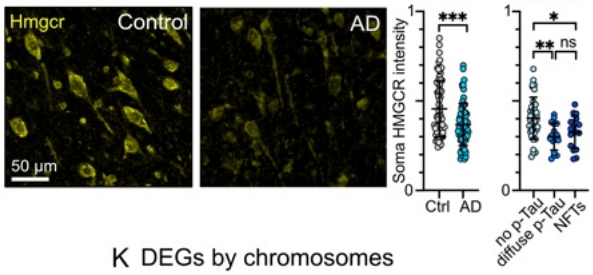

J DEGs in LADs

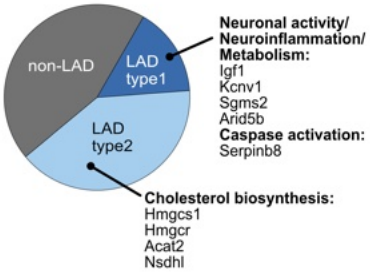

K DEGs by chromosomes

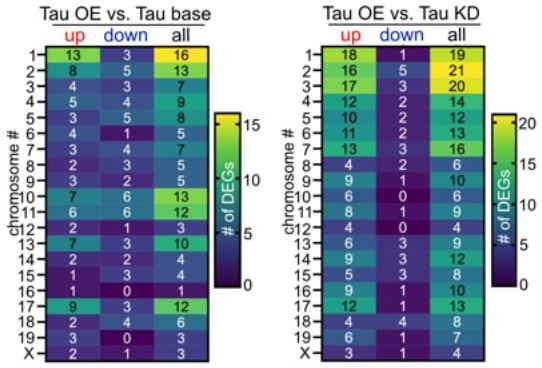

L Chromosome association of LAD type2 DEGs

Tau o/e vs. Tau base

Chr.	DEG	log2 FC
13	Nfil3	1.54
13	Cmah	1.36
13	Gm47075	1.12
13	Gm34466	1.10
13	S1pr3	1.07
13	Pxdc1	1.02
13	**Hmgcs1**	-1.37
13	Gm48342	-1.35
13	**Hmgcr**	-1.09
X	Msn	1.23
X	Lpar4	1.07
X	**Nsdhl**	-1.47

Tau o/e vs. Tau k/d

Chr.	DEG	log2 FC
13	Nfil3	1.70
13	Pxdc1	1.40
13	Gas1	1.18
13	S1pr3	1.18
13	Ccxcl4	1.04
13	Cmah	1.00
13	**Hmgcs1**	-1.18
13	**Hmgcr**	-1.03
13	Gm48342	-1.00
18	Egr1	1.35
18	Ppic	1.24
18	Gramd2b	1.15
18	Aqp4	1.08
18	Grp	-2.62
18	Lipg	-1.29
18	Stard4	-1.27
18	Chst9	-1.01
X	Apln	1.38
X	Sat1	1.12
X	Col4a5	1.00
X	**Nsdhl**	-1.15
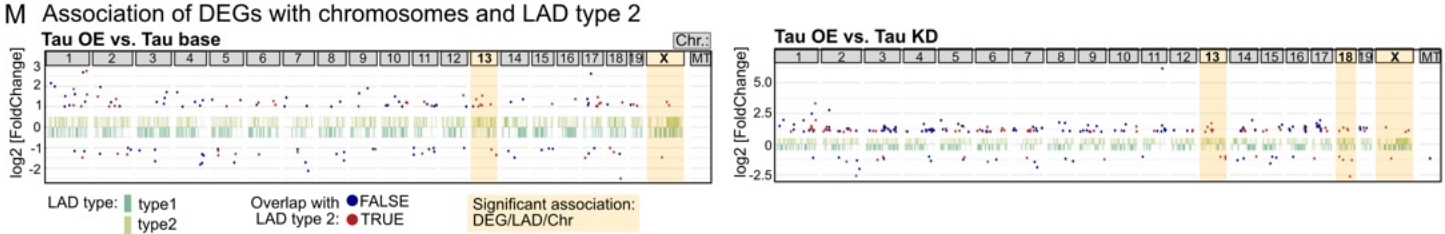
M Association of DEGs with chromosomes and LAD type 2